An investigation of novel and next generation semiconductor and piezoelectric materials using Raman spectroscopic characterisation

David Adley

December 12, 2012

Declaration

This thesis has not been submitted as an exercise for a degree at this or any other university. It is entirely the candidate's own work. The candidate agrees that the Library may lend or copy the thesis upon request. This permission covers only single copies made for study purposes, subject to normal conditions of acknowledgement.

Summary

Raman spectroscopy is an increasingly prevalent material characterisation technique and this work explored its application to several novel semiconductor and piezoelectric materials. Raman spectroscopy is non-destructive allowing the materials under study to be further characterised by additional techniques. The preparation of samples is straightforward in comparison to many existing techniques and allows for in situ measurements. Raman scattering is a multidisciplinary technique requiring familiarisation with chemistry, condensed matter physics and material science. Raman spectroscopy was used to examine and characterise several semiconductor materials that have promising applications in future semiconductor devices.

The project was initially started in collaboration with XSiL Ltd, a small semiconductor equipment manufacturing company, who developed novel laser dicing and drilling system machining tools to replace traditional saw-based dicing and etching systems. 'Through Silicon Vias' (TSV) used in 3D circuits are a new innovation that utilise short, vertical electrical connections or vias passing through a Silicon wafer in order to establish an electrical connection from the active side to the backside of the die. Thus providing the shortest interconnect path and creating an avenue for 3D integration. The application of Raman spectroscopy allowed detailed examination of the stress surrounding these vias in particular in the Heat Affected Zone (HAZ) directly surrounding the via. The Raman analysis of the vias demonstrated that the stress was significantly lower than other published results using established methods. XSiLs intellectual property was purchased by Electro Scientific Industries and it ceased trading in 2009.

A new deposition technique for microcrystalline Silicon (μc-Si) was developed by Phive Plasma Technologies (Phive), a campus company in Dublin City University (DCU). The company developed a new plasma source that removes some of the restrictions in existing plasma deposition equipment. μc-Si has many useful advantages, if grown properly it can have a higher electron mobility than amorphous Silicon, due to the presence of the Silicon crystallite which is advantageous when manufacturing solar cells. However, it is quite difficult to determine the crystallinity fraction, the ratio of amorphous material to crystallites of this material which has important effects on it performance. The application of several techniques including Raman spectroscopy and X-Ray Diffraction were investigated and successful attempts were made using chemometric analysis of the Raman data and polarisation filters to determine the crystalline fraction.

In collaboration with the Northern Ireland Semiconductor Group at The Queen's University Belfast, we investigated a novel fabrication technique in which deposited Germanium was rapidly annealed to produce single crystal Germanium from a Silicon seed. Germanium-on-insulator substrates are seen as a potential replacement for Silicon on miniaturized chips. Germanium is also used as a substrate for high-efficiency photovoltaic cells. Raman spectroscopy was used to analyse the crystalline purity of this material and its degradation with distance from the Silicon seed. The results showed that the rapid annealing of Germanium produced good quality crystalline Germanium a significant distance from the seed window but the structural integrity was weak.

Strontium doped lead Zirconate Titanate is a piezoelectric material sometimes called a smart material which is a material that has one or more properties that can be changed by external stimuli e.g. stress, temperature, moisture, pH electric or magnetic fields. The ferromagnetic properties of Strontium doped Zirconate Titanate were analysed to determine if transformation of its crystalline structure occurred due to temperature changes. Raman spectroscopy was used in this case to determine the Curie point at which the crystalline properties change.

In addition attempts were made to determine dopant diffusion in Tungsten Silicide (WSi),

using Raman characterisation. WSi is an ideal buried metallic layer as it is a refractory material that offers low sheet resistance (typically 2Ω for a 200-nm layer) and excellent thermal stability with many potential applications in transistor technology.

The important materials characterised and analysed by Raman spectroscopy has and will contribute to advances in the semiconductor and solar cell industries.

Acknowledgements

The first person I would like to thank is my supervisor Dr. Tatiana Perova for her dedication and enthusiasm. Throughout the duration of this thesis she has always been extremely supportive and approachable. Secondly, my parents without whom the completion of this work would have been impossible. I would also like to thank the numerous fellow researchers and collaborators who have provided support and help including, Joanna Wasyluk, Nurfarina Zainal, Mike Bain, Sharath Sriram, Madhu Bhaskaran, Eamonn Monaghan, Franz Schmied, Karsten Rode, Ann Baldycheva and Sergey Dyakov.

Contents

List of Figures

List of Tables

Nomenclature

$\mathbf{q}$	Wave vector
$\mathbf{K}$	Set of reciprocal lattice vectors
$\mathbf{R}$	Set of Bravais lattice vectors
$\mathscr{H}$	Hamiltonian
AFM	Atomic Force Microscopy
ALS	Alternating Least Squares
CLS	Classical Least Squares
CVD	Chemical Vapour Deposition
DPSS	Diode-Pumped Solid-State
DRIE	Deep Reactive Ion Etching
EDX	Energy Dispersive X-Ray
FIB	Focused Ion Beam
FWHM	Full Width Half Maximum
MCR	Multivariate Curve Resolution
MEMS	Microelectromechanical systems

PCA Principal Component analysis

PECVD Plasma Etched Chemical Vapour Deposition

PSZT Sr doped Piezoelectric Lead Zirconate Titanate

PVD Physical Vapour Deposition

PZT Piezoelectric Lead Zirconate Titanate

RIE Reactive Ion Etching

RMG Rapid Melt Growth

RTA Rapid Thermal Anneal

SEM Scanning Electron Microscopy

SEM Scanning Electron Microscopy

SOI Silicon on Insulator

SSOI Silicon on Silicide on Insulator

TEM Transmission Electron Microscopy

TEOS Tetraethylorthosilicate

TSV Through Silicon Via

XRD X-Ray Diffraction

Chapter 1

Introduction to Raman Spectroscopy

Raman Spectroscopy is the study of the interaction of electromagnetic radiation with matter. Initially the background theory is presented which describes molecular scattering before advancing to the scattering of crystalline materials addressed in the bulk of this thesis.

Raman scattering occurs when a system exchanges energy inelastically with a photon. These photons can interact with matter by absorption or scattering processes and the system excites or decays to vibrational energy levels above or below that of the initial state. The scattering may occur either elastically, or inelastically. The elastic process is termed Rayleigh scattering, whilst the inelastic process is termed Raman scattering. Rayleigh scattering always accompanies Raman scattering, unless selective notch filters are employed [1]. In the molecular case the electric field component of the scattering photon perturbs the electron cloud of the molecule and may be regarded as exciting the system to a virtual state. The Raman scattered light occurs at wavelengths that are shifted from the incident light by the energies of molecular vibrations. The frequency shift corresponding to the energy difference between the incident and scattered photon is termed the Raman shift. Depending on whether the system has lost or gained vibrational energy, the Raman shift occurs either as an up- or down-shift of the scattered photon frequency relative to that of the incident photon. The down-shifted and up-shifted components are called respectively the Stokes and anti-Stokes lines. A plot of scattered photons is a Raman spectrum. Different materials

have different vibrational modes, and therefore characteristic Raman spectra. This makes Raman spectroscopy a useful technique for material identification. Crystals do not behave as if composed of molecules with specific vibrational energy levels, instead the crystal lattice undergoes vibration. The macroscopic vibrational modes existing in the crystal are called phonons.

1.0.1 Molecular Scattering

According to quantum theory, a molecular motion can have only certain discrete energy levels. A change in level is accompanied by the gain or loss of one or more quanta of energy. The interaction of a molecule with electromagnetic radiation can thus be analysed in terms of an energy-transfer mechanism [2]. When incident monochromatic radiation of energy $h\upsilon$ (in Joules) collides with the molecules in sample, there are two possibilities. If the collision is elastic the scattered phonons will have the same energy as the incident photons from the radiation source. However, if the collision is inelastic the scattered photons will have a higher or lower energy than the incident photon. The summed kinetic energy of the photon and the molecule remains the same before and after the collision. If E represents the rotational, vibrational, and electronic energy of the molecule before a collision and E' represents the same values after the collision, then the law of conservation of energy gives,

$$h\upsilon + E = h\upsilon' + E' \tag{1.1}$$

Rearranging eqn. (1.1) gives

$$\frac{E' - E}{h} = \upsilon - \upsilon' \tag{1.2}$$

The scattered radiation is classified as follows

$$E = E'(\upsilon = \upsilon') \qquad \text{Raleigh Scattering} \qquad (1.3)$$

$$\left.\begin{aligned} E > E'(\upsilon < \upsilon') \\ E < E'(\upsilon > \upsilon') \end{aligned}\right\} \qquad \text{Raman Scattering} \qquad (1.4)$$

It is evident from these equations that during the Raman scattering case,the total energy of the system increases or decreases as a result of the incident radiation. The energy diagrams for these interactions are shown in Fig. 1.1.

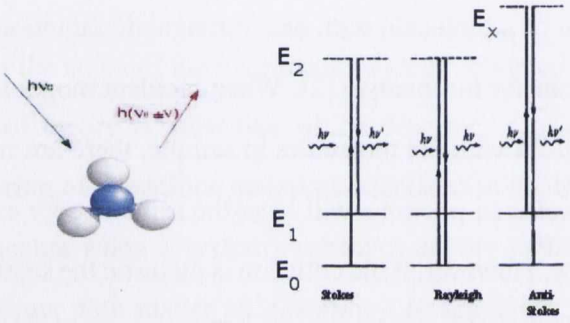

Figure 1.1 – Energy diagrams of molecular interactions with incident radiation

Figure 1.1 shows that when a system interacts with incident radiation of wavenumber υ_0, it may make an upward transition from a lower energy level E_1 to an upper energy level E_2. It must then acquire the necessary energy $E = E_2 - E_1$ from the incident radiation. This energy requirement may be regarded as the annihilation of one photon of the incident radiation hv and the simultaneous creation of a photon of smaller energy $h(\upsilon_0 - \upsilon_m)$, so that scattering of radiation of lower wavenumber, $\upsilon_0 - \upsilon_m$, occurs (see Fig. 1.1). Conversely, the interaction of the radiation with the system may cause a downward transition from a higher energy level E_2 to a lower energy level E_1 in which case energy becomes available, $E_2 - E_1 = h\upsilon_m$, so that scattering of radiation of higher wavenumber, $\upsilon_0 + \upsilon_m$, occurs. For the case of Rayleigh scattering, there is one photon annihilated and one photon of the same energy created simultaneously. Therefore there is no resultant change of energy in the system.

When a molecule is promoted from a ground state to a higher state and remains at this higher state, Raman scattering is produced and gives rise to the Stokes lines in a Raman spectrum. If a molecule is initially in an excited (vibrational) state it can be promoted to a higher unstable state and then return to the ground state in which case Raman scattering is also produced giving rise to the anti-Stokes lines in a spectrum. Fig. 1.2 shows the relative intensities of the Stokes and anti-Stokes lines compared to the Rayleigh line. It is clear that the scattering intensity of the anti-Stokes peak is weaker than the Stokes peak. This is because the system exists mostly at the ground energy state E_0 so that the population of E_0 is much larger than higher energy levels at room temperature. Therefore, the probability that molecules will be excited from the energy level E_0 is much higher than from energy level E_1. The intensity of the anti-stokes line is heavily dependent on the population of the E_1 state and is therefore highly temperature dependent. Typically the intensity of the Rayleigh line is 10^{-3} weaker than the incident excitation, while the Raman features are at least another factor of 10^{-3} weaker [3].

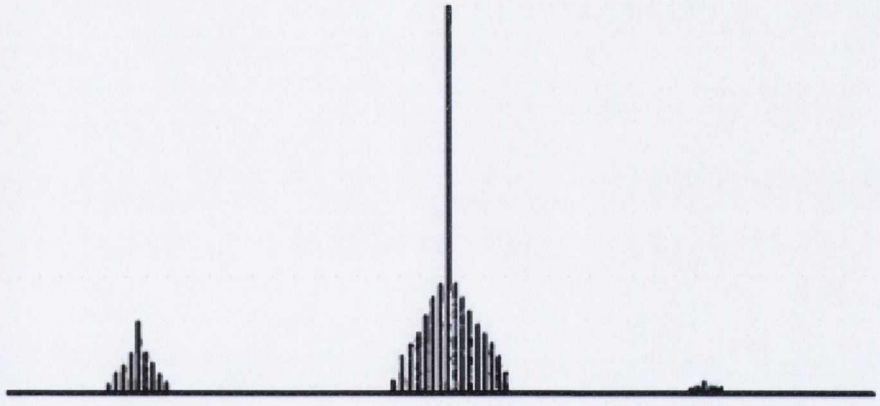

Figure 1.2 – Raman intensity of the Stokes, Rayleigh and anti-Stokes lines

Raman spectroscopy later gained increasing relevance in the study of thin layers such as those used in the semiconductor industry. This was possible due to the addition of a microscope to the conventional Raman system allowing an area of micron scale to be investigated with both a white light microscope and an excitation monocromatic light source, multiple excitation wavelengths and CCDs with increased sensitivity provide huge advancements in

the investigation of materials using Raman spectroscopy. Some of the most important material parameters that can be characterised include the chemical composition of the sample, long and short range order, stress, crystallinity and the presence of defects. A number of materials with important applications were investigated with the intention of exploring existing characterisation techniques and improving them. In particular the material characteristics of standard crystalline semiconductors such as Germanium and Silicon were examined along with silicides and piezo electric materials.

1.1 Band Theory of Crystalline Structures

In order to understand the Raman scattering from crystalline structures it is necessary to examine the lattice structures and their influence on the vibrational modes.

1.1.1 Crystal Lattices

The *Bravais lattice* specifies the periodic array of atoms or molecules that make up a crystalline lattice [4]. It is defined as

- An infinite array of discrete points with an orientation and structure that appear identical from whatever point the lattice is viewed.
- A lattice that has position vectors of the form

$$\mathbf{R} = n_1\mathbf{a}_1 + n_2\mathbf{a}_2 + n_3\mathbf{a}_3 \tag{1.5}$$

  where $\mathbf{a}_1$, $\mathbf{a}_2$ and $\mathbf{a}_3$ are any three vectors not in the same plane and n_1, n_2 and n_3 include all integer values.

The lattice vectors, $\mathbf{a}_1$, $\mathbf{a}_2$ and $\mathbf{a}_3$ in the second definition are called *primitive* vectors. The face-centered cubic and body-centred cubic lattices are the most important and commonly occurring Bravais lattices.

The *primitive unit cell* is the volume of space that when translated along all the vectors in the lattice results in the complete lattice. Numbers specifying the size of a unit cell are called, *lattice constants*. A unit cell can come in many shapes and sizes, however the most common is the *Wigner-Seitz cell* [4]. The Wigner-Seitz cell about any lattice point is the region of space that is closer to that point than any other point. It is generally constructed by drawing lines connecting the lattice point to its neighbouring lattice points and bisecting these lines with a plane to create a polyhedron that forms the cell.

1.1.2 Reciprocal Lattice

The *reciprocal lattice* of a Bravais lattice is defined as the set of all wave vectors, **K**, that yield plane waves, $e^{i\mathbf{K}\cdot\mathbf{r}}$ with the periodicity of the lattice [4]. **K** belongs to the reciprocal lattice of a Bravais lattice. If **R** is the collection of points that make up the Bravais lattice, the reciprocal lattice is the set of wave vectors, **K** that satisfy

$$e^{i\mathbf{K}\cdot\mathbf{R}} = 1 \tag{1.6}$$

The reciprocal lattice is a Bravais lattice with the three primitive vectors defined as

$$\begin{aligned}
\mathbf{b_1} &= 2\pi \frac{\mathbf{a_2} \times \mathbf{a_3}}{\mathbf{a_1} \cdot (\mathbf{a_2} \times \mathbf{a_3})} \\
\mathbf{b_2} &= 2\pi \frac{\mathbf{a_3} \times \mathbf{a_1}}{\mathbf{a_1} \cdot (\mathbf{a_2} \times \mathbf{a_3})} \\
\mathbf{b_2} &= 2\pi \frac{\mathbf{a_1} \times \mathbf{a_2}}{\mathbf{a_1} \cdot (\mathbf{a_2} \times \mathbf{a_3})}
\end{aligned} \tag{1.7}$$

where $\mathbf{a_1}$, $\mathbf{a_2}$ and $\mathbf{a_3}$ are the primitive lattice vectors of the direct Bravais lattice. All coefficients of $\mathbf{b_1}$, $\mathbf{b_2}$ and $\mathbf{b_3}$ must be integers if Eqn. (1.6) is to be satisfied. The Wigner-Seitz primitive cell of the reciprocal lattice is known as the *first Brillouin zone*, shown in Fig. 1.3.

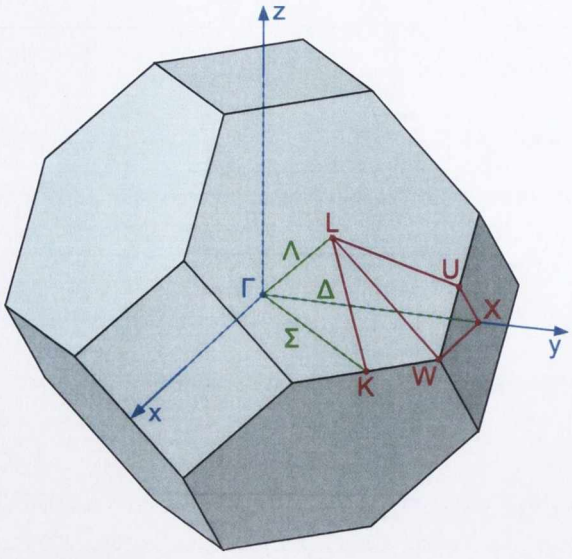

Figure 1.3 – Silicon first Brillouin zone [5]. High symmetry points are labelled with capital letters. Vector directions towards high symmetry point are labelled with Greek letters.

1.1.3 Crystalline Orientation

A crystalline structure can be separated into planes of atoms called *lattice planes*. The reciprocal lattice vectors are perpendicular to the lattice planes. The orientation of lattice planes is specified by a vector normal to that plane. In general the shortest reciprocal lattice vectors normal to the plane are used. The coordinates of this vector are called the *Miller indices* [4].

$$\mathbf{k} = h\mathbf{b_1} + k\mathbf{b_2} + l\mathbf{b_3} \tag{1.8}$$

where, h, k and l are the Miller indices and $\mathbf{b_1}$, $\mathbf{b_2}$ and $\mathbf{b_3}$ are the primitive vectors defined in Eqn. (1.7). Lattice planes are defined by giving their miller indices in parenthesis, *(h, k, l)*.

If directions are needed in a lattice the convention, $[n_1 n_2 n_3]$ is used where n_1, n_2 and n_3 are integer coefficients of the direct Bravais lattice, $n_1\mathbf{a_1} + n_2\mathbf{a_2} + n_3\mathbf{a_3}$ and $\mathbf{a}_1$, $\mathbf{a}_2$ and $\mathbf{a}_3$ are the direct lattices vectors.

1.1.4 Normal Modes of Three Dimensional Monatomic and Polyatomic Bravais Lattice

The displacement of the atoms from their equilibrium position are assumed to be time dependent plane waves

$$\mathbf{u}(\mathbf{R},t) = \varepsilon e^{i(\mathbf{k}\cdot\mathbf{R}-\omega t)} \tag{1.9}$$

in this case ε is a vector that describes the direction in which the ions move. It is known as the *polarization vector* of the normal mode. The Born-von Karmen boundary condition, stating that the final atom is identical to the first atom to remove boundary effects is also enforced.

$$\mathbf{u}(\mathbf{R}+N_i\mathbf{a_i}) = \mathbf{u}(\mathbf{R}) \tag{1.10}$$

where N_i are large integers satisfying $N = N_1N_2N_3$ and $\mathbf{a_i}$ describe the three primitive lattice vectors. Due to this condition the possible values of $\mathbf{k}$ are restricted to

$$\mathbf{k} = \frac{n_1}{N_1}\mathbf{b_1} + \frac{n_2}{N_2}\mathbf{b_2} + \frac{n_3}{N_3}\mathbf{b_3}, \qquad n_i \text{ integral} \tag{1.11}$$

where $\mathbf{b_i}$ are the reciprocal lattice vectors satisfying $\mathbf{b_i}\cdot\mathbf{a_j} = 2\pi\delta_{ij}$. The values of $\mathbf{k}$ are restricted to the first Brillouin zone as $e^{i\mathbf{K}\cdot\mathbf{R}} = 1$, where $\mathbf{K}$ is a reciprocal lattice vector. As a result there will be N nonequivalent values of $\mathbf{k}$ inside the Brillouin zone. A solution is found whenever ε is an eigenvector of the three-dimensional eigenvalue problem [4]:

$$M\omega^2\varepsilon = \mathbf{D}(\mathbf{k})\varepsilon \tag{1.12}$$

$\mathbf{D}(\mathbf{k})$ is known as the *dynamical matrix* and is given by

$$\mathbf{D}(\mathbf{k}) = \sum_{\mathbf{R}} \mathbf{D}(\mathbf{R})e^{-i\mathbf{k}\cdot\mathbf{R}} \tag{1.13}$$

the dynamical matrix has three real eigenvalues which satisfy

$$\mathbf{D}(\mathbf{k})\varepsilon_s(\mathbf{k}) = \lambda_s(\mathbf{k})\varepsilon_s(\mathbf{k}) \qquad s = 1, 2, 3 \tag{1.14}$$

for each of the N allowed values of $\mathbf{k}$ three normal modes are possible. The three normal modes with wave vector $\mathbf{k}$ will have three polarisation vectors $\varepsilon_\mathbf{s}(\mathbf{k})$ and frequencies given by

$$\omega_s(\mathbf{k}) = \sqrt{\frac{\lambda_s(\mathbf{k})}{M}} \tag{1.15}$$

These results give rise to the dispersion curves, an example for Silicon is given in Fig. 1.4. If the *basis* is not monatomic but rather has *two* ions per primitive unit cell than additional branches are added. For each value of $\mathbf{k}$ there are $3p$ normal modes, where p is the number of ions in the basis. Three of the $3p$ branches are *acoustic*, they describe vibrations with frequencies that vanish linearly with k in the long wavelength (small $\mathbf{k}$) limit. The other $3(p-1)$ branches are *optical*, their frequencies do not vanish in the long wavelength limit. One branch is labelled *longitudinal* if the branch is polarised along the direction of propagation ($\varepsilon \parallel \mathbf{k}$) and the other two are labelled *transverse* as their motion is perpendicular to the direction of propagation ($\varepsilon \perp \mathbf{k}$).

1.1.5 Quantum Theory of Normal Modes

To specify the energy levels of an N-ion harmonic crystal, one regards it as $3N$ independent oscillators, whose frequencies are those of the $3N$ classical normal modes. The contribution to the total energy of a particular normal mode of branch s and wave vector $\mathbf{k}$ with angular frequency $\omega_s(\mathbf{k})$ can only have the discrete values

$$(n_{\mathbf{k}s} + \frac{1}{2})\hbar\omega_s(\mathbf{k}) \tag{1.16}$$

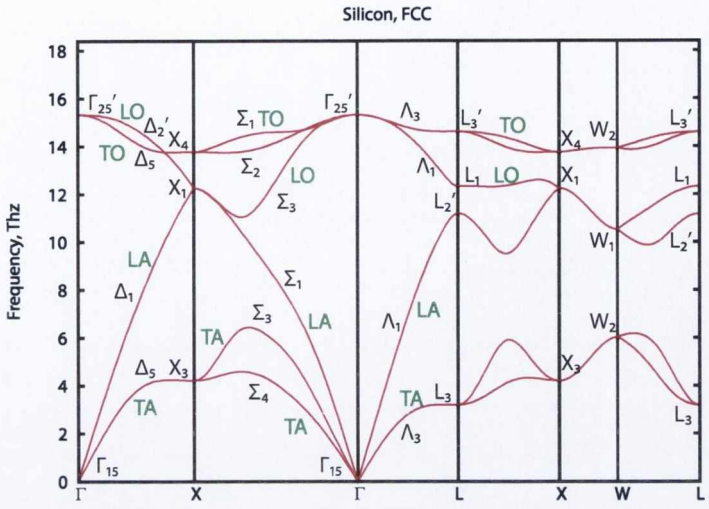

Figure 1.4 – Silicon dispersion curves, Silicon has a diatomic basis. The branches that vanish at the Γ point are acoustic branches, while those that have none zero values at the Γ point are optical branches. Generated using the 'PlotPhon' component of the Quantum Espresso software [6].

where $n_{\mathbf{k}s}$, the excitation number of the normal mode is restricted to the values 0, 1, 2, ... The total energy is just the sum of the energies of the individual normal modes:

$$E = \sum_{\mathbf{k}s} (n_{\mathbf{k}s} + \frac{1}{2}) \hbar \omega_s(\mathbf{k}) \tag{1.17}$$

Instead of saying that the normal mode of branch s with wavevector $\mathbf{k}$ is in the $n_{\mathbf{k}s}$ excited state, one says that there are $n_{\mathbf{k}s}$ *phonons* of type s with wavevector $\mathbf{k}$ present in the crystal.

1.2 Group Theory Notation of Electronic States and Lattice Vibrations

Eigenfunctions of the Hamiltonian form bases for irreducible representations of the space group G. Each irreducible representation of the space group is characterised by star$\{\mathbf{k}\}$ and a small representation of the point group, $\mathscr{G}(\mathbf{k})$, formed by star$\{\mathbf{k}\}$ [7].

For example Germanium and Silicon belong to the O_h^7 space group, with a diatomic unit cell consisting of two atoms one at the origin (000) and one at $\tau = (a/4, a/4, a/4)$. Therefore

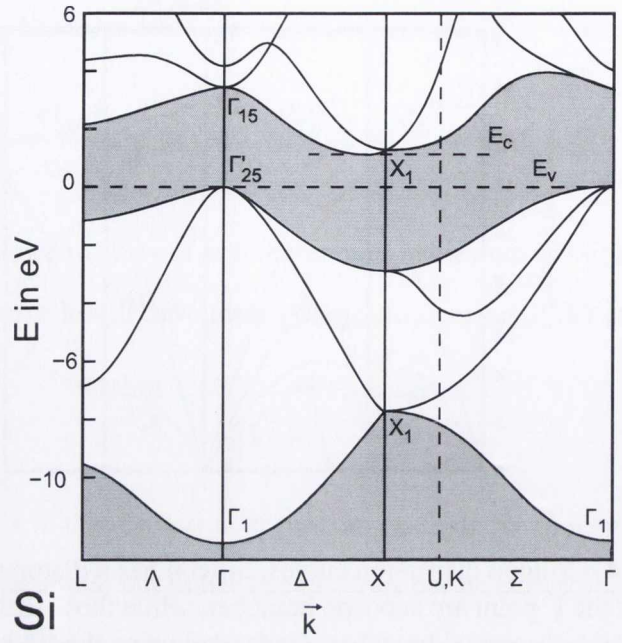

Figure 1.5 – Electronic band structure of Silicon including small representations. Created using Quantum-Espresso software [6].

any electrons with wave vector $\mathbf{k} = 0$ must have a wave function with one of the symmetries given in the O_h character table shown in Table 1.1. The two lowest electron energies (the s orbitals) have the symmetries, Γ_1 and Γ_2'.

Table 1.1 – O_h character table [7].

O_h	E	$8C_3$	$6C_2$	$6C_4$	$3C_2$	i	$6S_4$	$8S_6$	$3\sigma_h$	$6\sigma_d$		
A_1g (Γ_1)	1	1	1	1	1	1	1	1	1	1		$x^2+y^2+z^2$
A_2g (Γ_2)	1	1	-1	-1	1	1	-1	1	1	-1		
E_g (Γ_{12})	2	-1	0	0	2	2	0	-1	2	0		$(2z^2-x^2-y^2, x^2-y^2)$
T_{1g} ($\Gamma_{15'}$)	3	0	-1	1	-1	3	1	0	-1	-1	(R_x, R_y, R_z)	
T_{2g} ($\Gamma_{25'}$)	3	0	1	-1	-1	3	-1	0	-1	1		(xz, yx, z, xy)
A_{2u} ($\Gamma_{2'}$)	1	1	-1	-1	1	-1	1	-1	-1	1		xyz
E_u ($\Gamma_{12'}$)	2	-1	0	0	2	-2	0	1	-2	0		
T_{1u} (Γ_{15})	3	0	-1	1	-1	-3	-1	0	1	1	(x, y, z)	(x^3, y^3, z^3)
T_{2u} (Γ_{25})	3	0	1	-1	-1	-3	1	0	1	-1		$[x(z^2-y^2), y(z^2-x^2), z(x^2-y^2)]$
$\Gamma_{x,y,z}$	3	0	-1	1	-1	-3	-1	0	1	1		

The *p* orbitals correspond to the three degrees of freedom each atom has. In consequence the small representations of the *p* orbitals determine the symmetries of the normal modes of the lattice vibrations. Silicon and Germanium have the Γ_{15} *acoustic* mode in which the atoms at (000) and η move in phase and the Γ'_{25} *optic* mode in which they move out of phase [7].

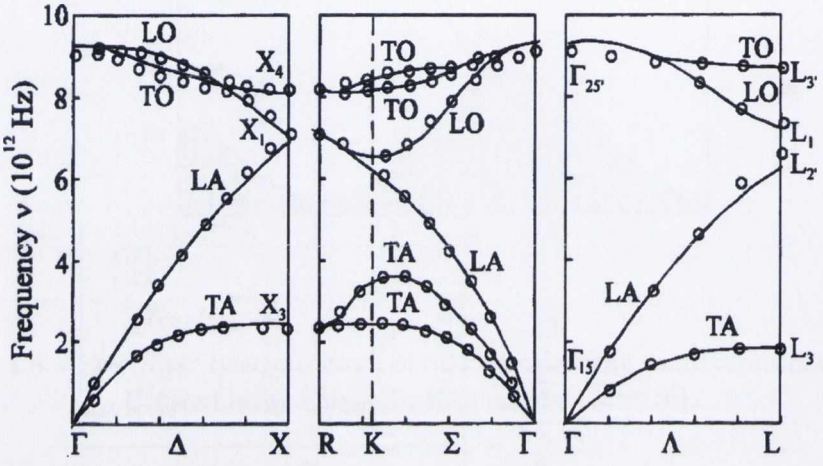

Figure 1.6 – Germanium phonon dispersion curves including symmetries. TA(O) is Traverse Acoustic(Optical) and LA(O) is Longitudinal Acoustic(Optical). Not the symmetries at the zone centre phonon Γ [7].

Chapter 2

Raman Theory of Scattering in Crystalline Structures

Each elementary Raman scattering event involves the destruction of a photon of frequency ω_i, the creation of a scattered photon of frequency ω_s and the creation or destruction of a phonon of frequency ω_q.

The scattering crystal is generally in its electronic ground state with all valence bands full and all conduction bands empty at the start of the scattering process and it returns to the electronic ground state at the end of the event.

2.1 Theory using Born-Bradman Approach

The intensity of the scattered radiation is arrived at by calculating the electric moment **M** set up in the crystal by the electric vector $\Re[\mathbf{E}\exp(-i\omega t)]$ of the incident light beam. If the polarizability tensor associated with the electrons in the crystal is, $\alpha_{\rho\sigma}$, then

$$M_\rho = \sum_\rho \alpha_{\rho\sigma} E_\sigma \tag{2.1}$$

The quantum mechanical expression for the electric polarizability tensor, $\alpha_{\rho\sigma}$ involves the energy eigenvalues and wave-functions of the electron system. These values are perturbed

by the existence of phonons as they move the position of atoms but not by electron-incident light interactions as this just excites the electrons into different eigenstates but does not affect those individual eigenstates. Due to this dependence on the electron-lattice interaction the electronic-eigenvalues and wave-functions in a diatomic lattice depend on the relative displacement amplitude **r** of the two sub lattices. The electronic polarizability can be expanded in a power series in **r**

$$\alpha^0_{\rho\sigma} = \alpha^{(0)}_{\rho\sigma} + \sum_{\mu} \alpha_{\rho\sigma,\mu} r_\mu + \sum_{\mu,\upsilon} \alpha_{\rho\sigma,\mu\upsilon} r_\mu r_\upsilon + O(r^3) \tag{2.2}$$

where

$$\alpha_{\rho\sigma,\mu} = \left(\frac{\partial \alpha_{\rho\sigma}}{\partial r_\mu}\right)_{r=0} \qquad \text{and} \qquad \alpha_{\rho\sigma,\mu\upsilon} = \left(\frac{\partial^2 \alpha_{\rho\sigma}}{\partial r_\mu \partial r_\upsilon}\right)_{r=0} \tag{2.3}$$

The term linear in r gives rise to the first-order Raman scattering, the quadratic term gives rise to second order Raman scattering and so on. It is obvious that Raman scattering cannot occur if change in **r** does not result in a change in the polarizability tensor.

Diamond has been investigated and the square of the relative displacement amplitude caused by a *single* optic phonon in diamond is given by

$$< r^2 >= \hbar / 2M\omega_0 \tag{2.4}$$

where M is the reduced mass of the two sublattices and ω_0 is the phonon frequency. Smith [8] has investigated the symmetry properties of $\alpha_{\rho\sigma,\mu}$ and finds that the only non-vanishing components of the tensor are those for which, ρ, σ and μ refer to different crystal axes. This leaves three distinct components (the tensor is symmetrical with respect to interchange of ρ and σ because it is derived from the symmetrical polarizability tensor $\alpha_{\rho\sigma}$) which are all equal. The scattering intensity can then be written assuming no phonon polarisation

$$I = A_c \left[\sum_{\rho,\sigma=x,y,z} \varepsilon^{(i)}_\rho \alpha_{\rho\sigma} \varepsilon^{(s)}_\sigma \right] \tag{2.5}$$

Smith has calculated the Raman scattering intensity I. The result for the first order Raman

scattering intensity for a diatomic non-polar crystal with diamond structure

$$I = \frac{\hbar\omega_S^4 LdW}{\rho c^4 \omega_0}(n_0+1)[|\alpha_{xy}|^2 + |\alpha_{zy}|^2 + |\alpha_{zx}|^2] \tag{2.6}$$

where L is the length of the crystal in the direction of $\mathbf{k}_i$, ρ is the crystal density, n_0 is the Bose population factor for the photon and the three Raman tensors ($\alpha_{xy} etc.$) are equal. In the case of anti-stokes scattering the n_0+1 is replaced by n_0.

2.1.1 Selection Rules

It is important to note that all conclusions in this section depend on the approximation that the phonon wave vector $\mathbf{q} = 0$. This is important as the Raman tensor (neglecting the symmetry requirements imposed by the crystalline structure) is only strictly symmetric if $\omega_\mathbf{q}$ is neglected [9]. As a result the selection rules are only calculated for irreducible phonon representations with $\mathbf{q} = 0$ (the Γ point in the Brillouin zone). The emphasis here is on diatomic non-polar cubic crystals e.g. Silicon and Germanium with O_h point group symmetry at $\mathbf{q} = 0$. Diatomic polar crystals have point group symmetry T_d at $\mathbf{q} = 0$.

The optic phonon at $\mathbf{q} = 0$ has symmetry F_2g for the non-polar crystal and F_2 symmetry for the polar crystal.

Table 2.1 – Raman active vibrational symmetries and Raman tensors for cubic crystal [10].

Raman tensor	$\begin{pmatrix} a & & \\ & a & \\ & & a \end{pmatrix}$	$\begin{pmatrix} & b & \\ b & & \\ & & b \end{pmatrix}$	$\begin{pmatrix} & b & \\ b & & \\ & & b \end{pmatrix}$	$\begin{pmatrix} & & d \\ & & \\ d & & \end{pmatrix}$	$\begin{pmatrix} & & d \\ & & \\ d & & \end{pmatrix}$	$\begin{pmatrix} & & d \\ & & \\ d & & \end{pmatrix}$
O_h	$A_{1g}\,(\Gamma_1)$	$E_g\,(\Gamma_{12})$	$E_g\,(\Gamma_{12})$	$F_2g\,(\Gamma_{25'})$	$F_2g\,(\Gamma_{25'})$	$F_2g(\Gamma_{25'})$
T_d	A_{1g}	E	E	$F_2(x)$	$F_2(y)$	$F_2(z)$

The matrices in Table (2.1) give the non-vanishing components of the Raman tensor e.g. $R_{\rho\sigma}$ and their symmetries depending on point group of the cubic crystal at $\mathbf{k} = 0$. The table shows that the symmetry and values of different components of the Raman tensor are not equal. If the irreducible representation is degenerate then the components corresponding to this irreducible representation must be split, the number of matrices depending on the

degeneracy of the irreducible representation (Two for E and three for F irreducible representations). Splitting the components like this allows some components such as the diagonal components in the table (where $a = b + b$) to have multiple symmetries.

The different elements in the Raman tensor matrix in Table 2.1 are the nine components of the tensor obtained by allowing both ρ and σ to take on the values x, y and z which are the principal axes of the crystal. Such that

$$\begin{pmatrix} R_{xx} & R_{xy} & R_{xz} \\ R_{yx} & R_{yy} & R_{yz} \\ R_{zx} & R_{zy} & R_{zz} \end{pmatrix} \tag{2.7}$$

It can be seen from Table (2.1) that the non diagonal components of the Raman tensor all have the same value, d, for both O_h and T_d point groups. Such that

$$d = R_{xy} = R_{yx} = R_{xz} = R_{zx} = R_{yz} = R_{zy} \tag{2.8}$$

The diagonal components of the tensor have different values from the non-diagonal components. For the E symmetry tensor the diagonal components are split.

Non-polar diatomic semiconductors like Germanium and Silicon have *inversion symmetry* meaning that the two atoms are the same and their charge distribution is symmetric so that the centroids of positive and negative charge coincide. The larger the symmetric vibration the further the atoms move apart and the more difficult it is to move them further therefore changing the polarizability and visa versa when the distance between them is decreasing. As the polarizability changes this vibration is Raman active. In the case of anti-symmetric vibrations the polarizability is maintained as movement of one atom in one direction is followed by movement by the other atom in the same direction. Therefore it is Raman inactive. As a result of this it is easy to see that only symmetric or even-parity (subscript g) vibrations can be Raman active in crystals with inversion symmetry and non-symmetric or odd parity (subscript u) are not Raman active but infra red active in crystals with inversion symmetry.

If a crystal doesn't have inversion symmetry (a piezo-electric crystal) than it is possible for a phonon to be both Raman and Infra-red active.

A phonon can participate in a first-order Raman transition if and only if its irreducible representation is the same as one of the irreducible representations which occur in the reduction of the representation of the Raman tensor[9].

Therefore only the phonons with the symmetries given in Table 2.1 can contribute.

The selection rules are then given by [10]

$$I = A\left[\sum_{j,i=x,y,z} \varepsilon_j^{(i)} R_{ji} \varepsilon_i^{(s)}\right]^2 \tag{2.9}$$

or

$$I = A[\mathbf{e}_i \cdot \mathbf{R} \cdot \mathbf{e}_s^T]^2 \tag{2.10}$$

where $\varepsilon_j^{(i)}$ and $\varepsilon_i^{(s)}$ are the j and i components of the unit polarization vector of the incident and scattered light, **R** is the Raman tensor and **A** is the scattering constant.

2.2 Linewidth

In the previous discussion it has been assumed that the phonon **k** exists in a perfectly harmonic crystal resulting in a constant frequency and infinite lifetime. However in reality this is not the case as there are slight anharmonic interactions. This results in the phonon having a finite lifetime.

The importance of a finite lifetime can be demonstrated through the Fourier transform of an oscillating function described by a complex exponential that is damped by multiplying with a exponential decay so that

$$f(t) = e^{-lt} e^{ict} \tag{2.11}$$

where, l is a constant describing the magnitude of the decay and c is the frequency of the undamped oscillator. The Fourier transform is used to convert from the time domain into the

frequency domain so that

$$\begin{aligned} F(\omega) &= \frac{1}{2\pi}\int_0^a e^{-lt}e^{ict}e^{e-i\omega t}\,dt \\ &= \frac{1}{2\pi}\frac{l-i(\omega-c)}{l^2+(\omega-c)^2} \end{aligned} \tag{2.12}$$

The Fourier transform resulting from the damped oscillation is shown in Fig. 2.1b, the Fourier transform of the undamped oscillator is $\delta(\omega)$.

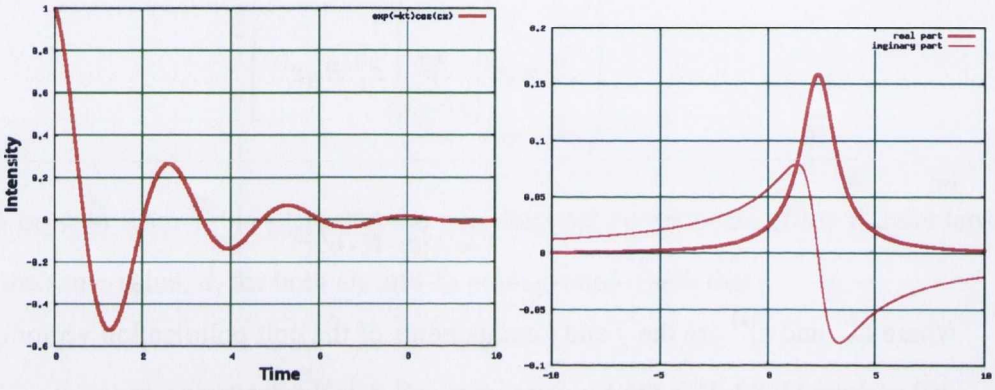

(a) Damped oscillator **(b)** Fourier Transform

Figure 2.1 – Damped oscillator and Fourier Transform.

The broad peak is a result of the exponential function

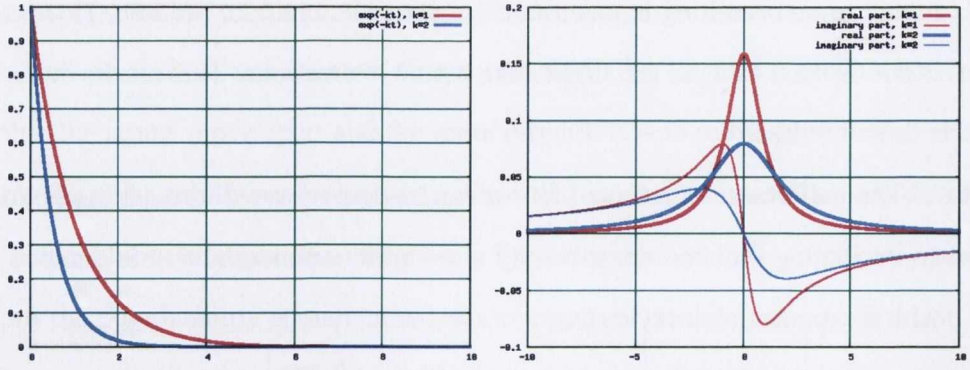

(a) Exponential Function **(b)** Fourier Transform

Figure 2.2 – Fourier transform of exponential decay.

Therefore Fig 2.1 can be thought of as the superposition of Fig. 2.2b and the Fourier

transform of the undamped oscillator, $\delta(\omega)$. The exponential decay determines the line width and the oscillator frequency determines the line position. If the mean lifetime is γ_k^{-1} for phonon k then the line width should be γ_k [11].

This problem was tackled by Brout, [11] in the following manner.

The Hamiltonian, $\mathscr{H}$, of the system is given by

$$\mathscr{H} = \mathscr{H}_s + \mathscr{H}_r + \mathscr{H}_I \tag{2.13}$$

where $\mathscr{H}_s$ is the Hamiltonian of the system, $\mathscr{H}_r$ is the Hamiltonian of the radiation field and $\mathscr{H}_I$ is the interaction Hamiltonian discussed previously. The most important source of damping of a long-wavelength optic phonon is usually the three-phonon anharmonic interaction this is the process in which the phonon decays into a two phonon state with conservation of wave vector [12]. Including this damping factor into $\mathscr{H}_s$ results in

$$\mathscr{H}_s = \mathscr{H}_0 + \lambda V \tag{2.14}$$

where V is a perturbation resulting from the phonon decaying into a two phonon state. It is simpler to examine *spontaneous emission* resulting in the removal of $\mathscr{H}_r$ as the final equations are identical [11]. In a system of this type it is not only the phonon of interest k that changes with time but also all other phonons in the crystal, α will represent all other phonons except k. The entire system to first order can be described by [11]

$$\psi(t) = \psi(0) + i\int_0^t e^{i\mathscr{H}_s(t-t_1)}\mathscr{H}_I e^{i\mathscr{H}_s t_1} \tag{2.15}$$

where the two terms on either side of $\mathscr{H}_I$ are time translation operators. Equation (2.15) is used to find the matrix element for a spontaneous emission [11]

$$\begin{aligned}\langle N_k^f;\alpha;\omega|\psi(t)\rangle = i\sum_{\alpha';\alpha^0;N_k^0}\int_0^t dt_1\,\langle N_k^f;\alpha|e^{i\mathscr{H}_s(t-t_1)}|N_k-1;\alpha'\rangle \\ \times e^{i\omega(t-t_1)}\,\langle N_k-1;\omega|\mathscr{H}_I|N_k\rangle\,\langle N_k;\alpha'|e^{i\mathscr{H}_s t_1}|N_k^0;\alpha^0\rangle\,\langle N_k^0;\alpha^0|\psi(0)\rangle\end{aligned} \tag{2.16}$$

The key differences here from the harmonic case are the time dependence of α and N_k the number of phonons of wave vector k. The terms $\langle N_k^f;\alpha|e^{i\mathscr{H}_s(t-t_1)}|N_k-1;\alpha'\rangle$ and $\langle N_k;\alpha'|e^{i\mathscr{H}_s t_1}|N_k^0;$ can be considered time translation operators. The matrix elements have been calculated [13] to order $\lambda = 2$

$$\langle\beta|e^{i\mathscr{H}_s t}|\beta'\rangle = U_\beta\delta_{\beta\beta'} + i\lambda\int_0^t U_\beta(t-t_1)V_{\beta\beta'}U_{\beta'}(t_1)dt_1 + (i\lambda)^2\sum_{\beta_2}\int_0^t dt_2\int_0^{t_2}[U_\beta(t-t_2)V_{\beta\beta_2}U_{\beta_2}(t_2-t_1)V_{\beta_2\beta'}U_{\beta'}(t_1)]dt_1+\ldots \quad (2.17)$$

where $|\beta\rangle = |N_k;\alpha\rangle$ is the index of the whole system. λ^2 is the fist non vanishing term keeping only this terms results in

$$\langle\beta|e^{i\mathscr{H}_s t}|\beta'\rangle = (i\lambda)^2\sum_{\beta_2}\int_0^t dt_2\int_0^{t_2}[U_\beta(t-t_2)V_{\beta\beta_2}U_{\beta_2}(t_2-t_1)V_{\beta_2\beta'}U_{\beta'}(t_1)]dt_1 \quad (2.18)$$

where

$$U_\beta(t) = e^{i[E(\beta)+\Delta(\beta)+i\Gamma(\beta)]t} \quad (2.19)$$

$$\Gamma_\beta = \pi\lambda^2\sum_{\beta'}|\langle\beta|V|\beta'\rangle|^2\delta(E_\beta - E_{\beta'}) \quad (2.20)$$

$$\Delta_\beta = \lambda^2\sum_{\beta'}|\langle\beta|V|\beta'\rangle|^2[1/(E_\beta - E_{\beta'})]_P \quad (2.21)$$

E_β is an unperturbed eigenvalue of $\mathscr{H}_0$. The $\Gamma(\beta)$ term, eqn (2.20) results from the system changing between degenerate states (single phonon decaying into two) of the unperturbed system and results in the linewidth as shown in Fig. 2.1. This mathematical construct simply defines the uncertainty of the energy due to the short lifetime of the phonon in terms of the energy states of the unperturbed system. It is therefore useful to determine the crystallinity of the system as the more uncrystalline the crystal the shorter the relaxation time. The $\Delta(\beta)$ term is the change in energy (harmonic frequency) of the system due to the interaction.

After making several simplifying assumptions and inserting Eqn. (2.18) into (2.16) the

eventual probability of transition is given by [11]

$$W_{N_k \to N_k - 1}(\omega) = \frac{|\langle N_k - 1|\mathscr{H}_I|N_k\rangle|^2 P_{N_k}}{2\bar{\gamma}_k} \frac{2\bar{\gamma}_k}{(\omega - \bar{\omega}_k)^2 + (2\bar{\gamma}_k)^2} \tag{2.22}$$

where $\bar{\gamma}_k$ and $\bar{\omega}_k$ are the mean linewidth and frequency respectively of phonon k. For almost all α on the energy surface the populations are near to their equilibrium positions so that $\gamma_k(\alpha) \approx \bar{\gamma}_k$ where

$$\gamma_k(\alpha) = \Gamma_{N_k;\alpha} - \Gamma_{N_k - 1;\alpha} \tag{2.23}$$

The distribution of the possible frequencies about $\bar{\omega}$ follows a *Lorentzian* distribution.

2.3 Second Order Spectrum of Crystalline Silicon

Although the selection rules discussed previously limit Raman scattering to the zone-centre optical phonon with representation $\Gamma_{25'}$, this is not the only Raman active representation. Examining Table 1.1 the Γ_1, Γ_{12} and $\Gamma_{25'}$ representations are all Raman active. The zone centre optical phonon has the irreducible representation $\Gamma_{25'}$ and this is visible in first order Raman scattering. Second order Raman scattering occurs when the two phonons participate in the scattering process. There are two types of scattering process resulting in a line spectrum (a spectrum consisting of defined lines) and a continuous spectrum.

Line spectrum, in this case two first order events occur successively and the selection rules must allow for both phonons to be scattered individually. In Silicon only the zone-centre peak at 520 cm^{-1} is Raman active so this type of scattering does not occur [14] except for the zone-centre overtone.

Continuous spectrum, here the scattering event results in the creation of two phonons simultaneously [14]. The wave vector conservation rules must still be applied, however meaning that the sum of the two created phonons must balance the photon wave vector. As the photon wave vector $k \approx 0$ then the wave vector of the two phonons must be equal and opposite resulting in a sum of zero wave vector. Therefore the second order Raman spectrum is

dependent upon the density of states of two phonons with equal and opposite wave vector. If both phonons belong to the same branch then the two phonon state is called an *overtone*. In Silicon the vast majority of distinguishable second order scattering results from overtones. If however the two phonons belong to different branches the two phonon state is called a *combination*, in Silicon the second order peak at 610 cm^{-1} is a result of a combination state [15]. The analysis of the two phonon density of states is conducted mainly through *critical point analysis*, [15]. Critical points have been discussed previously and their importance lies in the fact that a plot of phonon density of states against frequency will in general have discontinuity of slope at critical points. Most of these critical points occur a points of high symmetry in the Brillouin zone. These discontinuous effects will only occur for phonon pairs that the selection rules allow. The selection rules for phonon pairs are calculated using group theory. The two phonon state is assumed to belong to the product representation (generally reducible) formed from the two representations to which the two phonons belong. The incident and scattered photons belong to the zone-centre ($\mathbf{k} = 0$) representations, Γ_1, Γ_{12} and $\Gamma_{25'}$. In order to satisfy the selection rule which requires that the net $\mathbf{k}$ vector be conserved the two phonons must have equal but opposite wave vector. Since their net wave vector is zero, the product representation for the two phonon pair consists of a sum of irreducible zone centre representations. This is equivalent to asking if the product representation for the two phonon state contains Γ_1, Γ_{12} or $\Gamma_{25'}$ [15]. The group-theoretical selection rules derived for two phonon Raman scattering are shown in Table 2.2.

Each of these irreducible representations will have selection rules that depend upon the polarisation of the incident and scattered light. In the case of a Silicon wafer with face (001) and backscattering geometry with the incident light parallel to the cubic axes the polarisation selection rules are given in Table 2.3.

As a result of these selection rules and similar rules for samples with different faces it is possible to identify the scattering from each irreducible representation.

From Fig. 2.3 it is obvious that the Γ_{12} representation contributes very little to the spectrum. The $\Gamma_{25'}$ representation scatters primarily from the zone centre phonon at 520 cm^{-1}

Table 2.2 – Examples of some notable critical points and their group theoretical selection rules [15]. A complete analysis of the second order spectrum including all critical points can be found in [16].

Region in k space	One-phonon representations	zone-centre reduction coefficients			Two phonon frequency (cm^{-1})
		Γ_1	Γ_{12}	$\Gamma_{25'}$	
General point		1	1	1	
Γ	$\Gamma_{25'} \otimes \Gamma_{25'}$	1	1	1	1040
X	$X_3 \otimes X_3$	1	1	1	300
	$X_4 \otimes X_4$	1	1	1	920
L	$L_3 \otimes L_3$	1	0	1	230
	$L_{3'} \otimes L_{3'}$	1	1	2	980
W	$W_2 \otimes W_2$	1	1	1	940

Table 2.3 – Polarisation selection rules, back scattering geometry, (001) surface wafer, see table 2.1 for irreducible representation matrices.

Polarisation		Intensity		
$\mathbf{e}_i$	$\mathbf{e}_s$	$(\mathbf{e}_i \cdot \Gamma_{25'} \cdot \mathbf{e}_s^T)^2$	$(\mathbf{e}_i \cdot \Gamma_{12} \cdot \mathbf{e}_s^T)^2$	$(\mathbf{e}_i \cdot \Gamma_1 \cdot \mathbf{e}_s^T)^2$
[100]	[100]	-	$4b^2$	a^2
[010]	[010]	-	$4b^2$	a^2
[100]	[010]	d^2	-	-
[010]	[100]	d^2	-	-

with very little second order scattering and finally the Γ_1 consists almost entirely of second order scattering.

2.4 Microcrystalline and Amorphous Silicon

2.4.1 Vibrational Analysis of Amorphous Silicon

The Raman spectra of crystalline materials is highly constrained by the selection rules as discussed previously. This is primarily due to the fact phonons have a relatively long lifetime and as a result have energies and momentums that are quite well defined. However in the case of amorphous solids the vibrational modes are much more localised resulting in a shorter

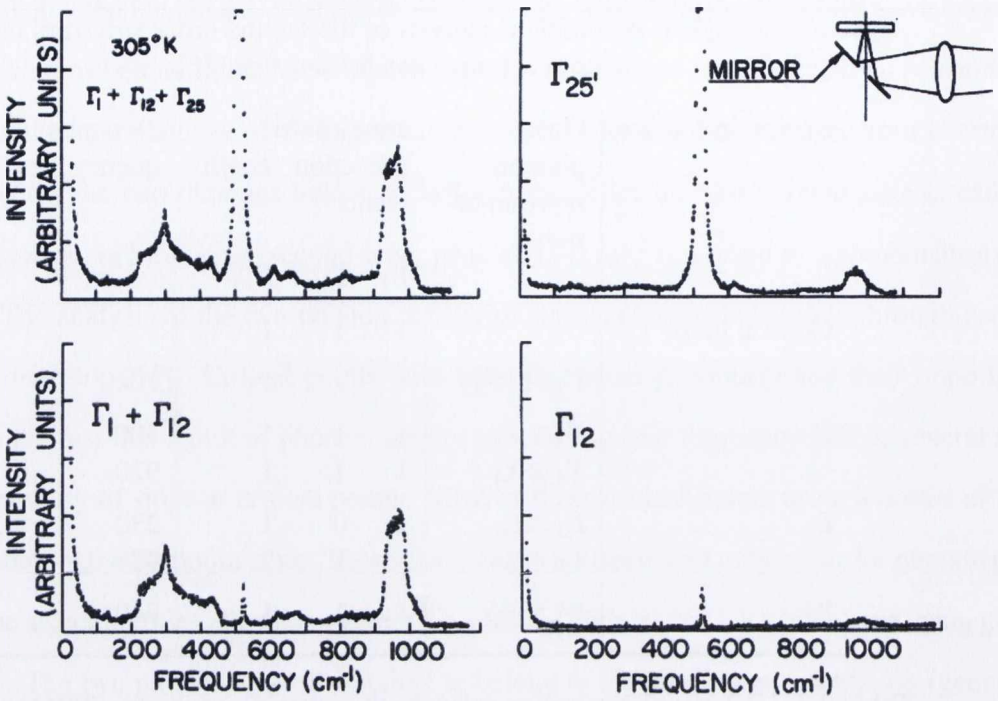

Figure 2.3 – Raman spectra of crystalline Silicon scattering is shown from each Raman active irreducible representations [15].

lifetime. An amorphous solid has *short range* ordering that is strong at a distance up to three or four bond lengths. Beyond this limit longer correlations are not observed.

The Raman spectra shows the Raman active vibrational modes of the sample or in other words the Raman active vibrational density of states. It is possible to deduce this density of states from a disorder induced breakdown in the selection rules [17]. In a perfect harmonic crystal the spatial extent of a normal mode vibrational frequency (Λ) is infinite with a very well defined energy and wavevector. If it is assumed that in an amorphous solid the coherence length of the vibrational mode is short compared with optical wavelengths. The assumption of short coherence lengths yields the breakdown of the usual wave-vector $\mathbf{q} \approx 0$ selection rule. This results in a much sharper damping than that resulting from the degeneration of a phonon into two degenerate phonons which results in the observed linewidth of a fully crystalline crystal, the coherence length of this effect is long compared to the wavelength of light. Vibrational modes of such short spatial duration cannot be characterised by a single

wavevector. This results in the Fourier transform having a broad flat maximum around $\mathbf{q} = 0$ and not peaked at a particular wave vector thereby allowing scattering from essentially all the normal modes of the material. Such that [17] the vibrational mode envelope is now proportional to

$$e^{i\mathbf{q}_j \cdot \mathbf{r}} e^{-\mathbf{r}/\Lambda} \tag{2.24}$$

where $\mathbf{q}_j$ is the wavevector of the jth harmonic mode and $\mathbf{r}$ is the position. Summing over all $\mathbf{q}_j$ the Stokes Raman spectra at a frequency shift ω is then given as [17, 18]

$$I_{\alpha\beta\gamma\lambda}(\omega) = \sum_b C_b^{\alpha\beta\gamma\lambda} \frac{1}{\omega}[1 + n(\omega, T)](\omega_i - \omega)^4 g_b(\omega) \tag{2.25}$$

where

$$n(\omega, T) = [e^{\frac{\hbar\omega}{kT}} - 1]^{-1} \tag{2.26}$$

is the Bose-Einstein occupation number at a temperature T. It is assumed that the normal vibrations fall into bands having similar microscopic motions, frequencies, optical coupling and correlation ranges. Each vibration within these bands is assumed to have an identical coupling constant $C_b^{\alpha\beta\gamma\lambda}$ with the superscripts $\alpha\beta$ and $\gamma\lambda$ describing the polarisation of the incident and scattered photons. $g_b(\omega)$ is the vibrational density of states, ω and ω_i are the phonon frequency and incident photon frequency. If $I^P(\omega)$ is the measured Stokes part of the Raman spectrum incorporating $\alpha\beta\gamma\lambda$ into P then the reduced Raman spectrum is defined as

$$I_R^P(\omega) = \omega(\omega_i - \omega)^{-4}[n(\omega) + 1]^{-1} I^P(\omega) \tag{2.27}$$

The reduced Raman spectrum only involves the density of states and the frequency dependent factors in $C_b^{\alpha\beta\gamma\lambda}$ which are presumed to be smooth and slowly varying.

2.4.2 Raman Spectra of Amorphous Silicon

From experimental spectra two main conclusions can be drawn.

- The first-order Raman spectrum covers the entire vibrational energy, removing the selection rules requiring only the zone centre optical phonon
- The amorphous density of states is very similar to the crystalline density of states.

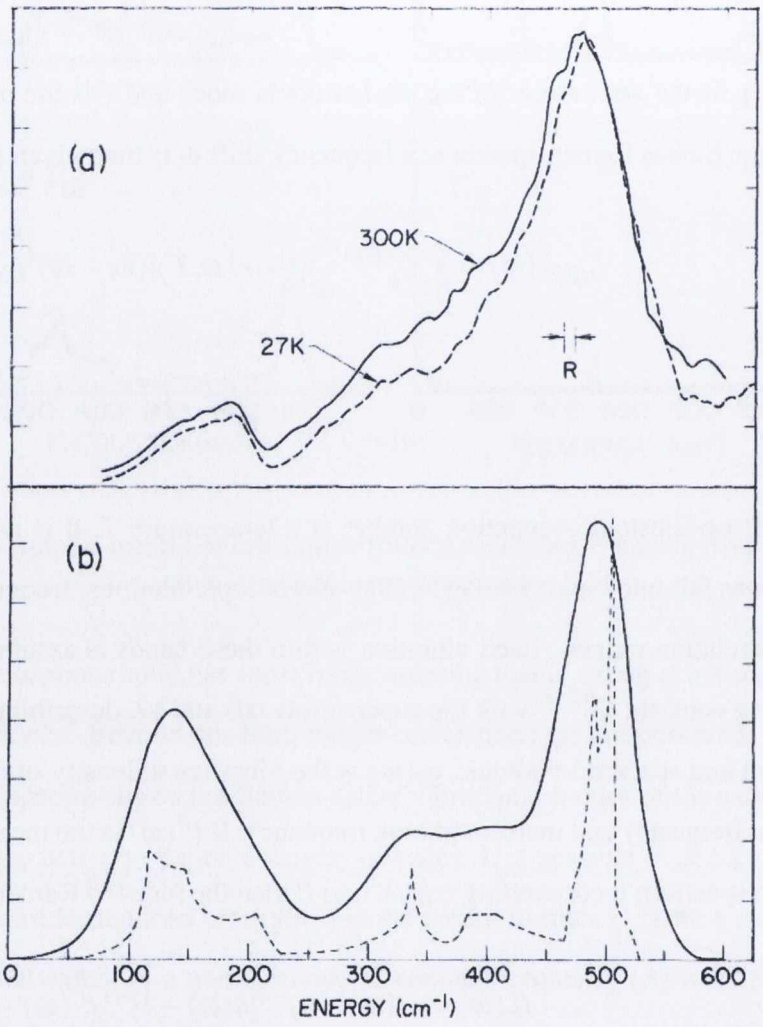

Figure 2.4 – a) Raman spectra of amorphous Silicon at 27 and 300 K reduced by $[n(\omega,T)+1]/\omega$. b) Density of states of crystalline Silicon from Neutron scattering data. The solid line is the crystalline density of states broadened by a convolution with a Gaussian factor of half-width 25 cm^{-1} [19].

Figure 2.4(a) shows the reduced Raman spectrum, in the absence of matrix effects this would be the vibrational density of states, $g_b(\omega)$. Figure 2.4(b) shows the crystalline density of states and a broadened version. The similarity shows that the general features of the

reduced Raman spectra are given by the crystalline density of states, which indicates that the vibrational spectrum is significantly determined by near-neighbour interactions. The weakness in the low frequency modes is due to the band dependence of C_b which in this case was assumed to be equal. The singularities in the crystalline spectra related to the crystallinity have been removed due to the broadening.

It is possible to use a limited number of short range force constants (such as bond stretching and bond bending force constants) to calculate the vibrational spectra. This results from the strong short range nature of covalent bonds and the dominant role of short range forces in determining vibrational spectra as shown in the Raman spectra of amorphous Si 2.4. The Weaire-Alben [20] theorem states that phonon density of states of a tetrahedrally coordinated system subject to a short range potential energy obtained using short range force constants should be as shown in Fig. 2.5(a)

Figure 2.5(b) shows the phonon density of states of crystal Si as determined by fitting Neutron spectroscopy data by a parameterized shell model [21].

2.4.3 Effect of Microcrystal Size on Vibrational Properties

Microcrystalline Silicon is an intermediate case in which the crystal is sufficiently small that confinement effects start to appear. Experimental results also show a peak position shift towards lower energy (also known as a redshift) that is accompanied by a broadening of the linewidth [22]. The shift in the peak position was also shown to increase with decreasing crystalline size. The wave function of an phonon of wavevector $\mathbf{q}_0$ in an infinite crystal is

$$\Phi(\mathbf{q}_0, \mathbf{r}) = u(\mathbf{q}_0, \mathbf{r}) e^{i\mathbf{q}_0 \cdot \mathbf{r}} \tag{2.28}$$

where $u(\mathbf{q}_0, \mathbf{r})$ has the periodicity of the lattice, the phonon in a microcrystallite of diameter L is restricted to the volume. This boundary condition is imposed as [23]

$$\Psi(\mathbf{q}_0, \mathbf{r}) = W(\mathbf{r}, \mathbf{L}) \Phi(\mathbf{q}_0, \mathbf{r}) = \Psi'(\mathbf{q}_0, \mathbf{r}) u(\mathbf{q}_0, \mathbf{r}) \tag{2.29}$$

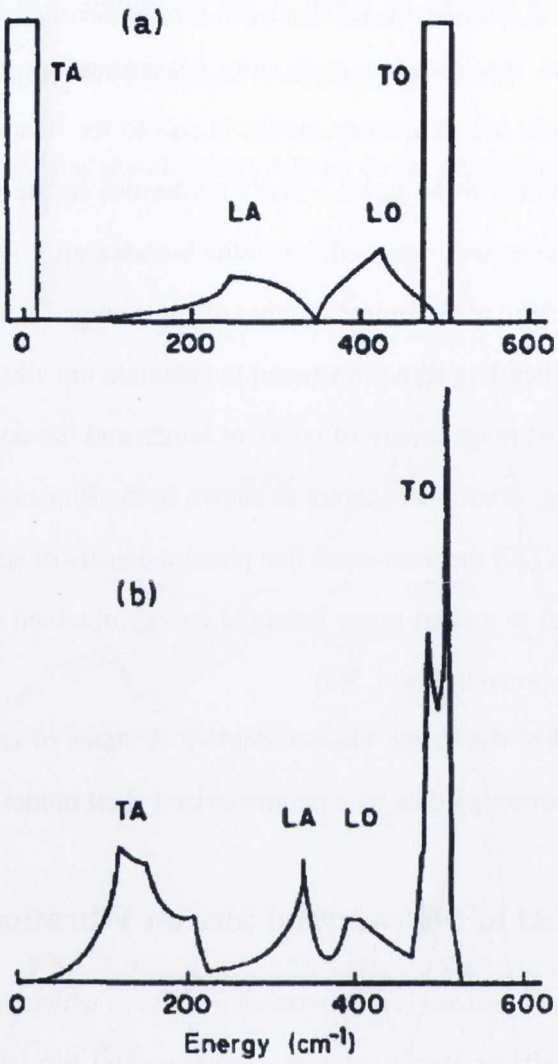

Figure 2.5 – (a) The theoretical phonon spectrum of cubic Silicon using short range force constants [20] (b) Phonon spectrum of Silicon as shell model fitted [21] to experimental Neutron scattering data.

where W is the phonon weighting function. A Gaussian weighting function, has been found to give the best correlation with experimental results [24]. So that

$$\Psi(\mathbf{q}_0,\mathbf{r}) = Ae^{\frac{-2r^2}{L^2}}\Phi(\mathbf{q}_0,\mathbf{r}) = \overbrace{Ae^{\frac{-2r^2}{L^2}}e^{i\mathbf{q}_0\cdot\mathbf{r}}}^{\Psi'}u(\mathbf{q}_0,\mathbf{r}) \tag{2.30}$$

The phonon has now been confined to a region $|\mathbf{r}| \leq L$ with a Gaussian probability distribution so that

$$|\Psi|^2 = A^2 e^{\frac{-4\mathbf{r}^2}{L^2}} \tag{2.31}$$

The Raman spectrum can then be calculated by expanding Ψ' in a Fourier series

$$\Psi'(\mathbf{q}_0, \mathbf{r}) = \int C(\mathbf{q}_0, \mathbf{q}) e^{i\mathbf{q}\cdot\mathbf{r}} d^3\mathbf{q} \tag{2.32}$$

with Fourier coefficients $C(\mathbf{q}_0, \mathbf{r})$ given by

$$C(\mathbf{q}_0, \mathbf{q}) = \frac{1}{(2\pi)^3} \int \Psi'(\mathbf{q}_0, \mathbf{r}) e^{-i\mathbf{q}\cdot\mathbf{r}} d^3\mathbf{r} \tag{2.33}$$

Inserting $\Psi'(\mathbf{q}_0, \mathbf{r})$ from Eqn. (2.30) into Eqn. (2.33) results in

$$C(\mathbf{q}_0, \mathbf{q}) = \frac{AL}{(2\pi)^{3/2}} e^{\frac{-(\mathbf{q}-\mathbf{q}_0)^2(L/2)^2}{2}} \tag{2.34}$$

Due to this localisation $\Psi(\mathbf{q}_0, \mathbf{r})$ is no longer an eigenfunction of the system with a single wave vector but rather a quantum superposition of wave vectors centered around $\mathbf{q}_0$ with a standard deviation, $\sigma = 2/L$. The phonon transition probability $|\langle \mathbf{q}_0 | \hat{O} | \mathbf{q} \rangle|^2$ is therefore not zero for $\mathbf{q}_0 \neq \mathbf{q}$ and has values [23]

$$|\langle \mathbf{q}_0 | \hat{O} | \mathbf{q} \rangle| = |\langle \mathbf{q}_0 | \hat{O} | \mathbf{q}_0 \rangle|^2 C(\mathbf{q}, \mathbf{q}_0)^2 \tag{2.35}$$

where $\hat{O}$ is the photon-phonon interaction operator, $|\langle \mathbf{q}_0 | \hat{O} | \mathbf{q}_0 \rangle|^2$ is a scaler probability and

$$C(\mathbf{q}, \mathbf{q}_0)^2 = \frac{A^2 L^2}{(2\pi)^3} e^{-(\mathbf{q}-\mathbf{q}_0)^2(L/2)^2} \tag{2.36}$$

This is a different situation than the linewidth. In the case of the linewidth Eqn. (2.22) describes the case of a single phonon of wavevector k and the probability that it will emit a frequency that differs from the harmonic case due to its decay into two degenerate phonons

with opposite wavevector. The resulting linewidth describes the energy uncertainty of the phonon due to its rapid decay and is symmetric. In this case we are looking at the *relaxation* of the selection rules so that wave vectors not equal to $\mathbf{k} = 0$ are permitted. Each of these new wave vectors will have a natural linewidth.

Silicon In the case of Silicon this results in non zero transition probabilities for $\mathbf{q}_0 \neq 0$ and $\mathbf{q}_0 = 0$. So

$$C(\mathbf{q},0)^2 = \frac{A^2L^2}{(2\pi)^3} e^{-(\mathbf{q})^2(L/2)^2} \tag{2.37}$$

By examining the dispersion relations for Silicon, Fig. 1.4, it is obvious that the frequency of all the optical phonons surrounding the Γ zone centre phonon have a lower frequency. This results in the asymmetric downshift to a lower frequency of the microcrystalline spectra. The complete spectra is the result of adding the new phonons to the spectra with their natural linewidths as described by Eqn. (2.22) so that the complete Raman spectrum [24] and from Eqn. (2.22) is given by

$$I(\omega) = \int \frac{d^3\mathbf{q}|C(0,\mathbf{q})|^2}{(\omega - \omega(\mathbf{q}))^2 + (\Gamma_0/2)^2} \tag{2.38}$$

where $\omega(\mathbf{q})$ is read from the phonon dispersion curve, Fig. 1.4 and Γ_0 is the natural linewidth. The natural linewidth for microcrystalline Silicon is wider than crystalline Silicon as the momentum conservation rules have been relaxed [23].

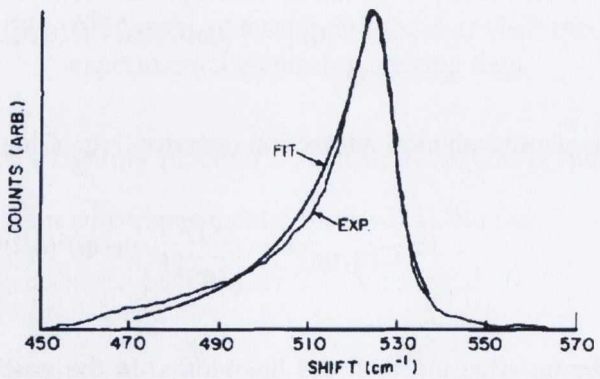

Figure 2.6 – Microcrystalline spectra with crystallite size of 40Å. Asymmetry is visible.

The phonon curves also show that the degeneracy of the Γ zone centre phonon no longer holds. Wave vectors outside this point separate into a doubly degenerate transverse optical (TO) branch and a non degenerate longitudinal optical (LO) branch. The TO branch has a higher frequency than the LO branch.

Chapter 3

Experimental Set up

The micro-Raman scattering measurements were carried out at room temperature in the backscattering geometry using RENISHAW 1000 micro-Raman system equipped with a CCD camera and a Leica microscope. An 1800 lines/mm grating was used for all measurements, providing a spectral resolution of 1 cm^{-1}. 457 (Ar+), 488 (Ar+), 514(Ar+) and 633 (HeNe) nm excitation sources with adjustable power were used. Figure 3.1 shows a standard Raman installation demonstrating all the major component parts.

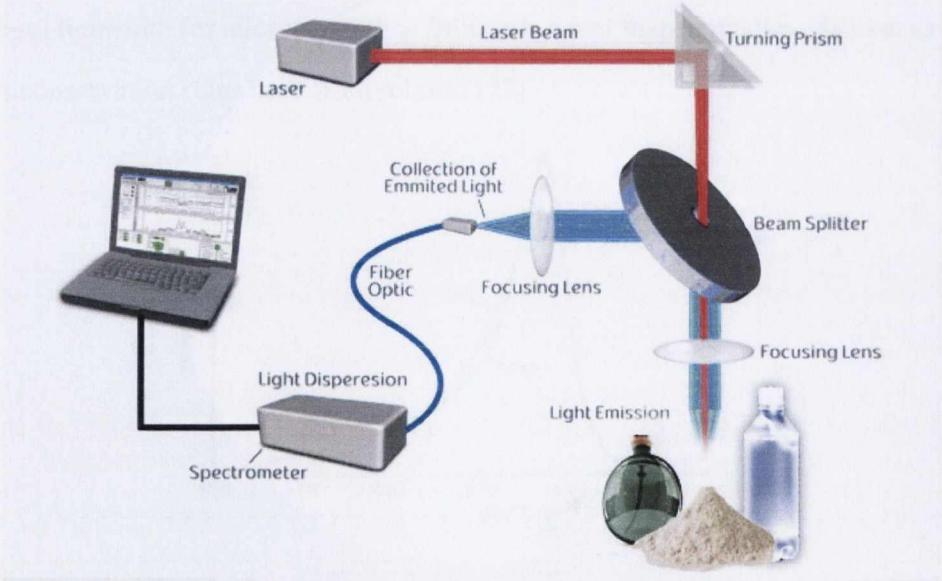

Figure 3.1 – Raman spectrometer installation.

An Ar+ (Argon ion) and HeNe (Helium-Neon) lasers can produce highly monochromatic light and the power density of the focused beam is very high, meaning smaller samples can be investigated. Most of the current dispersive Raman set-ups are now equipped with multichannel two-dimensional CCD detectors. The CCD is much more sensitive than the eye and is able to record a complete Raman spectrum in less than a second. Rayleigh scatter is elastically scattered light of the same wavelength as the laser and so is of no interest. Rayleigh scatter is very intense typically one million times stronger than Raman scatter. If this light is allowed to pass into the spectrograph, it will be so intense as to render it almost impossible to see any Raman spectrum. For this reason Rayleigh scatter must be removed. A holographic notch filter is used to remove this scatter. The holographic notch filter selectively rejects (through Bragg diffraction) a narrow band of light while passing light outside of the band rejection region.

3.0.4 Penetration Depth Dependence on Wavelength

The depth of penetration in a crystalline material depends on the wavelength of the incident light. The total scattered light intensity integrated from the surface to a depth, d, I_s is given by [25]

$$I_s = I_0 D \int_0^d e^{-2\alpha x} dx = \frac{I_0 D}{2\alpha}(1 - e^{-2\alpha d}) \tag{3.1}$$

while that from the depth d to infinity is

$$I_d = I_0 D \int_d^\infty e^{-2\alpha x} dx = \frac{I_0 D}{2\alpha} e^{-2\alpha d} \tag{3.2}$$

I_0, D and α are the incident light intensity, The Raman scattering cross section and the photoabsorption coefficient respectively. The penetration depth, d_p, is the depth that satisfies the relationship

$$\frac{I_d}{I_s + Id} = 0.1 \tag{3.3}$$

and is given by

$$d_p = \frac{-\ln 0.1}{2\alpha} = \frac{2.3}{2\alpha} \tag{3.4}$$

The absorption coefficients for Silicon and Germanium for different wavelengths can be found using Eqn. (3.4) and the absorption coefficients, see Figs. 3.2a and 3.2b

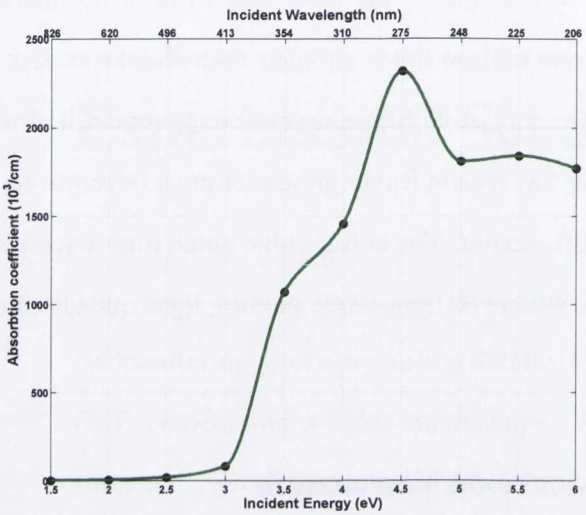

(a) Silicon absorption coefficients

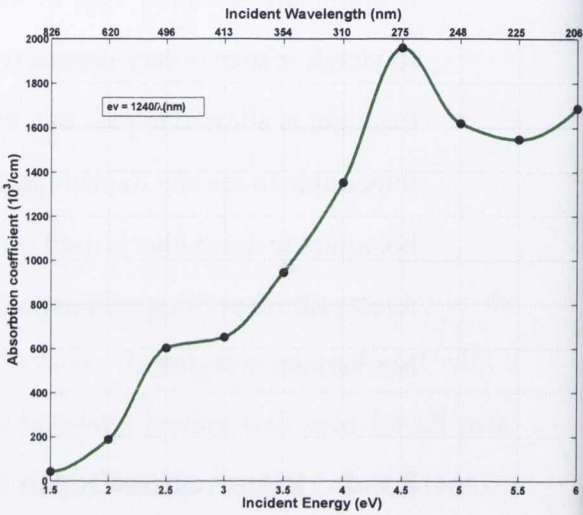

(b) Germanium absorption coefficients

Figure 3.2 – Silicon and Germanium absorption coefficients, interpolated from discrete values given in [26]

The results for several popular laser wavelengths are summarized in Table 3.1

Table 3.1 – Penetration depths of Silicon and germanium for popular laser wavelengths.

		Silicon		Germanium	
λ(nm)	λ(eV)	$10^{-3}\alpha(\text{cm}^{-1})$	d_p (nm)	$10^{-3}\alpha(\text{cm}^{-1})$	d_p (nm)
457.9	2.708	36.43	320	625.8	18
488.0	2.541	20.18	570	610.2	19
514.5	2.410	14.96	770	569.3	20
633.0	1.958	3.911	2940	168.3	68
785.0	1.580	0.893	12875	49.28	233

In the majority of cases experiments were run with backscattering geometry on wafer surfaces. Microelectronic substrates always have a (001) surface. Equation (2.9) describes the selection rules and their dependence on the polarisation directions of the incident and

scattered light and the Raman tensor.

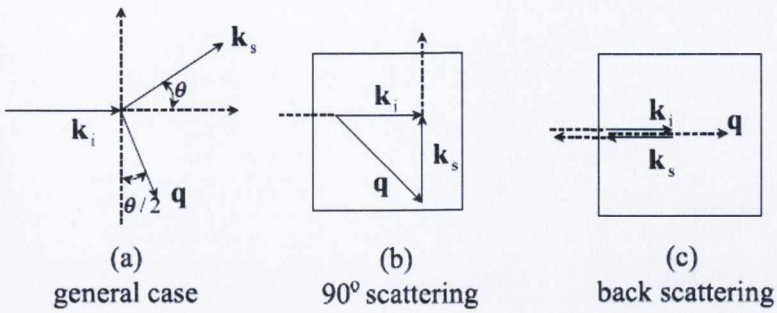

Figure 3.3 – Geometry of light scattering. (a) general case, (b) right angle (90°) scattering geometry and (c) back scattering geometry. $\mathbf{k}_i$ is the wave vector of the incident photon, $\mathbf{k}_s$ is the wave vector of the scattered photon and $\mathbf{q}$ is the phonon wave vector. [10]

Various scattering geometries are shown in Fig. 3.3. In the case of backscattering geometry with light incident on a (001) surface wafer the selection rules only allow a single phonon mode to be visible, $F_2(z)$ in Table 2.1. This occurs as the other two phonons have matrix elements that require the incident or scattered light to have at least one component in the z direction which is impossible, as in the back scattering set up this direction is the direction of incident light propagation and scattered light collection. The z-axis is the axis of the incident light and the polarisation directions must then be perpendicular to this axis so that

$$\mathbf{e}_i \perp z \text{ and } \mathbf{e}_s \perp z \tag{3.5}$$

The three Raman tensors from Table 2.1 can then be written

$$R_x = \begin{bmatrix} 0 & 0 & 0 \\ 0 & 0 & d \\ 0 & d & 0 \end{bmatrix}, R_y = \begin{bmatrix} 0 & 0 & d \\ 0 & 0 & 0 \\ d & 0 & 0 \end{bmatrix}, R_z = \begin{bmatrix} 0 & d & 0 \\ d & 0 & 0 \\ 0 & 0 & 0 \end{bmatrix} \tag{3.6}$$

The selection rules with backscattering geometry on a (001) surface are

$$I = A \left(\mathbf{e}_i \cdot \begin{bmatrix} 0 & d & 0 \\ d & 0 & 0 \\ 0 & 0 & 0 \end{bmatrix} \cdot \mathbf{e}_s^T \right)^2 \tag{3.7}$$

depending on the polarisation directions of the incident and scattered light several different Raman intensities ranging from zero to $A(-2d)^2$ are possible, Table 3.2 shows a selection.

Table 3.2 – Polarisation selection rules, back scattering geometry, (001) surface wafer.

Polarisation		**Intensity**
$\mathbf{e}_i$	$\mathbf{e}_s$	$A(\mathbf{e}_i \cdot R_z \cdot \mathbf{e}_s^T)^2$
[100]	[100]	-
[100]	[010]	$A(d)^2$
$[1\bar{1}0]$	$[1\bar{1}0]$	$A(-2d)^2$
[110]	$[1\bar{1}0]$	-

The excitation source is generally polarised but the scattered light is unpolarised. However, with the addition of polarisation plates it is possible to polarise the scattered light. By rotating the Silicon wafer it is possible to change the polarisation direction of the incident light with respect to the crystallographic axis of Silicon. This can also be achieved by insertion of a $\pi/2$ plate in the incident light beam.

Chapter 4

Stress Analysis of Laser Machined Silicon

4.1 Introduction

Over the last four decades the semiconductor industry has advanced at a relentless pace, although semiconductor fabrication was never cheap or easy it seems that in recent generations the basic process behind miniaturisation, that of shrinking the transistor dimensions, is no longer straightforward and increasingly engineers are collaborating with physicists, chemists and material scientists in an attempt to develop the next generation of technology.

The transistor and its surrounding structures from the basic Silicon substrate to the material in the global interconnects has undergone a radical change in recent years and in many cases ideas that were previously discarded as too complex or simply impossible are being revisited as the enormous resources of the global semiconductor industry strives to follow Moore's law [27]. Despite the enormous achievements already made, new challenges requiring innovative solutions are always on the horizon and despite the advances so far unequalled in any other industry constant change is a given.

Increasingly, 3D technology is seen as a potential solution to many of these problems and research interest has increased in recent year [27]. A three-dimensional integrated circuit

is a die with two or more layers of active electronic components, integrated both vertically and horizontally into a single circuit. For example, a high speed imaging application could require detectors on one layer and the first stage of processing circuitry immediately below on another layer. The number of detectors in an array could be increased and the speed of signal processing would also improve as signals would travel a shorter distance. This differs significantly from 3D packaging also known as System in Package (SiP), where multiple chips are packed together vertically and communicate using off chip signalling in the same way as if they had been placed next to each other on a PCB but this approach still presents latency, bandwidth and power problems due to growing circuit density and complexity.

The key advantage of 3D circuits is to dramatically reduce the length of global interconnects as 3D interconnects could be highly optimised to save space. This design allows more transistors to be placed within a clock cycle of each other dramatically increasing performance and removing the requirement for booster transistors. Long power hungry global interconnects connecting distant parts of the wafer together could be greatly reduced as distances to different parts of a 3D circuit would be much shorter when compared to a 2D circuit with an identical wafer area. Resistance losses can also be effectively removed using special heat conducting thermal vias, allowing heat dissipation in three dimensions. Different semiconductor layers using different substrate materials and processing techniques can be mixed together, for example elemental semiconductors like Silicon in the carbon group (IV) can be aggregated into a compound semiconductor material in the Boron-Pnicitain (III-V) group. The trend towards general purpose IC design would be accelerated. Devices such as memory, field programmable data arrays (FPGAs), logic circuits and other generic devices could be stacked. High volume production of these generic components reduces cost. Allowing the use of legacy equipment while introducing performance and cost benefits is of major economic importance. In this chapter laser machined samples with uses in 3D manufacturing are investigated and Raman spectroscopy is used to investigate the stress in the Silicon substrate resulting from damage due to laser ablation. Theoretical analysis of the change in the Raman spectra due to stress is also presented.

4.1.1 Through Silicon Vias

Through Silicon vias (TSVs), are seen as the key technology allowing 3D circuits to become a reality. Essentially they are small via structures created in the Silicon substrate. After the via is drilled barrier metals are deposited onto the sidewalls and the via is filled with copper interconnect material. The wafer is thinned until the copper bottom of the via is exposed.

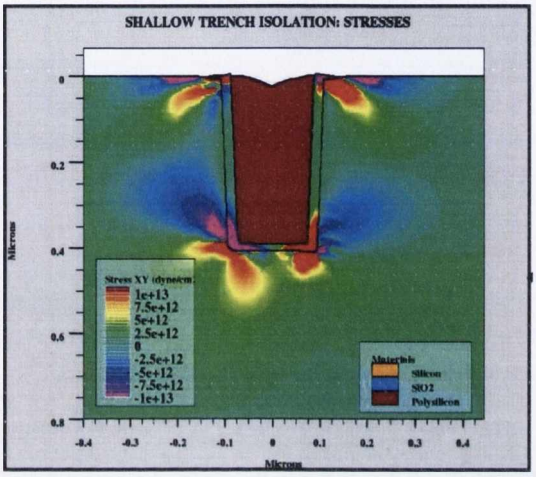

Figure 4.1 – Stress state surrounding an etched via modelled with Silvaco ATLAS device simulation framework [28].

Conventionally corrosive plasmas have been used in the formation of TSVs. The most popular techniques currently used to create TSVs and Microelectromechanical systems (MEMS)[29] are Reactive Ion Etching (RIE) which makes use of the high energy ions contained in chemically reactive plasma, Fig. 4.1 shows a model of the stress in a chemically etched TSV. This process ablates the wafer surface using a lithography process to mask the wafer and create the desired patterns. Alternatively Bosch Deep Reactive Ion Etching (DRIE) is similar to RIE but is more effective at creating deep holes [30]. For RIE processing, a Plasma Enhanced Chemical Vapour Deposited (PECVD) Silicon dioxide layer is used as an etch mask while photoresist is normally the material used for DRIE. If wet etching is used the vias are normally etched using a diluted solution of hydrofluoric acid (HF). If RIE is used the sidewall taper is often too large as shown in Fig 4.2 (a). Alternatively the DRIE process produces highly vertical sidewalls using a gas cycling scheme that alternates etch (SF_6) and sidewall

passivation (C_4F_6) gases. The etch tends to dissolve the passivation layer and ablate only the bottom of the via and not the sidewalls allowing excellent diameter/height ratios. However the challenge for this process is in achieving the desired sidewall taper. By increasing the time of the etch cycle compared to the passivation cycle this can be obtained [31]. DRIE does however have a serious disadvantage as alternating etch and passivation cycles causes scallops to form on the sidewalls due to the isotropic nature of the etch cycle [32] as observed in Fig. 4.2 (b). This scalloping may cause problems in subsequent processes when the vias are lined with barrier metals (normally Tantalum to protect the Silicon from the corrosive copper interconnects [33]) as it is difficult to effectively line the via using PECVD or similar methods without first removing the scallops and significantly affecting throughput [34]. The taper of the sidewalls is also very important if the sidewalls are to be effectively coated as if the sidewalls are too steep they will not be uniformly lined using conformal spluttering [35]. Filling the lined via with copper is another important step that is affected by scallops as they occlude the sidewall and can result in defective plating and the formation of air bubbles [35]. After these steps have been completed the wafer is thinned until the metallized vias are exposed.

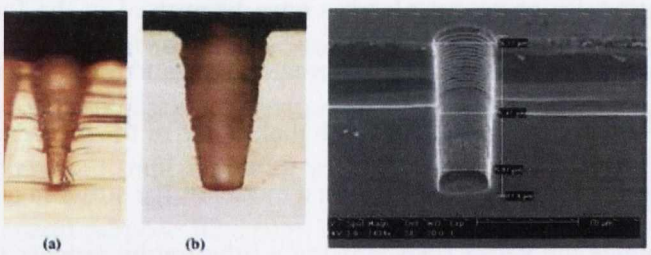

(a) Optical micrograph of RIE via etch profiles (a) sidewall taper is too large (b) desired sidewall taper [32]

(b) SEM image of DRIE via etch profile illustrating sidewall taper [32]

Figure 4.2 – Sidewall tapers.

The limitations described above and the large investment required using these fabrication techniques mean that TSVs have so far only appeared in high-end products.

XSiL Ltd., a Dublin based semiconductor equipment maker that was based in Dublin was the original company partner for this PhD work. XSil Ltd had developed a number of innovative laser micro-machining systems for high volume manufacturing for the semiconductor, opto-electronic and bio-medical sectors in particular laser drilling of through Silicon vias where high powered ultra-violet high repetition Diode-Pumped Solid-State (DPSS) lasers were used to ablate the Silicon and create vias.

The key difference between laser and the alternative etching techniques is the lack of a lithography step this significantly simplifies the via fabrication flow as no masks are needed and eliminates the need for expensive etching equipment, consumables and high level clean room environments. Laser ablation could have important applications for Silicon dicing, and many of the results and conclusions drawn could be applicable to both drilling and dicing. Tradionally dicing is a mechanical process using a diamond saw. Unfortunately this process can lead to significant debris accumulating around the diced area. High stress areas that can potentially lead to failure are also a concern.

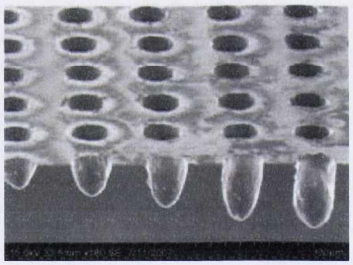

Figure 4.3 – Scanning Electron Microscope (SEM) image of laser drilled vias from XSiL.

Of the known laser drilling regimes (helical, trepanning and percussion) only percussion provides a significant throughput advantage over DRIE [36]. In a percussion drilling regime a consecutive sequence of laser pulses are focused on the same point to drill a via of fixed depth and diameter. The number of laser pulses and the pulses and the pulse energy dictate via depth, the beam size governs the via diameter while the overall drill rate is determined by the laser repetition rate and the speed at which individual vias can be addressed, see Fig. 4.3 for an example of a laser drilled TSV. As the pulse energy determines the depth of the vias,

excellent depth uniformity (4%) can be achieved over a large 300mm wafer unlike many current DRIE processes [36]. XSiL Ltd. had achieved a 50 fold increase in via drilling rates, and used a technique that enables ablation rates of approximately 20 μm per pulse [37]. Fig. 4.4 show the relationship between drill rate, depth and diameter, showing that larger diameter vias have a lower drill rate.

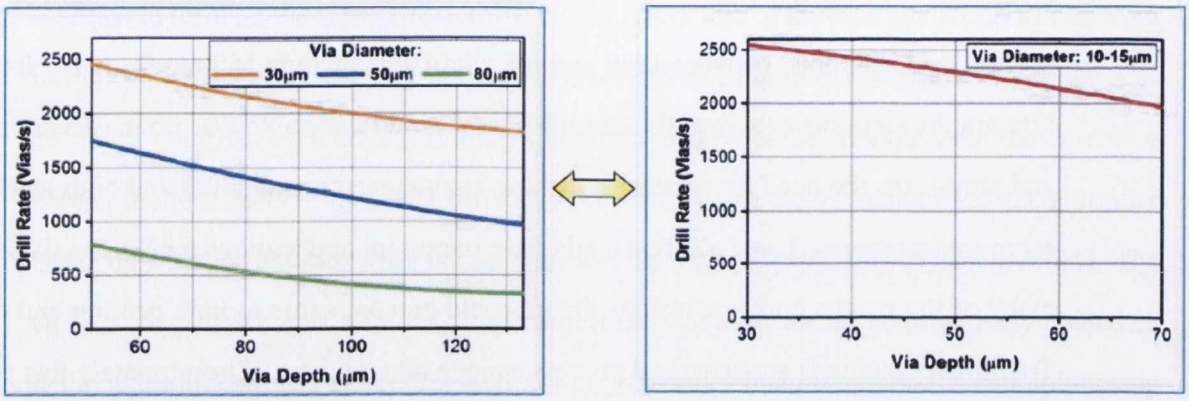

Figure 4.4 – Laser drilling rates achieved by XSiL.

The sidewalls of the laser process developed by XSil were very smooth without any scalloping removing the limiting factor in DRIE via formation and approach the optimal 85° angle considerable simplifying and accelerating meallization, low surface roughness of approximately 0.12μm have been measured using a white light inferometer [36].

Via diameters ranging from 15-80μm are currently available using existing technology. The main impediment to attaining large via diameters is imposed by the maximum pulse energy available from the industrial UV high repetition DPSS lasers [36]. However large vias in Silicon are not of interest for interconnect applications, see Fig. 4.5. Limitations for small diameter vias arise from opto-mechanical restrictions, spherical aberrations in commercially available scan lenses, trade off between focal length, separation between scanning mirrors in galvanometer, hazards of scan lens contamination by the ejected plume and effective throughput reduction with smaller scan field [38]. However research is ongoing in this area and substantial diameter reduction $< 2 - 3\mu$m is envisioned by precise control of instantaneous power with picosecond lasers and other emerging technologies.

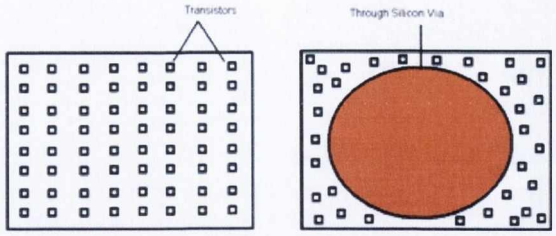

Figure 4.5 – Size of large TSVs in comparison with transistor dimensions.

4.1.2 Ablation process

The mechanism through which laser induced ablation occurs is dependent on the power or flux of the laser at low laser flux. The material is heated by the absorbed laser energy and evaporates. At high laser flux, the material is converted to a plasma. For vias of the size required to be useful in Silicon, ablation occurs primarily through stationary melt displacement and ejection [17] when the ablation and vapour pressures present are significant enough to eject the molten material acting like a piston in the hole and forcing the melt up and out along the sidewalls. The melt tends to adhere to the sidewalls leaving a thick crystallised porous layer behind, see Fig. 4.6.

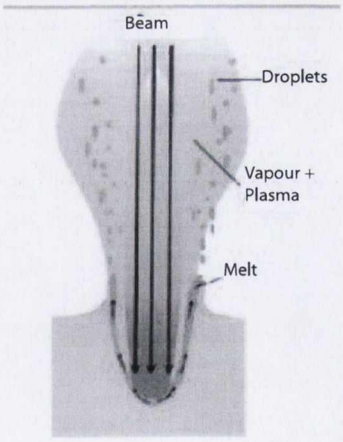

Figure 4.6 – Drawing showing ablation process and melt ejection [39].

One of the most important issues is thermal damage, although damage compares favourably to vias drilled in metals, as Silicon has a much lower thermal conductivity. The thermal effects have the potential to damage the surrounding Silicon by introducing material defects

and amorphous regions.

Depth, diameter and scale of material damage depend on pulse energy, pulse length, power density and the intensity distribution across the beam on the target. In particular energy transport away from the via determines the extension of the heat affected zone. The studies in [40] and [30] using Transmission Electron Microscopy (TEM) give a detailed analysis of the mechanical effects introduced by laser drilling as shown in Fig. 4.7.

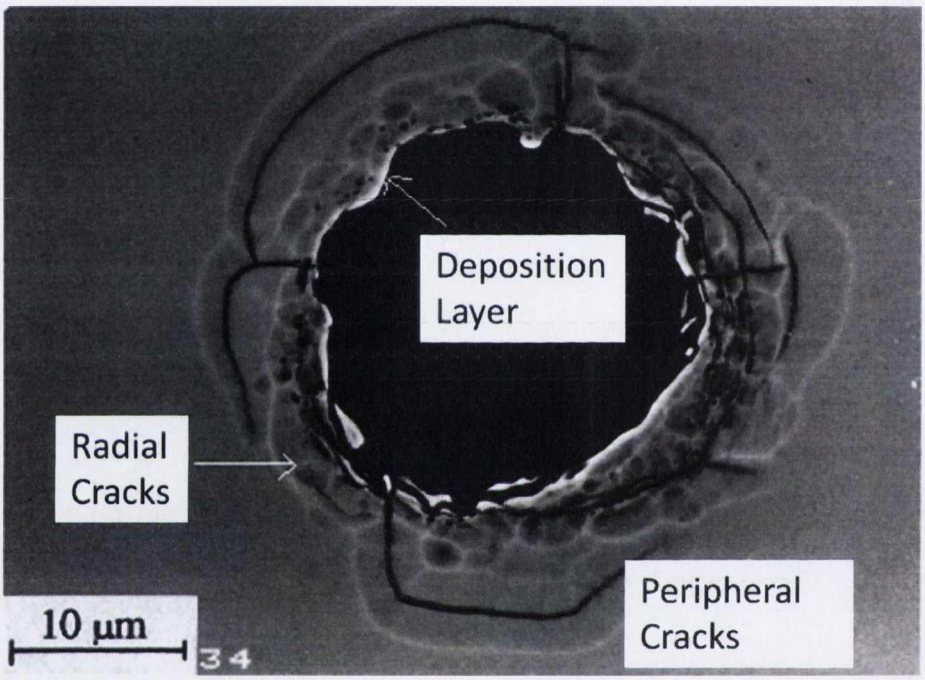

Figure 4.7 – Ion-polished cross-section through a via laser drilled in Silicon. Note the pore-containing deposition layer and the radial and peripheral cracks [40].

The amount of heat diffused into the Silicon substate in the direction of drilling is claimed to be a comparatively lesser problem than heat diffusion into the side walls of the via [40]. In addition the width of the heat affected zone observed on the wall of the hole is not dependent on the duration of the pulses and generally does not extend more than 10 μm.

4.2 Description of Samples

XSiL provided 11 samples fabricated in the following way: each sample was drilled using a UV DPSS laser, with pulses lasting several nanoseconds. The pulse energies ranged from 450 μJ/pulse to 1100 μJ/pulse depending on the diameter of the fabricated via. The laser beam was focused through an iris to ensure a spherical beam diameter and then passed through a series of mirrors and lenses and an optical galvanometer. Electromagnetically controlled mirrors were used to ensure accurate and fast positioning before eventually ablating the Silicon surface. As the scanning field of the galvanometer can only cover a small area the Silicon must be moved using a motorised process that significantly slows down the drilling rate. UV light allows a maximum hole diameter of 5 μm as the light cannot be focused any further.

Table 4.1 – Description of samples. M = Multistep, S = Singlestep (many pulses all one after another, MC = Multistep Circular polarisation, SC = Singlestep circular polarisation, SL = Singlestep Linear polarisation.

Sample Name	Diameter, μm	F, kHz
S2 S	15	-
S3 S	30	-
S4 S	50	20
S5 S	80	-
S6 MC	30	30
S7 SC	30	30
S8 SL	30	30
S9 M	30	20
S10 S	25	20
S11 M	30	10

The polarisation of the laser is determined by the direction of oscillation of the electric field, perpendicular to the propagation direction of the laser beam.

Multistep drilling is a cyclical process, each cycle one laser pulse is used to increase the depth of the via before moving onto the next via and returning to the initial via at the start of the next cycle. This is a slower process but allows for smoother vias as the dust cloud from the first pulse has had time to disperse. During singlestep drilling, the via is completed in one step using sequential laser pulses.

XSiL also supplied Silicon that had been cut or nicked using laser ablation as an alternative to a mechanical saw. Division using a mechanical saw can lead to wafer damage such as chipping and cracking which reduced the strength of the wafer. This is particularity prevalent in thin wafers used in 3D manufacturing. A magnified image using SEM of the diced wafer is shown in Fig. 4.8

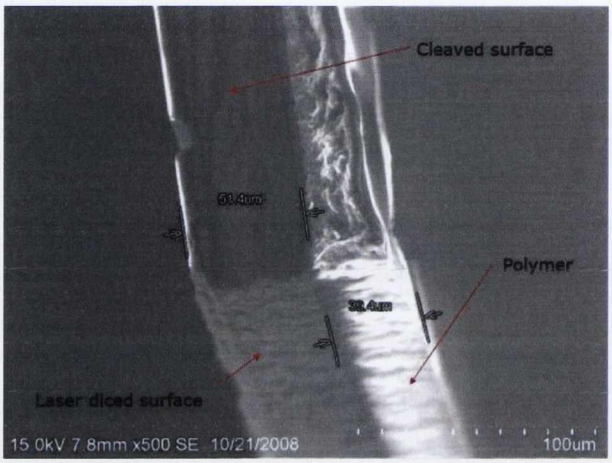

Figure 4.8 – Laser diced wafer, oriented so that the corner and two edges are visible

4.3 Raman Application to Stress Measurements of Silicon

The three Raman tensors in unstrained Silicon from table 2.1 are

$$R_x = \begin{bmatrix} 0 & 0 & 0 \\ 0 & 0 & d \\ 0 & d & 0 \end{bmatrix}, R_y = \begin{bmatrix} 0 & 0 & d \\ 0 & 0 & 0 \\ d & 0 & 0 \end{bmatrix}, R_z = \begin{bmatrix} 0 & d & 0 \\ d & 0 & 0 \\ 0 & 0 & 0 \end{bmatrix} \tag{4.1}$$

The frequencies of the three optical modes in the presence of strain, to terms linear in the strain, can be obtained by solving the following secular equation [41, 42] for the three eigenvalues, λ_j $(j = 1, 2, 3)$.

$$\begin{vmatrix} p\varepsilon_{xx}+q(\varepsilon_{yy}+\varepsilon_{zz})-\lambda_j & 2r\varepsilon_{xy} & 2r\varepsilon_{xz} \\ 2r\varepsilon_{xy} & p\varepsilon_{yy}+q(\varepsilon_{xx}+\varepsilon_{zz})-\lambda_j & 2r\varepsilon_{yz} \\ 2r\varepsilon_{xz} & 2r\varepsilon_{yz} & p\varepsilon_{zz}+q(\varepsilon_{xx}+\varepsilon_{yy})-\lambda_j \end{vmatrix} = 0 \quad (4.2)$$

Here p, q and r are material constants, the phonon deformation potentials, and ε_{ij} are the strain tensor components. The difference between the Raman frequency of each mode in the presence of stress, $\omega_j (j = 1, 2, 3)$, and in the absence of stress, ω_{j0}, can be calculated from the eigenvalues λ_j. Then the Raman tensor in the presence of strain is the sum of the unstrained tensors weighted by the coefficients

$$R^j = \xi_x^j R_x + \xi_y^j R_y + \xi_z^j R_z \qquad j = 1, 2, 3 \quad (4.3)$$

where ξ^j is the eigenvector of eigenvalue λ_j. The through Silicon vias were drilled on a wafer with a (001) surface so the selection rules, eqn. (3.7), limit the Raman tensors to

$$R^j = \lambda_z^j R_z \qquad j = 1, 2, 3 \quad (4.4)$$

The Raman peaks for the individual modes separate under various strain states. However, under the constraint of small strains, the peaks do not fully resolve experimentally, and the observed spectrum appears as a net single, shifted, and broadened peak [43]. Despite the complexity of the stress tensor the assumption that the wavenumber of the Raman peak increases with compressive stress and decrease with tensile stress, the uniaxial assumption has been found to be valid [43, 44, 45]. Koseski, calculated the Raman strain tensor using finite element analysis and then calculated the Raman shift resulting from this strain tensor

as shown in Fig. 4.9

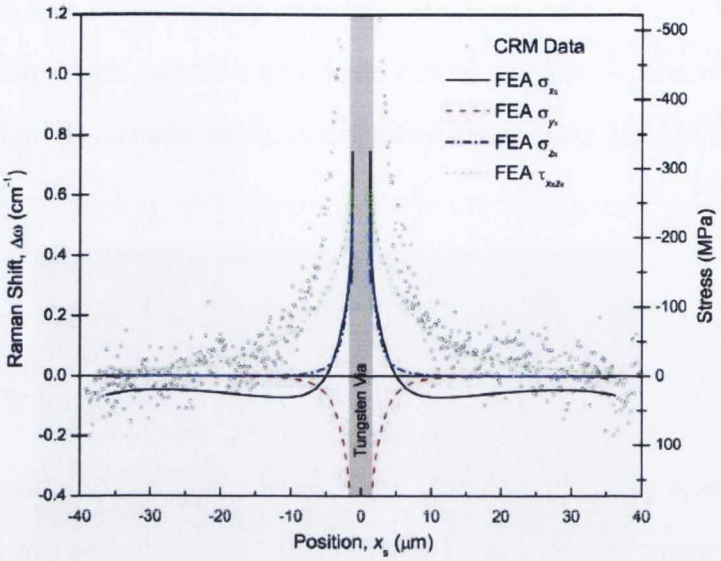

Figure 4.9 – Plot of stress and experimental confocal Raman results surrounding a TSV. Four of the six components of the stress tensor are calculated using finite element analysis, the other two have negligible contribution [43]

.

To preform the stress calculation eqn. (4.5) is used [46]. A peak shift of 1 cm^{-1} corresponds to a shift of about 500 MPa for uniaxial stress.

$$\omega_s \approx \omega_0 + \frac{\lambda_j}{2\omega_0} \tag{4.5}$$

Single Spot mapping of vias

The aim of this section was to build up an overall map of the primary locations of stress and strain of the XSiL samples. The areas immediately surrounding the vias, the sidewalls and the bottom of the via were given particular attention. Any large strains that were found were further investigated and more measurements taken in the area surrounding the sample. After the initial spectrometer calibration, further calibrations were performed approximately after every 2-3 hours in accordance with best practice [45] requiring the substitution of the measured sample with the Silicon reference. Each measurement took approximately 3 minutes and a total of 820 measurements, not including calibration measurements were taken over a

period of several weeks. As the Silicon peak is so strong only one accumulation with a registration time of two seconds was required however the set of measurements was collected two to three times for each via. For relaxed Silicon the Si-Si band peak is located at 520 cm^{-1}. Under compressive stress this peak is shifted to a higher frequency, while for tensile stress the peak is shifted to a lower frequency of the Raman spectrum as shown in Fig. 4.10.

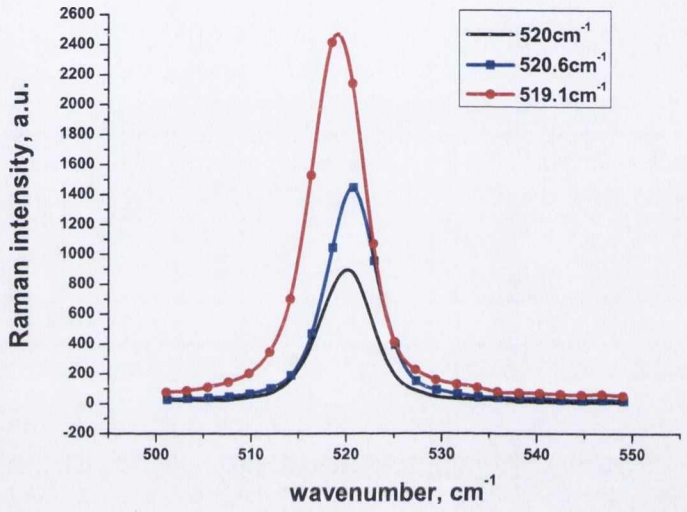

Figure 4.10 – Raman spectra registered at different positions on a via sample, the change in peak position are due to stress.

Optical microscope images were taken for each of the samples and a coloured dot was placed at every point where a stress measurement was taken. Figs. 4.11-4.17 are a representation of the results. As can be seen from Fig. 4.11 tensile stress is very prevalent especially around the via mouth and upper sidewalls while compressive stress is predominant at the bottom of the via structure. In Fig. 4.12 the optical microscope image of the badly damaged structure of sample s3 is shown. As can be seen from this figure primarily tensile stress is present in the area surrounding the via. Figs. 4.11-4.17 show that the multistep and singlestep drilling processes had very few visual differences. The majority of the points had stress of less than 150MPa and the stress tended to be concentrated at the bottom of the via or around the via lip.

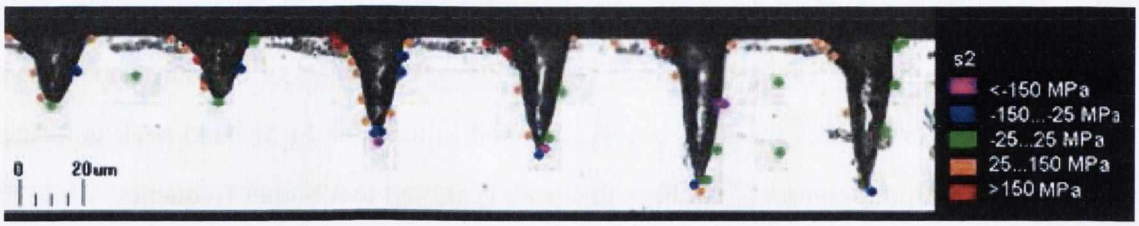

Figure 4.11 – The optical microscope image of sample s2, with diameter at surface, $\varnothing$=15μm. Coloured dots are shown where Raman measurements were taken. Each colour represents the calculated range of stress obtained.

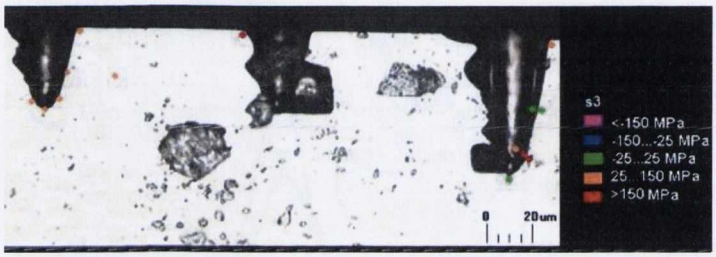

Figure 4.12 – The optical microscope image of sample s2, with diameter at surface, $\varnothing$=30μm. The coloured dots represent the calculated stress range.

Figure 4.13 – Sample s4, $\varnothing$=50μm, singlestep: primarily tensile stress uniform along sidewalls and generally less than 150MPa.

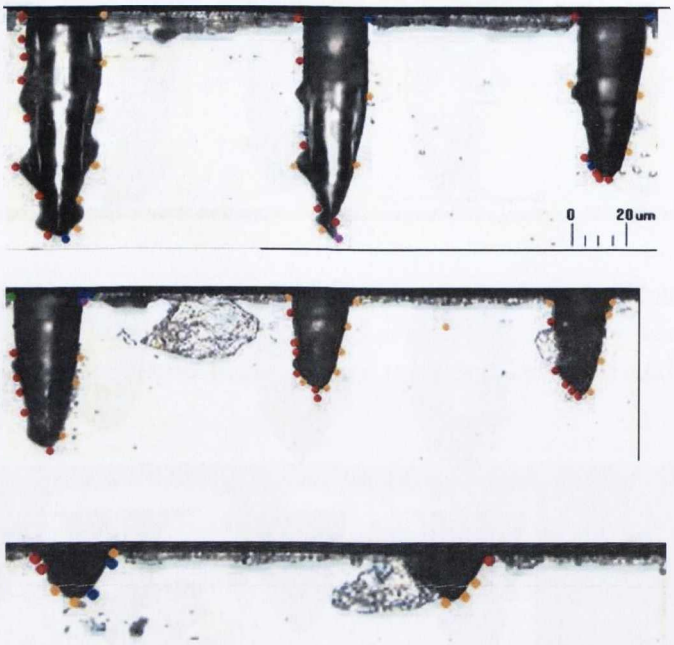

Figure 4.14 – Sample s6, ⌀=30 μm, multistep circular polarisation: sidewalls uniform stress, damaged sidewalls at deeper depths.

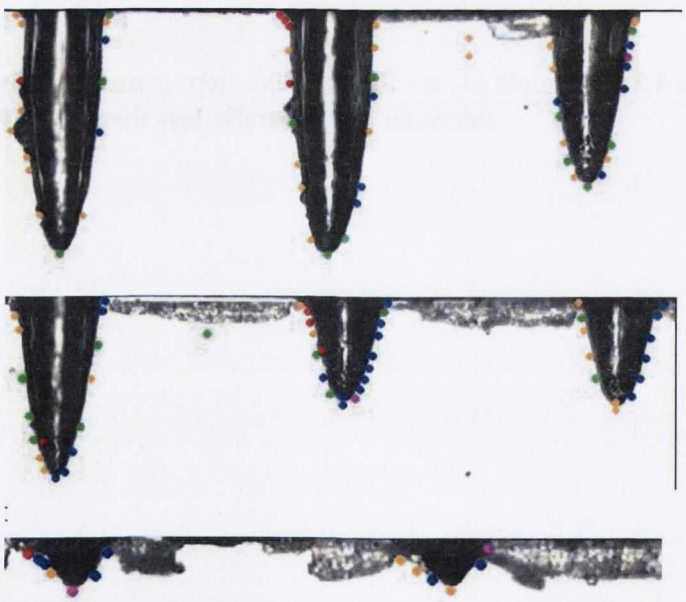

Figure 4.15 – Sample s7, ⌀=30μm, singlestep circular polarisation: very smooth deep vias with lows stresses in sidewalls.

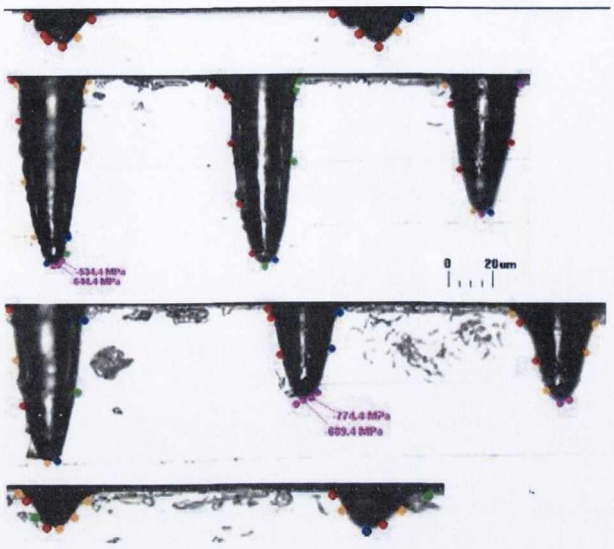

Figure 4.16 – Sample s10, $\varnothing$=25μm, singlestep laser drilling: Stress on left seems higher in middle via.

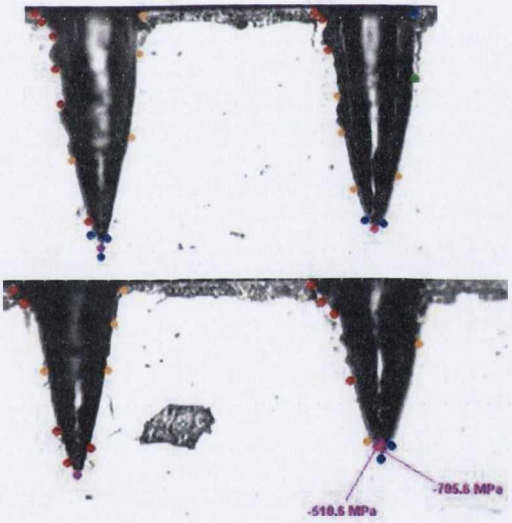

Figure 4.17 – Sample s11, $\varnothing$=30μm, multistep: Compressive stress at base of via and uniform sidewall stress.

Line mapping of vias

After the single spot analysis of the vias, Raman line mapping was used to see how the stress varies along a horizontal line of length 10 μm with its origin at the edge of the via and approximately 10 μm below the surface as shown in Fig. 4.18.

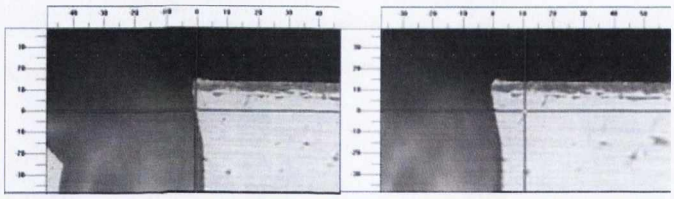

Figure 4.18 – Line mapping start (left) and finish (right) positions.

Each result was automatically compared to a fitted reference curve, in this case the fitting spectrum was obtained from a relaxed Silicon wafer that was used for calibration. Line maps could then be generated showing how the fitted experimental data differed from the original reference. The variation of different parameters such as peak position, peak width and peak intensity with position along the line-mapping length could then be graphically plotted. A sample of the plots received is seen in Figs. 4.19-4.24.

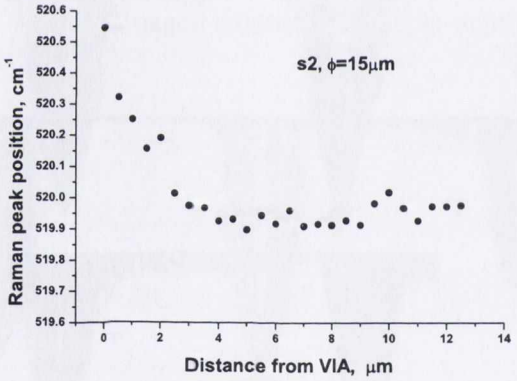

Figure 4.19 – The dependence of the Silicon peak position on the position of the measured spot. Starting from the edge of the via in sample s2.

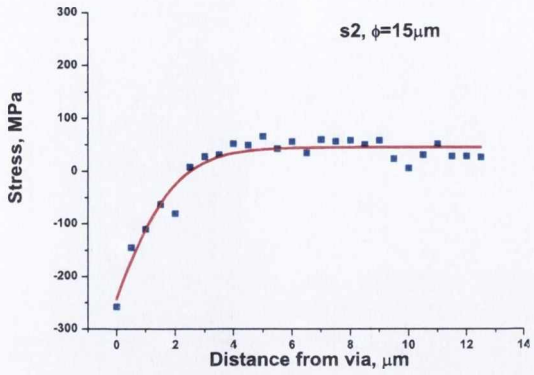

(a) Sample 2

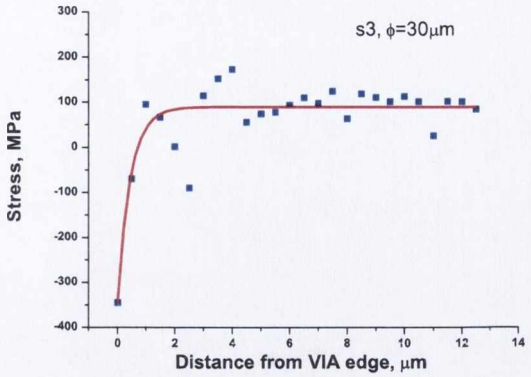

(b) Sample 3

Figure 4.20 – The dependence of the stress on the position for samples s2 and s3.

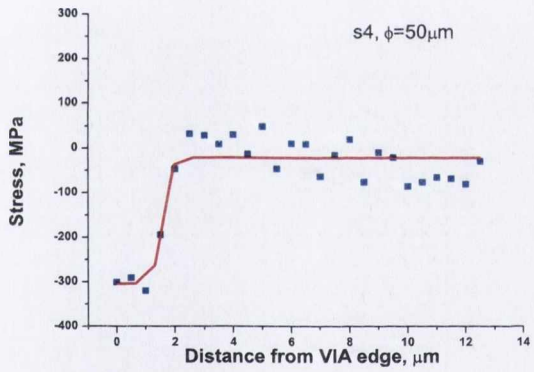

(a) Sample 4

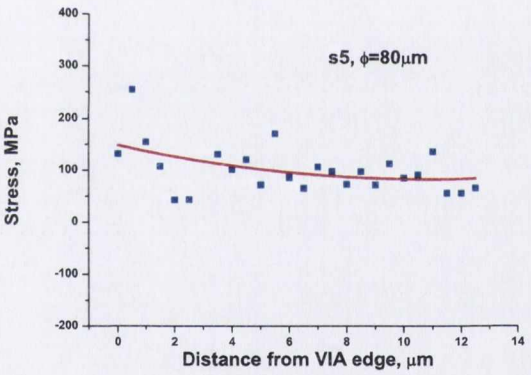

(b) Sample 5

Figure 4.21 – The dependence of the stress on the position for samples s4 and s5.

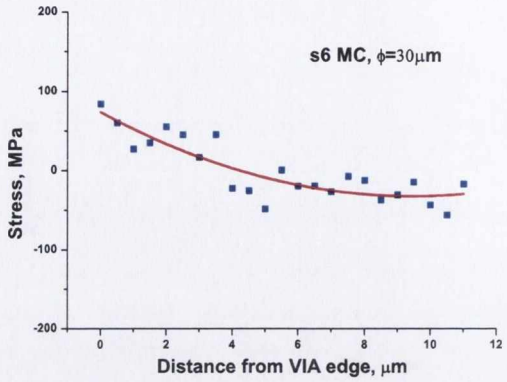

(a) Sample 6

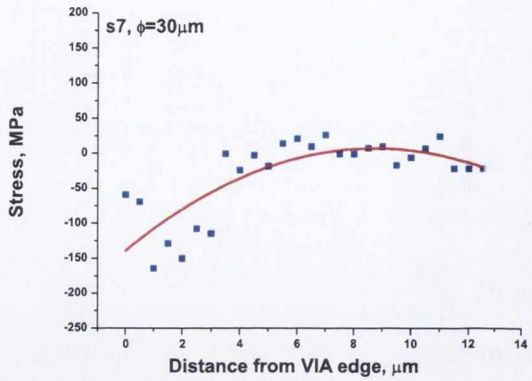

(b) Sample 7

Figure 4.22 – The dependence of the stress on the position for samples s6 and s7.

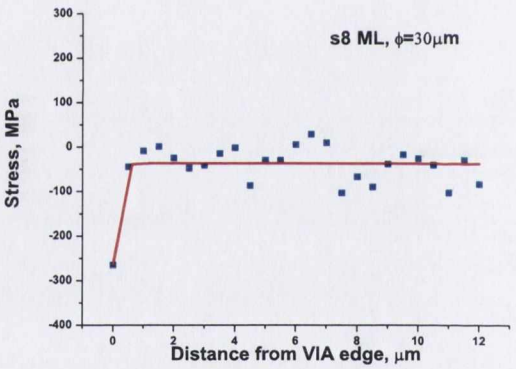

(a) Sample 8

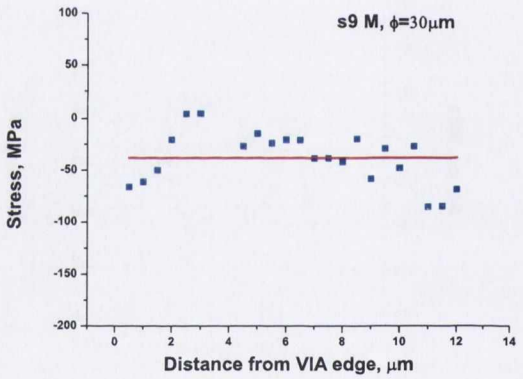

(b) Sample 9

Figure 4.23 – The dependence of the stress on the position for samples s8 and s9.

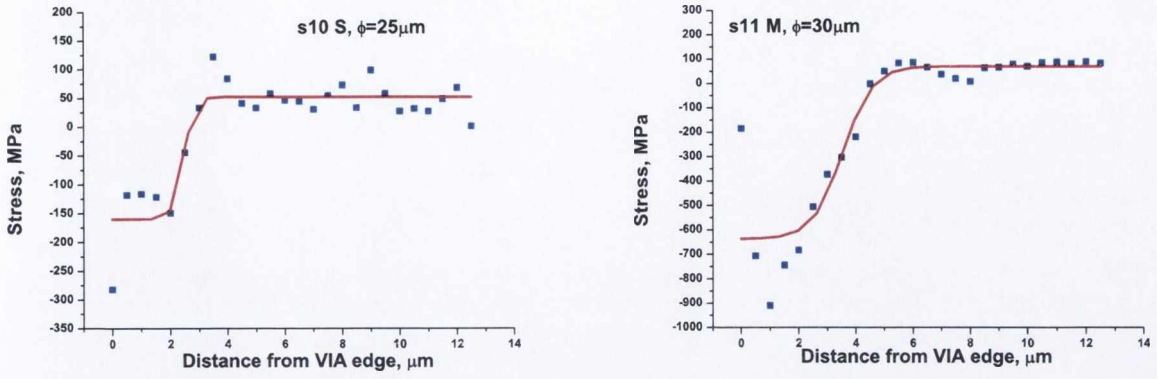

(a) Sample 10

(b) Sample 11

Figure 4.24 – The dependence of the stress on the position for samples s10 and s11.

It can be seen from the above figures that the stress decreases significantly at a distance of 2-6 μm from the via edge for most samples. Compressive stress appears to be more prevalent. No significant differences were seen between the different drilling techniques in the stress distribution.

Laser Dicing

Conventionally, wafers are diced into chips using a rotating blade. Water is used to cool the blade and to remove debris, this process is not completely reliable and significant debris can remain, see Fig. 4.25. Sensitive structures must be protected both from the water and the moving debris. This can significantly limit design freedom in particular for microelectrical mechanical systems (MEMS) which are often very fragile. Laser dicing hopes to reduce these problems.

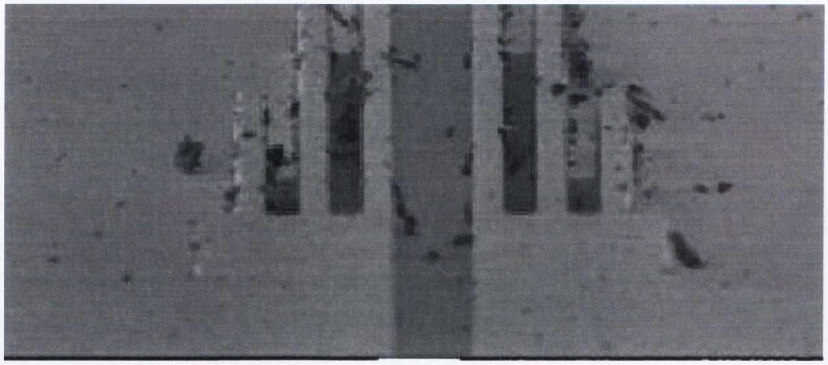

Figure 4.25 – Debris resulting from mechanical dicing [47].

Similarly to the TSVs discussed above the laser diced wafers also show a significant reduction in stress away from the edges. Figure 4.26 shows a laser diced Silicon wafer.

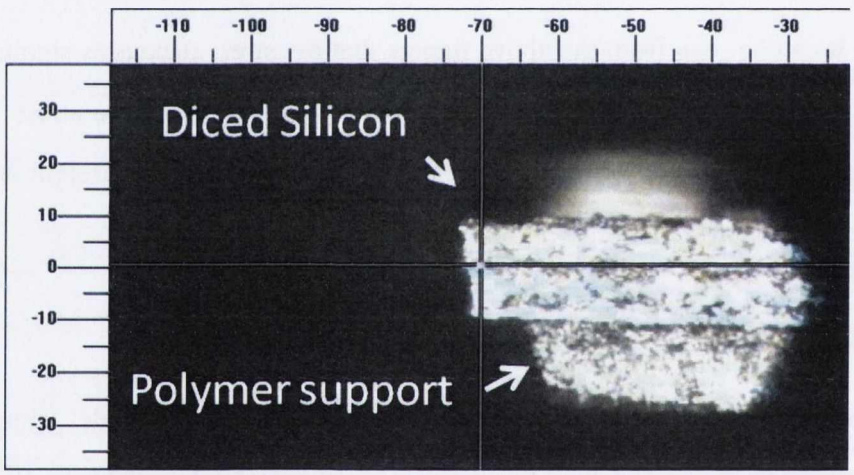

Figure 4.26 – Cross section of a laser diced wafer. Raman measurements were taken horizontally from the position marked with the crosshairs.

After Raman measurements had been conducted the stress was calculated as shown in Fig. 4.28 and Fig. 4.29.

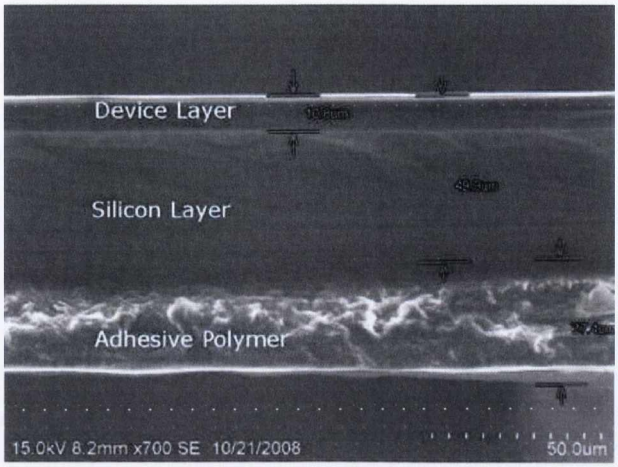

Figure 4.27 – SEM cross section of diced wafer showing each layer.

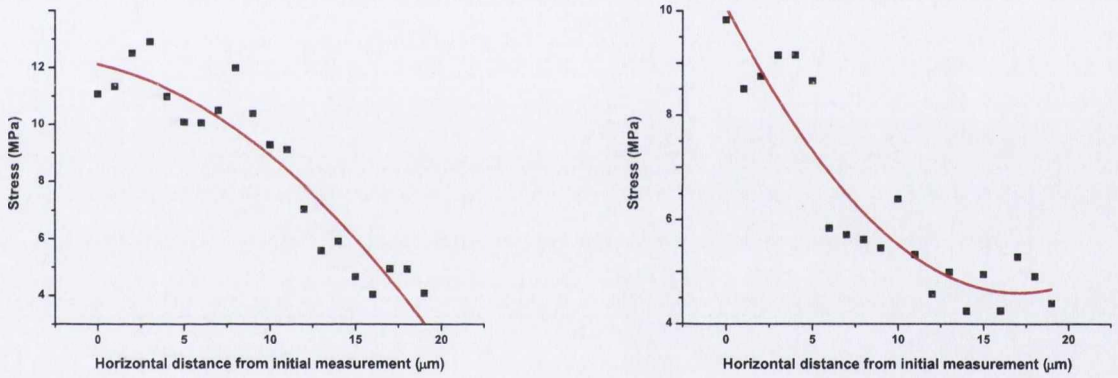

(a) Centre

(b) Centre

Figure 4.28 – The horizontal distribution of stress in the diced wafer. The depth of these measurements is shown by the crosshairs in Fig. 4.26

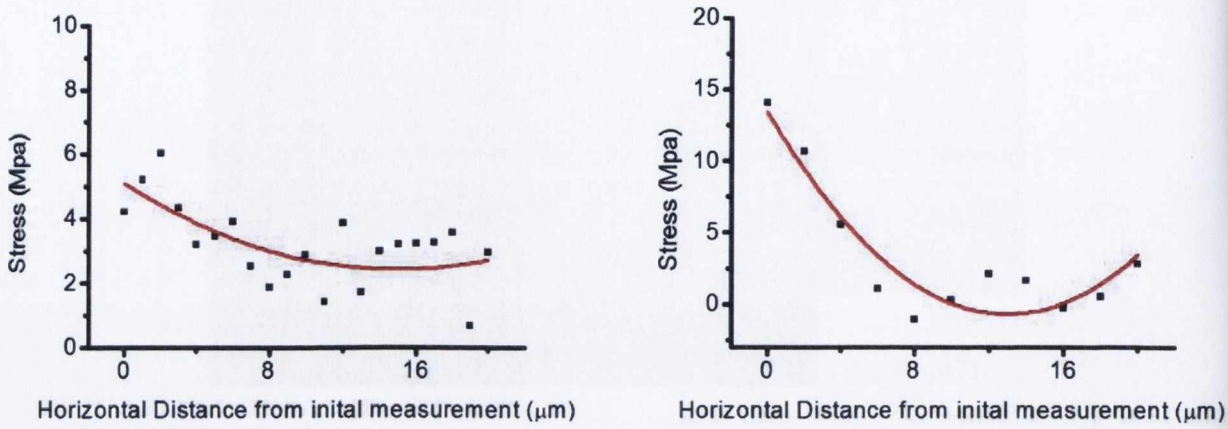

(a) Top

(b) Bottom

Figure 4.29 – Stress reduces from a peak near the edge of the laser diced wafer. a) was measured near the top of the wafer and b) near the bottom as shown in Fig. 4.26

4.4 Results Discussion

The initial single spot measurements confirmed that in the vast majority of samples the stresses found was below 200MPa in comparison to the much larger stress of 1.4 GPa found recently in a study of vias fabricated using a different laser drilling process [48]. The stress values above 200MPa were always isolated occurrences and similar vias with identical processing did not necessarily show stress values in the same regions. Irreproducible results such as these could possibly have been caused by surface damage due to Silicon spluttering and melt during the ablation process or experimental error due to obscured Silicon from environmental contamination. The data from the spot checks did however yield information about the location and type of stress, compressive stress in particular was very prevalent in the upper half of the vias sidewalls. The top left hand mouth of the vias were often sloped outwards (e.g. see Figs. 4.11 and 4.12) and a corresponding higher stress on the left hand sidewall when compared to the right can be seen, indicating that perhaps the laser spot is not perfectly spherical or vertical and overly ablates the left hand side causing a stress build up. No strong correlation between stress levels surrounding the via and via depth could be

found. Stress at the bottom of the via varied, although some samples (Figs. 4.16 and 4.17) did show strong tensile stress unlike the sidewalls where compressive stress is normally seen. Although the magnitude of stress either tensile or compressive is quite small except in sample s10, s11 and s2. Samples s10 and s2 have the smallest diameters indicating a possible correlation. Samples s6, s9 and s11 all used multistep ablation and in each sample semi spherical defects can be seen in the sidewalls of the vias possibly caused by inaccurate laser positioning on subsequent cycles. No major differences were seen in stress measurements between multistep and singlestep drilling in samples s6 and s9. Sample s11 however had the highest levels of compressive stress of any sample near the via mouth. The results obtained during the line-mapping experiments to determine the extent of the heat affected zone show a significant reduction of stress a distance of 2-4 μm from the edge of the vias. This is demonstrated as an example in Figs. 4.19 and 4.20(a) for sample s2 in this section. It can also be seen that in most of the cases stress calculated from the Raman shift using Eqn. 4.5 is varied in the range from -100 to 50 MPa a distance 2-4 μm up to 10 μm from the via edge. This stress is relatively small and could be due to the process of grinding and rough polishing during the samples cross-section preparation. The results obtained are of far less magnitude than the data received for stress value and heat affected zone propagation obtained in [49, 50], where significant stress and large heat affected zone area were found.

Amorphous Silicon was not detected at the edge of the vias, fabricated by XSiL. This is contrary to recent results from [50] and [48] where a different drilling process for via fabrication was used. This difference can be clearly seen by comparing Fig. 4.30 and Fig. 4.31 where the Raman spectra obtained in this work and by Amer et. al [48] respectively are shown.

The Raman spectra obtained for all samples could be fitted using a single Lorentzian curve unlike the spectra in Fig. 4.31 where three Lorentzian functions are required to fit the obtained amorphous Silicon spectrum due a further peaks at 480 cm^{-1} and below caused by the amorphous Silicon [50].

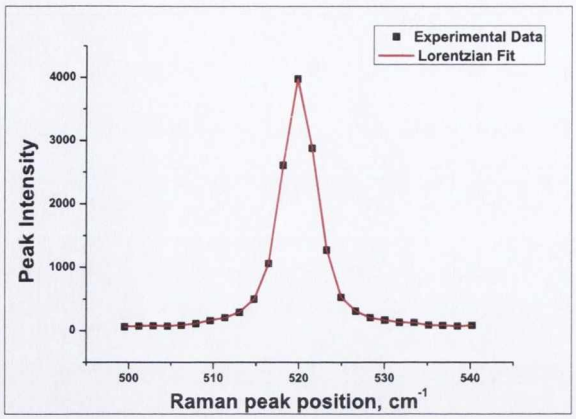

Figure 4.30 – Raman spectrum from a measurement taken near a Silicon via and fitted with a Lorentzian function.

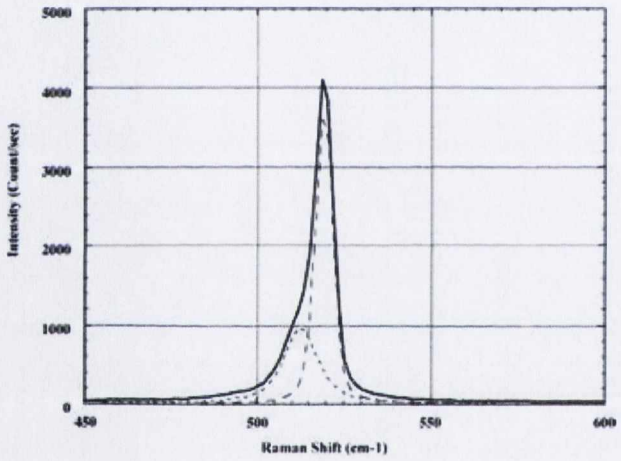

Figure 4.31 – Typical Raman spectrum of via structure with the presence of amorphous Silicon at the edge. Due to asymmetry from the low frequency side this spectrum required three Lorentzian functions for a good curve fitting [48].

4.5 Conclusion

The results showing the extent of the heat affected zone compares very favourably with results obtained in [48, 50] where a significant induced stress of up to 1.4 GPa and amorphization in single crystal Silicon (ranged up to ~20%) were found using a UV laser and nanosecond pulse duration. The stress values above 200MPa were always isolated occurrences possibly resulting from sample damage. Compressive stress in particular was very prevalent in the upper half of the vias sidewalls. No strong correlation between stress levels

surrounding the via and via depth could be found. The results obtained during the line-mapping experiments to determine the extent of the heat affected zone show a significant reduction of stress a distance of 2-4 μm from the edge of the vias. Amorphous Silicon was not detected at the edge of the vias, fabricated by XSiL. This is contrary to recent results from [50] and [48] where a different drilling process for via fabrication was used. Based on these results the technique developed by XSiL had significant advantages over existing through Silicon vias formed by laser ablation. For the laser dicing samples the stress in the heat affected zone declined away from the sidewall.

Chapter 5

Microcrystalline Silicon

5.1 Introduction

Photovoltaics have developed enormous economic importance over the last few decades and increasingly are seen as a viable alternative to fossil fuels. Over the years there have been many attempts to improve on existing solar cell technology. Not only in the solar efficiency but also incorporating other important factors such as the ease of fabrication and reducing costs. Silicon due to its cost, manufacturing base and almost inexhaustible supplies is still the dominant technology today.

Solar cells operate on the principle of direct and/or indirect transition whereby an incident photon excites an electron to an excited state. Figs. 3.2a and 3.2b show the incident energy in electronvolts (eV) of photons of various wavelengths. Micro-crystalline Silicon has been proposed as a solar cell material that combines the low cost of amorphous Silicon with the stability of monocrystalline Silicon.

Since the optical and electrical properties of micro-crystalline Silicon depend on the fraction of crystalline material, the crystallite size, and the grain boundaries an accurate determination of the crystallinity fraction for micro-crystalline Silicon is of primary importance. Raman spectroscopy can be used to determine the crystallinity fraction but there are several shortcomings with the existing techniques that have been examined and attempts made to

improve them.

5.2 The Advantages of Microcrystalline and Amorphous Silicon

Crystalline Silicon is expensive, it also needs to be quite thick due to its indirect band gap. Several alternative materials that are strong light absorbers and inexpensive have been examined. The most common materials are amorphous Silicon (*a*-Si, still Silicon, but in a different form), or the polycrystalline materials: Cadmium Telluride (CdTe) and Copper Indium (Gallium) Diselenide (CIS or CIGS).

Each of these three is amenable to large area deposition (on to substrates of $\sim$1 metre dimensions) allowing high volume manufacturing. The thin film semiconductor layers are deposited on to either coated glass or stainless steel sheet.

Several key properties are required for the existence of a solar cell. Defined energy bands and the ability to change the intrinsic Fermi level of the Silicon through doping. It was discovered in 1972 that plasma-deposited amorphous matrices can be made with a low density of states in the semiconductor band gap [51] and therefore had a band structure. Doping was also achieved [52, 53] in amorphous Silicon. This allows the construction of pn-junctions and solar cells out of amorphous Silicon. Plasma deposited 'amorphous' matrices are in reality 'non-crystalline' in which the chemical bonding is nearly unchanged from crystals but small disorderly variation in the angles between the bonds eliminates regular lattice spacing. There are also numerous defects in which case Silicon atoms do not bond to four other Silicon atoms but only bond to three leaving a 'dangling bond'. These dangling bonds act as recombination centers that severely reduce the carrier lifetime and do not allow doping. However it was discovered [54] that the introduction of Hydrogen, passivated these extra bonds eliminating the dangling bonds. As Silane (SiH_4) is used in plasma deposition the amorphous Silicon had a significant percentage of Hydrogen atoms. This is called "hydrogenated amorphous Silicon" (*a*-Si:H) however it suffers from the "Staebler-Wronski

Effect"[55]. This results in a significant decrease in efficiency of a-Si:H solar cells after being exposed to sunlight, eventually they stabilise after approximately 1000 hours due to an increase in defect density with light soaking as the Hydrogen atoms gain sufficient energy to disassociate with the Silicon. A solution to this problem is to use "microcrystalline Silicon" (also known as nano-crystalline Silicon).

Hydrogenated Microcrystalline Silicon, consists of small crystalline grains embedded in an amorphous matrix. It has a higher doping efficiency requiring less Hydrogen than a-Si:H so is resistant to the Staebler-Wronki effect and has increased absorption efficiency at longer wavelengths than a-Si:H. It has strong potential in multijunction solar cells. Multijuction cells consist of layers of a-:Si:H and μc-Si:H sandwiched together using their different absorption characteristics to capture as much of the incident light spectrum as possible. Other composite materials or alloys of Silicon can also be used to increase absorption efficiency and increase the number of layers.

5.3 Raman Spectra of Microcrystalline Silicon

The Raman spectra of microcrystalline Silicon is composed of two components. A component from the amorphous matrices and also a Raman spectra from the embedded microcrystalline features as shown in Fig. 5.1.

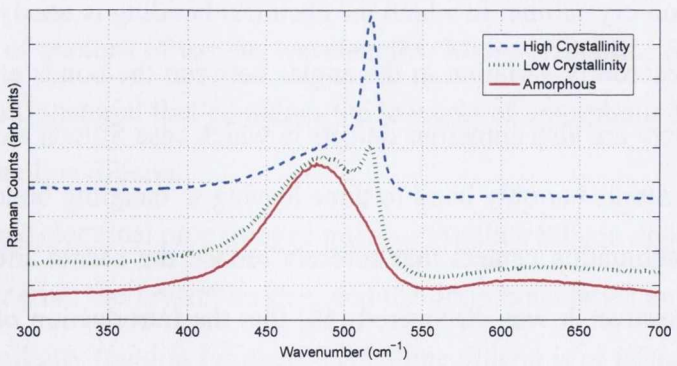

Figure 5.1 – Evolution of Raman spectra from a fully amorphous state to a largely crystalline state.

Since the optical and electrical properties of micro-crystalline Silicon depend on the fraction of crystalline material, the crystallite size, and the grain boundaries an accurate determination of the crystallinity fraction for micro-crystalline Silicon is of primary importance.

High-Resolution Transmission Electron Microscopy (HRTEM) [56], X-Ray Diffraction (XRD) [57] and Raman spectroscopy [58] are the primary experimental techniques currently employed to determine the crystal structure of micro-crystalline Silicon. Raman spectroscopy, does not require elaborate sample preparation and measurements can be conducted quickly. In contrast to the special preparation of thin-film samples using other techniques for example TEM and XRD. XRD has no dependence on the depth of penetration as the X-Rays pass through the entire sample and a long measurement time. The shape and the position of the Raman bands is strongly influenced by both the size and the shape of the Si crystal grains and as a result of quantum effects [59], care must be taken when interpreting spectra. The accuracy is highly dependent on spectral analysis in particular on the spectral fitting as the amorphous and microcrystalline bands are composite and not well defined. Several methods have been proposed to accurately determine the crystallinity fraction, including deconvolution into multiple constituent fitting profiles [60] and amorphous subtraction [58].

The crystallinity fraction is normally determined as the ratio of the TO band of crystalline Silicon to the TO band of amorphous Silicon. As these bands overlap several techniques have been developed to deconvolute the spectra into its separate components. Several peak fitting approaches have been proposed using two and three peak fitting. Two peak fitting assigns one Gaussian peak to the amorphous component and a second Lorentzian peak to the crystalline component of the micro-crystalline spectra. A Lorentzian peak will strongly bias the contribution from the zone centre phonon and does not capture the full asymmetric microcrystalline spectra which overlaps with the amorphous spectra. Furthermore, the amorphous component is not a single Gaussian function but rather a combination of optical and acoustic phonon bands, shown in Fig. 2.5, therefore the Gaussian function does not adequately fit the spectra without significant error. Adding a further peak, intermediate between the amorphous peak and the crystalline peak as shown in Fig. 5.2b, significantly reduces the

residual error [61] however there is little evidence of a physical explanation to account for this additional peak.

If three peak fitting is used the crystallinity fraction is then determined from Eqn. (5.1) where Ia, Im and Ic are the amorphous, intermediate and crystalline integrated intensities, γ is a wavelength dependent scaling factor taken to be on average 0.88 [58].

$$Xc = \frac{Ic + Im}{Ia + Im + \gamma Ic} \tag{5.1}$$

It is extremely difficult to reliably and repeatably fit the amorphous and intermediate peaks. Errors are introduced due to the absence of a third defined peak, as a result the position and width of the peaks can vary significantly depending on the width of the selected region and the local minimum the fitting algorithm determines. As a result several local minimums are possible that lead to very different results. In addition, factor analysis has indicated that 98% of the spectrum can be accounted for using only two spectral components [62]. Therefore it must be assumed that the spectrum has two components that are not precisely Lorentzian or Gaussian shaped.

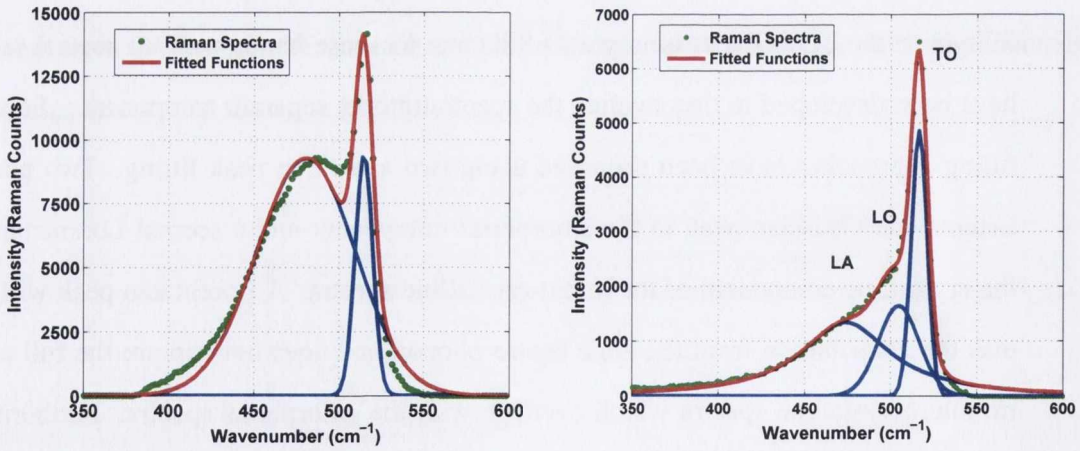

(a) Two peak Fitting

(b) Three peak fitting

Figure 5.2 – Different approaches to fitting the spectra of microcrystalline Silicon.

Smit et al. [58] proposed an alternative technique in which the shape of the amorphous

component was considered constant across samples of varying crystallinity and the change in the spectra was primarily due to changes in the crystalline peak. All peaks surrounding the first order scattering between approximately 380 and 440 cm^{-1} are assigned to the amorphous spectrum. A 'least squares fit' was then applied in order to scale a reference amorphous spectra so that it could than be subtracted from the sample spectra. The remaining spectra could be assigned to the microcrystalline component. The crystalline fraction was then found as

$$Xc = \frac{Ic}{Ia + \gamma Ic} \tag{5.2}$$

where Ic is the integrated intensity of the spectra remaining after the amorphous component subtraction this corresponds to the microcrystalline component. Ia is the TO component of the amorphous spectra, the TO component can be found approximately by fitting three Gaussian curves as shown in Fig 5.3.

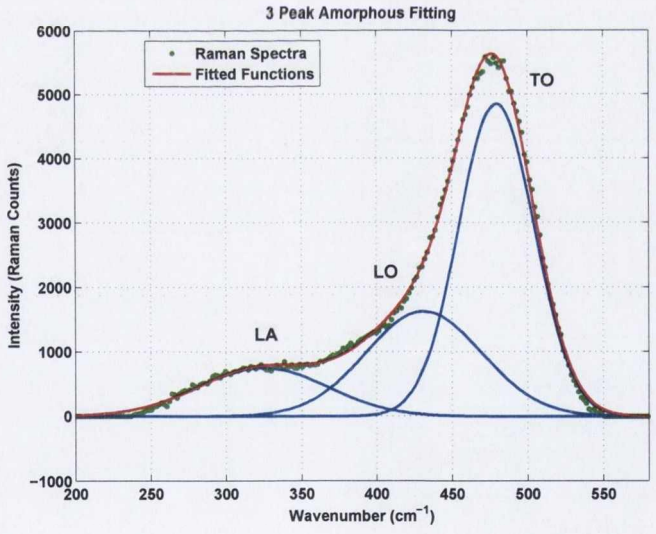

Figure 5.3 – Deconvolution of amorphous component of Raman spectra of microcrystalline Silicon using three Gaussian peaks.

This was significantly more reliable than the two and three peak fitting approaches. However this technique suffers from several problems. The crystalline component does not consist solely of the first order Raman peak at approximately 520 cm^{-1} but also includes second

order peaks of Raman scattering including overtone, combination and acoustic phonon peaks at wavenumbers above and below the central TO peak at 520 cm^{-1}. The influence of these second order peaks is more pronounced for longer wavelengths of excitation such as 633nm due to its larger penetration depth, as shown in Table 3.1 and the associated increase in the scattered light recovered.

As these peaks result from the crystalline phase they are most pronounced when the sample has a large crystalline component. The second order peaks overlap the regions assigned purely to the amorphous spectra and used to calculate the scaling factor in [58]. Therefore the correct scaling factor cannot be found using the least fit analysis described in [58] due to this overlap and leading to errors as shown in Fig. 5.4.

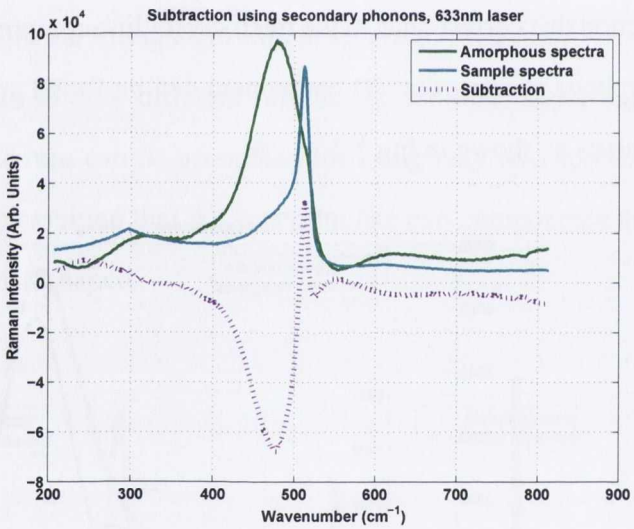

Figure 5.4 – Spectra subtraction showing the effect of second order phonons. The scaling factor was calculated using the peaks surrounding the amorphous peak as described in [58]. The magnitude of the error is proportional to the crystallinity fraction

Attempts were made to improve the reliability of the latter approach by reducing the influence of the secondary phonons. This is achieved in two ways.

1) Polarisation of scattered light is used to remove the influence of the secondary phonons which result primarily from the Γ_1 representation.

2) Least squares regression, a form of chemometric analysis, is used to determine the correct scaling factor of the amorphous phonons without influence from the second order

phonons.

The different fitting procedures had to be implemented using MATLAB in order to determine the crystallinity fraction. The custom MATLAB code written is included in the appendix.

5.4 Sample Preparation

Phive Plasma Technologies, a campus company based in DCU was our partner for this work and provided the samples. Unfortunately now in receivership they had developed a technique to improve hydrogenated Silicon deposited by Plasma Enhanced Chemical Vapour Deposition (PECVD) using scalable segmented electrode topography. PECVD is well known for its advantageous properties in the deposition of amorphous Silicon for solar cells. However, Silicon can also be deposited in the micro-crystalline phase, which has the advantage of a lower band gap allowing for the absorption of grey light. When used in tandem cells a greater efficiency than those with a single amorphous junction is achieved. Large area deposition of micro-crystalline Silicon is generally associated with low silane (SiH_4) concentrations and low deposition rates. It has been shown that deposition rate increases with increasing RF excitation frequency with the disadvantage of wavelength effects [63]. By using a scalable, segmented electrode topology large area depositions of micro-crystalline Silicon can be deposited at high deposition rates [64]. Depositions of micro-crystalline Silicon at rates of up to 15A/s have been achieved with SiH_4 concentrations of 20% [64].

A selection of micro-crystalline samples grown on glass substrates having varying crystallinity fractions were used as a sample set. A set of samples covering the complete crystallinity spectrum were manufactured by adjusting the Silane and Hydrogen ratio.

5.5 Raman Measurements

Raman spectra were registered in a backscattering geometry from the samples using a RENISHAW 1000 micro-Raman system equipped with a CCD camera, a Leica microscope and

Table 5.1 – Set of samples and their production parameters.

Sample	SiH_4	H_2	Pressure	Time	Temp.	Pwr. Set Pt.	Exposure	SiH_4 conc.
100121-02	90	424	1000	500	180	2400	750	17.5%
100121-03	90	360	1000	500	180	2400	750	20.0%
100121-04	90	310	1000	500	180	2400	750	22.5%
100122-01	108	432	1000	420	180	2400	756	20.0%
100122-03	126	504	1000	360	180	2400	756	20.0%
100122-04	144	576	1000	325	180	2400	780	20.0%
100123-02	126	504	1000	360	180	2800	756	20.0%
100123-03	126	504	1000	380	180	3200	798	20.0%
100123-04	144	576	1000	315	180	2800	756	20.0%
100125-01	144	576	1000	315	180	3200	756	20.0%
100128-02	150	720	1000	180	180	2800	450	17.2%

Table 5.2 – Second set of samples and their production parameters.

Sample	SiH_4	H_2	Pressure	Time	Temp.	Pwr. Set Pt.	Exposure	SiH_4 conc.
091110-02	53	537	1000	1000	180	1800	750	9.0%
091111-01-7d	56	534	1000	1440	180	1800	750	9.5%
091112-01	59	531	1000	930	180	1800	750	10.0%
091112-02-7c	53	537	1000	948	180	1800	750	9.0%
091112-02-7d	59	531	1000	930	180	1800	750	10.0%
100121-03-2b	90	424	1000	500	180	2400	750	17.5%
100121-03-2b	90	360	1000	500	180	2400	750	20.0%
100121-04-2b	90	310	1000	500	180	2400	750	22.5%

a 50x objective. A line grating of 1800 lines/mm was used for all measurements, providing a spectral resolution of approximately $1cm^{-1}$. The sample set was measured using Ar^+ and HeNe lasers with 514nm and 633nm wavelengths. The use of different excitation wavelengths allows the Raman signal to be collected at different depths of penetration. However, the exact depth of penetration was difficult to determine as the samples do not consist of homogeneous material but rather varying concentrations of amorphous and crystalline Silicon grains. Crystalline Silicon has a larger depth of penetration (d_p) in comparison to amorphous Silicon, as a result amorphous Silicon below the nucleations sites of the conical crystalline grains can also influence the spectra [65] adding additional difficulties when determining the d_p accurately. The depth of penetration for crystalline Silicon is shown in Table 3.1.

5.5.1 Attenuation of second order phonons using polarisation filters

The method proposed by Smit et al., [58], suffers as the secondary phonons of crystalline Silicon overlap the amorphous bands. In order to find the correct multiplier or scaling fac-

tor (the amount by which the Silicon spectra must be scaled) for subtraction, the crystalline secondary phonon peaks must be suppressed or removed. The incident and scattered photons belong to the zone-centre ($\vec{k} = 0$) in the case of first order scattering they are single phonons. However in the case of optical second order phonons they correlate with multi-phonon emissions that have a product representation belonging to the zone centre representation but whose constituent (equal and opposite) phonons do not. The three representations to which the Raman tensor of fully crystalline Silicon belongs in this group are Γ_1, Γ_{12} and Γ_{25}.

For single crystal Silicon it was shown [15] that if the incident light is parallel to the crystalline (110) or (001) planes and the scattered light is perpendicularly polarised to the incident light the selection rules limit the scattered spectra to the Γ_{25}, representation which has very little second order scattering. The vast majority of the second-order scattering results from the Γ_1 representation [15] and it is strongly attenuated, as shown in Fig. 5.5. As this phenomenon was shown for both planes, it prompted the possibility that this technique could be used to remove second order scattering from micro-crystalline Silicon with grains of differing crystalline orientation.

If the micro-crystalline Silicon has a very high crystallinity fraction, a much reduced second order spectrum was still visible despite attenuating polarisation filters. In particular in the region at 300cm^{-1} due to a strong acoustical phonon peak from the monocrystalline Silicon. Unfortunately this overlaps with the amorphous spectral component used to calculate the scaling factor. However, the amorphous peak at 600cm^{-1} does not have this problem as shown in Fig. 5.6. Therefore for samples with a very high crystallinity, such as that shown in Fig. 5.4, it becomes difficult to determine the crystallinity fraction. If polarisers are used to attenuate the second order and acoustical peaks their influence is removed and a scaling factor can be obtained. The highest accuracy using polarisers was obtained by solely fitting the amorphous spectral region at 600cm^{-1} from a fully amorphous sample to obtain a scaling factor. The amorphous spectra is then scaled by this factor and subtracted from the microcrystalline spectra. This technique can also be applied using non-polarised light to im-

prove the resolution of the Smit process. However as the amorphous spectra in this region is quite weak accumulation times are long especially as the polarisation attenuates the Raman scattering and this is not appropriate for rapid mapping. Table 5.3 shows the results of the different fitting techniques discussed above. It can be seen from the table that the two peak fitting is normally significantly smaller than the other techniques. The fitting using the 630 cm^{-1} peak shows a higher Xc value in general than the other columns as it is less effected by the second order effects which tend to promote low crystallinity values.

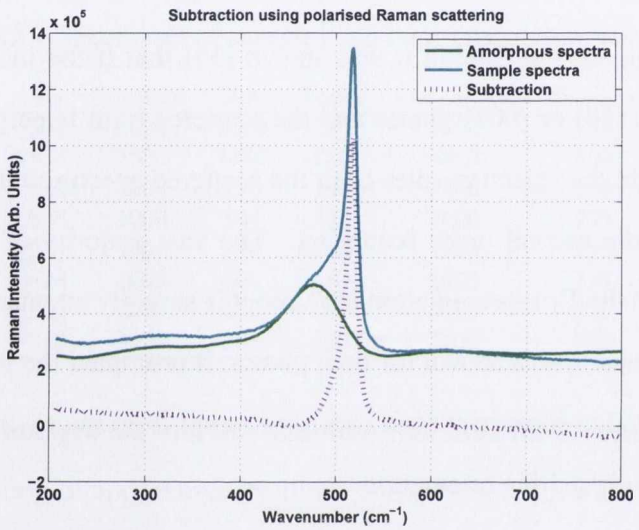

Figure 5.5 – Effect of polarised Raman measurements on amorphous subtraction using only secondary peak situated at 600 cm^{-1}.

5.5.2 Chemometric Analysis

In order to improve upon existing techniques a statistical approach was developed. This approach has several advantages over the existing techniques as it takes into account the secondary phonons and does not rely on the phonon peaks of amorphous Silicon therefore it requires less accumulation time. Several approaches were examined such as Classical Least Squares (CLS), Principal Component Analysis (PCA) and Multivariate Curve Resolution (MCR). However eventually the most accurate technique to determine the scaling factor was found to be simple regression analysis in particular Classical Least Squares. The CLS

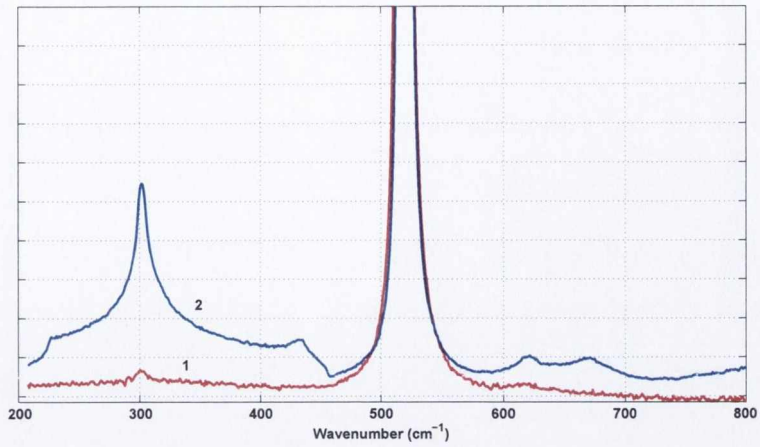

Figure 5.6 – Removal of second order peaks surrounding the first order peak at 520cm^{-1} from single crystal Silicon wafer. 1) Spectrum using polarisers 2) Spectrum without polarisers. The spectrum have been scaled using the intensity of the first order peak. The (001) plane is parallel the incident light.

Table 5.3 – Xc values calculated using two peak, three peak and Smit analysis .

Sample	Polarisation	Two peak	Three peak	Smit using 630 cm^{-1} peak	Smit using both peaks
091110-02	N	0.39	0.56	0.70	0.53
091110-02	Y	0.41	0.57	0.71	0.70
091111-01-7D	N	0.41	0.58	0.67	0.40
091111-01-7D	Y	0.42	0.59	0.68	0.67
091112-01	N	0.20	0.41	0.34	0.26
091112-01	Y	0.20	0.40	0.28	0.32
091112-02-7C	N	0.34	0.50	0.58	0.44
091112-02-7C	Y	0.35	0.52	0.63	0.60
091112-02-7D	N	0.28	0.46	0.60	0.31
091112-02-7D	Y	0.27	0.45	0.53	0.48
100121-02-2B	N	0.40	0.55	0.79	0.45
100121-02-2B	Y	0.44	0.59	0.72	0.68
100121-03-2B	N	0.43	0.58	0.65	0.32
100121-03-2B	Y	0.47	0.60	0.46	0.46
100121-04-2B	N	0.22	0.43	0.57	0.19
100121-04-2B	Y	0.21	0.43	0.45	0.44

model assumes that measurements are the weighted sum of linearly independent signals. In spectroscopy, the CLS model assumes that measured spectra are the sum of pure component spectra weighted by their respective concentration. Thus, the model is:

$$\mathbf{x} = \mathbf{pS} \tag{5.3}$$

where **x** is the measured spectra, **S** is the matrix of pure component or basis spectra and **p** is the vector containing the concentrations of the component spectra or loadings. Generally, given the vector of measurements, **x**, one would like to know **p**, the degree to which each component contributes to the overall measurement.

A fully amorphous spectra and a spectra from a single crystal Silicon wafer measured using the same experimental parameters as the micro-crystalline samples were used as the basis vectors for the CLS analysis (the **S** matrix). The resultant loadings will contain a least fit analysis with residuals as shown in Fig. 5.7.

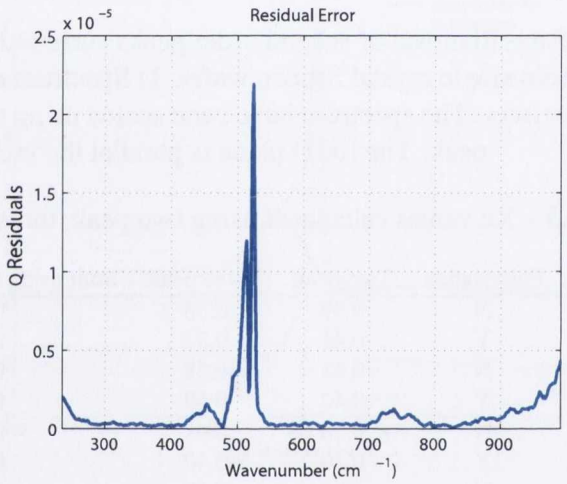

Figure 5.7 – Residuals (fitting error) showing that the majority of the fitting error is due to the widening of the crystalline band.

Although these fitting will contain significant error, it is primarily due to the asymmetric broadening of the micro-crystalline peak, due the relaxation of the momentum conservation rule, see Fig. 5.8. The scaling factor of the amorphous component should be correct. The scaled amorphous peak can then be subtracted from the micro-crystalline spectra and the crystallinity fraction calculated as described in [58].

The Eigenvector PLS Toolbox [66] was used for CLS fitting. Initially the dataset was preprocessed using SavGol smoothing to smooth, second order polynomial baseline fitting to remove the baseline and area normalisation to normalise the spectra. The scaling factor for each individual micro-crystalline spectra is found in the loading matrix (**p**) consisting of

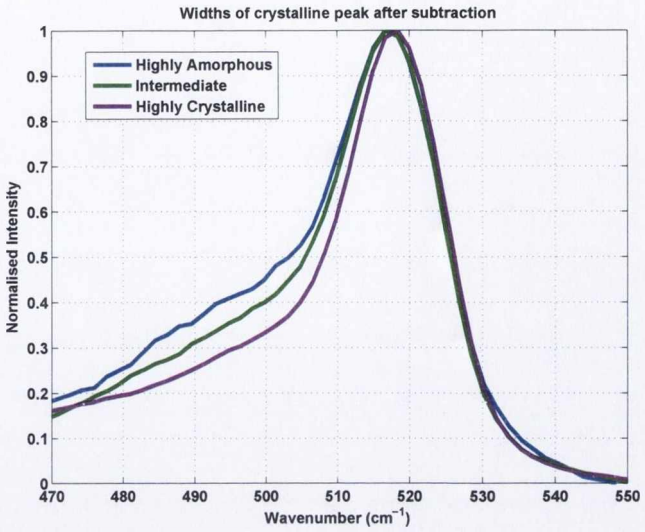

Figure 5.8 – Raman spectra of the Si-Si peak of micro-crystalline Silicon indicating the increase in the linewidth depending on the crystallinity.

two factors corresponding to the amorphous and crystalline components. The amorphous factor can then be used as the scaling factor in the technique described in [58]. Tables 5.4 displays the results of this approach.

Table 5.4 – Xc values calculated using CLS for 633nm lasers, all from unpolarised samples with low crystallinity.

Sample	CLS	Smit	Two peak
100121-02	0.30	0.25	0.26
100121-03	0.36	0.48	0.37
100121-04	0.25	0.35	0.26
100122-01	0.15	0.24	0.18
100122-03	0.02	0.08	0.07
100122-04	0.09	0.14	0.10
100123-02	0.20	0.28	0.24
100123-03	0.20	0.31	0.23
100123-04	0.04	0.12	0.09
100125-01	0.12	0.18	0.13
100128-02	0.18	0.27	0.18

Further Chemometric Techniques

Blind source separation chemometric algorithms do not require that the spectral shape be known in advance and aim to deconvolute the sample spectrum into it constituent components. Several techniques were examined namely Principal Component Analysis and Mul-

tivariate Curve Regression with different constraints. The aim of these algorithms is to attempt automated separation of microcrstalline Si into it's independent additive components consisting of an amorphous and crystalline component. If successful decomposition can be preformed, the crystalline fraction can be calculated based on the relative intensities of these components. These techniques are powerful tools frequently used to determine component spectra but due to the width dependence of the crystalline peak on crystallinity and the large area of overlap they were not sufficiently accurate to be of use in the microcrystalline samples under investigation.

Principal Component Analysis

Principal Component Analysis (PCA) is one of the most common and frequently used chemometric techniques. It separates a dataset into a number of *factors* that describe major trends in the data. If $\mathbf{X}$ is a data matrix with m rows and n columns with each variable being a wavenumber reading from the spectrometer and each row the spectra from a sample. PCA decomposes $\mathbf{X}$ as

$$\mathbf{X} = \mathbf{t}_1\mathbf{p}_1^T + \mathbf{t}_2\mathbf{p}_2^T + \cdots + \mathbf{t}_k\mathbf{p}_k^T + \ldots \mathbf{t}_r\mathbf{p}_r^T = \mathbf{T}P^T \tag{5.4}$$

The $\mathbf{t}_i$ vectors are called *scores* and the $\mathbf{p}_i$ vectors are called *loadings* and r is the rank of the matrix $\mathbf{X}$. A complete expansion up to r completely describes the data. In the case of microcrystalline Silicon this is simplified into two loading vectors one describing the amorphous and the other the crystalline component. All the remaining score, loading pairs are combined into an error matrix $\mathbf{E}$ so that

$$\mathbf{X} = \mathbf{t}_1 p_1^T + \mathbf{t}_2\mathbf{p}_2^T + \mathbf{E} \tag{5.5}$$

One score vector would then quantify the crystalline loading in each sample and the other would quantify the amorphous loading in each sample. $r = 2$ in this case. PCA uses an eigenvector decomposition of the covariance matrix

$$cov(\mathbf{X}) = \frac{\mathbf{X}^T X}{m-1} \tag{5.6}$$

This means that the loadings and scores are arranged in descending order of variance. Therefore the first loading, score pair will capture the maximum variance in the data. This is very useful for finding hidden factors and simplifying data into a small number of factors but suffers as the components frequently consist of negative and positive contributions which is not possible for spectroscopic data. This is due to the rotational ambiguity inherent to the PCA algorithm, as the equation

$$\mathbf{X} = \mathbf{T}\mathbf{P}^T + \mathbf{E} = \mathbf{T}\mathbf{R}\mathbf{R}^{-1}\mathbf{P}^T + \mathbf{E} \tag{5.7}$$

has an infinite number of possible solutions for the arbitrary transformation matrix **R**. However, factor analysis techniques such as PCA can be used to indicate the number of components responsible for the spectra. In the case of microcrystalline Silicon factor analysis has indicated that 98% of the spectrum can be accounted for using only two spectral components [62] and this is reproduced in Fig. 5.10 for the sample set shown in Fig. 5.9.

Multivariate Curve Resolution

This class of methods is termed source separation or multivariate curve resolution (MCR). It requires the introduction of *constraints* on the shape of the loadings. Application of MCR requires a number of spectra recorded at different stages of structural evolution in the case of micro crystalline Silicon this requires samples from the complete spectrum of different crystalline fractions. The MCR equation is presented as follows

$$\mathbf{X} = \mathbf{C}'\mathbf{S} + \mathbf{E} = \mathbf{X}_{\text{est}} + \mathbf{E} \tag{5.8}$$

where **C** is the contribution matrix, **S** is the matrix of pure component spectra, and **E** is error (random or systematic). One of the most important constraints when dealing with Raman spectra is that of *non-negativity*, that is both the spectra matrix, **S** and the contribution

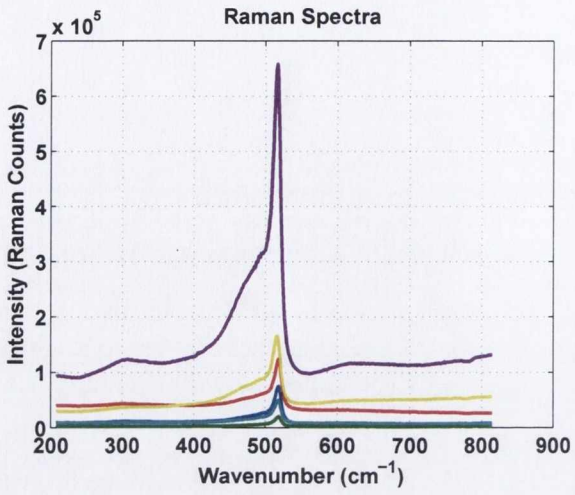

(a) Set 1

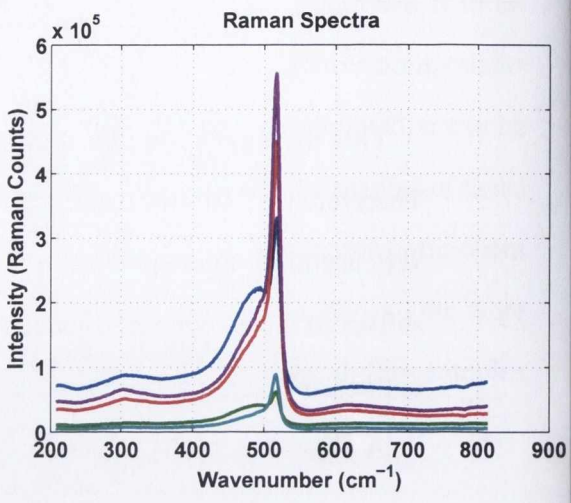

(b) Set 2

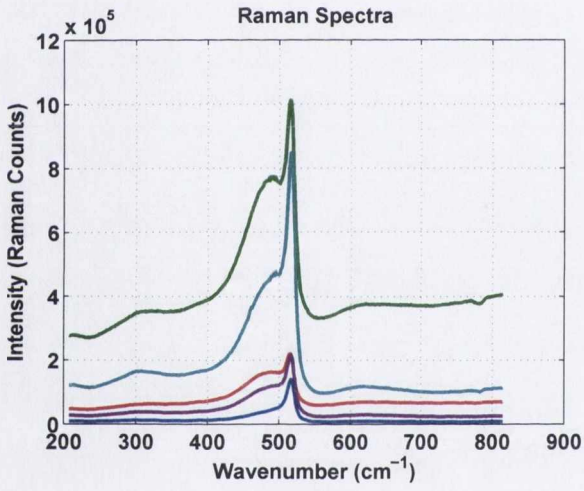

(c) Set 3

Figure 5.9 – Set of sample spectra used for PCA analysis, covering a broad range of crystallinity these three sets were combined into a single dataset.

matrix, **C** are non-negative. This constraint is achieved through the use of the Alternating Least Squares (ALS) algorithm. This algorithm iterates between a prediction of **S** and **C**, during each iteration a new estimate of the spectra matrix **S** and of the concentration matrix **C** is obtained. This is achieved by iterating between the following two equations

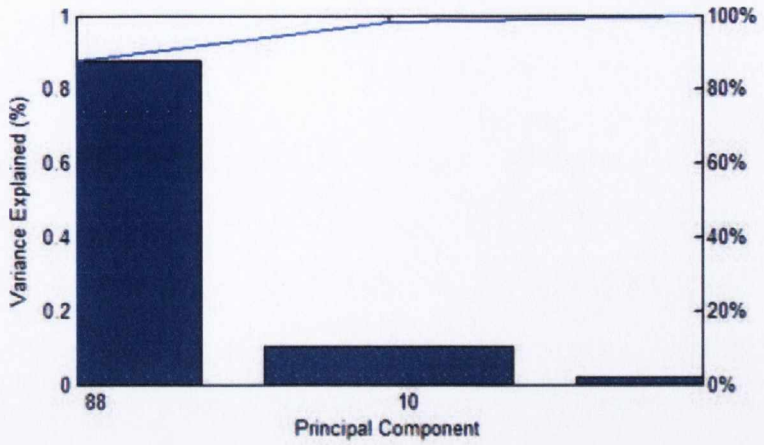

(a) PCA Scree Plot

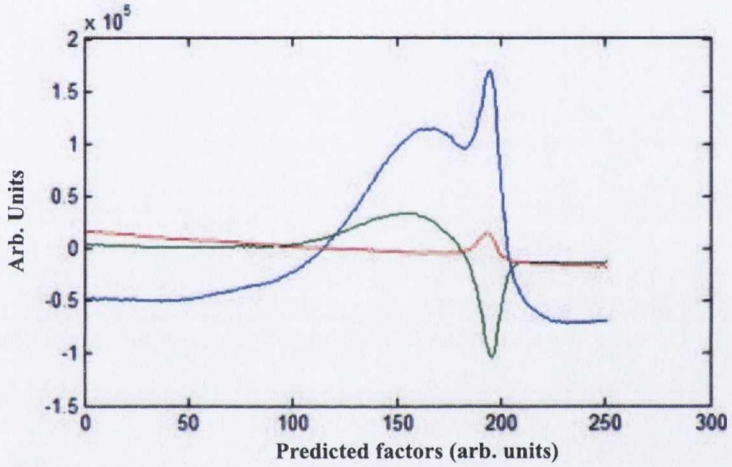

(b) PCA scores

Figure 5.10 – Results of PCA analysis on the sample set shown in Fig. 5.9. The Scree plot (a) shows the percentage of variance described by each score (b).

$$\begin{aligned} \mathbf{S}^T &= \mathbf{C}^{+T}\mathbf{X}_{\text{est}} \\ \mathbf{C} &= \mathbf{X}_{\text{est}}\mathbf{S}^{+} \end{aligned} \tag{5.9}$$

where $\mathbf{C}^{+} = \mathbf{C}(\mathbf{C}^T\mathbf{C})^{-1}$ and $\mathbf{S}^{+} = \mathbf{S}(\mathbf{S}^T\mathbf{S})^{-1}$ are pseudoinverses of the matrices $\mathbf{C}$ and $\mathbf{S}$ respectively. Non-negativity constriants are then imposed on these matrices.

Figure 5.11 illustrates the difficulty of using non-negative decomposition to force the calculated sources into component spectra using constrained MCR. The MCR algorithm

considers the sample set to be a linear combination of two basis spectra however the microcrystalline spectra is not static as it shapes changes depending on the crystallinity. This results in a crystalline basis function whose width is insufficient when the sample under investigation is highly crystalline and a width that is too large when the sample has a low crystallinity. Raman spectra are inherently non-linear, which is why non-linear distribution functions such as the Lorentzian and Gaussian functions are used. However errors resulting from this non-linearity are usually small when used with CLS fitting provided the scale of the reference spectra is large compared to the measured spectra.

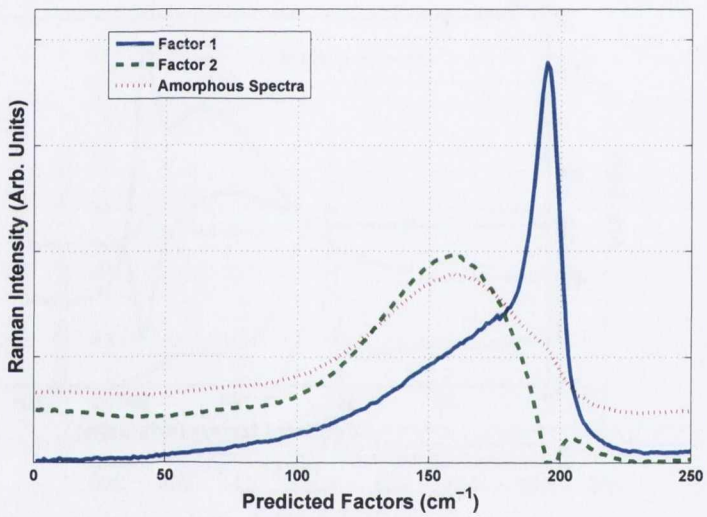

Figure 5.11 – A comparison between the factors found from the constrained MCR algorithm using the spectra shown in Fig. 5.9 and the spectra of amorphous Silicon.

5.6 XRD Analysis

X-Ray Diffraction a method of determining the arrangement of atoms within a crystal, in which a beam of X-rays strikes a crystal and causes the beam of light to spread into many specific directions was used by Smit et al. [58] as a supplementary technique to determine the crystalline content of microcrystalline Silicon. Using a Siemens D500 diffractometer based in DCU, the microcrystalline samples were measured as shown in Fig. 5.12.

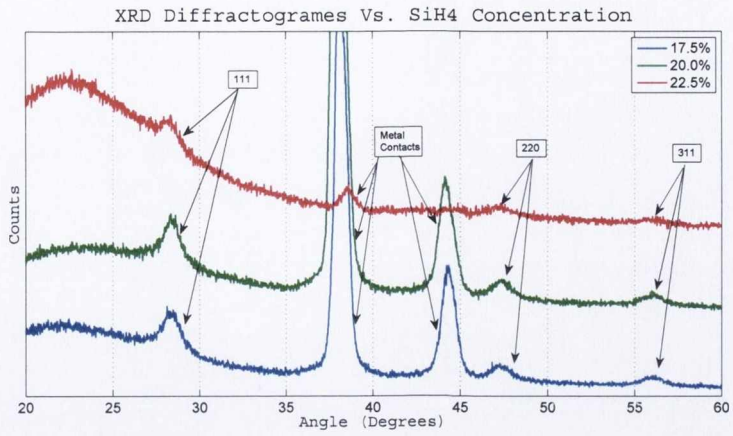

Figure 5.12 – X-Ray Diffraction results from samples 100121-02, 100121-03 and 100121-04 with different hydrogen concentrations.

Further attempts were made to improve on these results using the XRD system in the CRANN, TCD. For high resolution XRD (HRXRD) measurements the BRUKER D8 Discovery with a primary beam channel cut Ge (110) crystal monochromator, producing an intense, parallel Cu Ka monochromatic beam (with wavelength λ=1.5406), was used. The secondary beam was equipped with a LynxEye 1D detector allowing for fast mapping of the reciprocal space. The sample lattice parameters were determined by estimating the thin film lattice parameters from the relative separation in O and 2θ. The results for sample 100121-02 are shown in Fig. 5.13.

However it was not possible to improve upon the existing results. The obtained XRD results can be deconvoluted as described by Williamson et. al. [67] and shown in Fig. 5.14.

A simple, experimental, quantitative measure of the size of the crystalline grains can be obtained from the FWHM of the microcrystalline peaks shown in Fig. 5.14 via the Scherrer equation [68]

$$L = \frac{0.9\lambda}{W \cos\theta} \tag{5.10}$$

where W is the FWHM of the (111), (220) or (311) microcrystalline peaks. The preferred orientation is that the (220) plane is parallel to the film surface as indicated by its stronger rel-

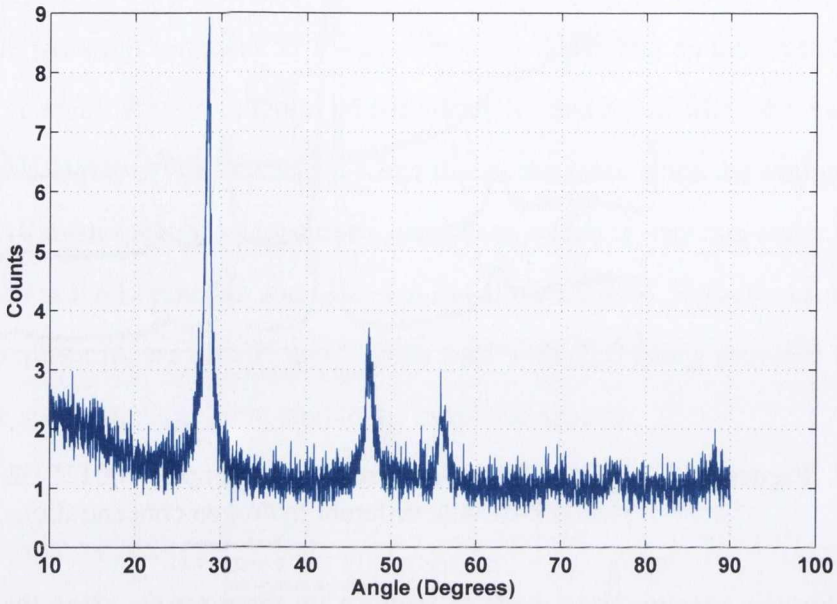

Figure 5.13 – XRD results of sample 100121-02 using the XRD system at CRANN, Trinity College.

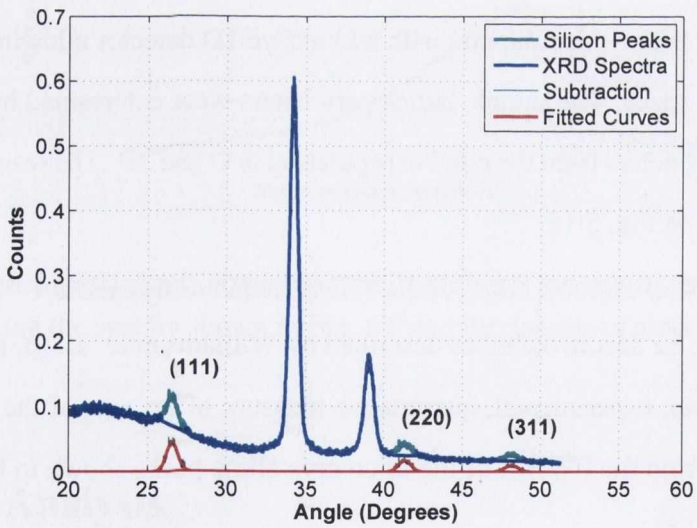

Figure 5.14 – Deconvolution of a microcrystalline sample. The lowest three Bragg peaks are visible in the microcrystalline sample [67].

ative intensity compared to the other peaks. The microcrystalline fraction can be calculated from [67] as the ratio of the integrated intensity (area) of the (111), (220) and (311) peaks to the total area from 14°to 65°. Although this method has been confirmed to be unreliable if

the amorphous fraction is greater than 40%. Despite several attempts it was not possible to get an accurate and repeatable microcrystalline fraction using XRD primarily as it was difficult to extract a reliable fit of the (111), (220) and (311) peaks as shown in Fig. 5.12 without small variations significantly impacting the results. Correspondence with Prof. Williamson confirmed the limitations of XRD analysis.

5.7 Conclusion

The crystallinity fraction, determined from the Raman spectra of micro-crystalline Silicon, decreases significantly with increasing wavelength as illustrated by the results in Table 5.4. This is expected as the crystalline regions grow in conical sections [61], the girth of which increases with distance from the substrate. This results in different crystallinity fractions at different depths due to the change in the absorption coefficient observed at different wavelengths. Different wavelengths can therefore be used to determine the crystallinity at various depths. However this growth method also means the micro-crystallinity and the resulting Raman analysis is not uniform but rather an average of the crystallinity within the Raman collection region.

Both the polarisation and chemometric technique significantly attenuates the influence of the second order phonons and allows for more accurate calculation of the crystallinity fraction with highly crystalline samples. The chemometric technique requires significantly shorter exposure time and could potentially be used to rapidly map regions of the sample under investigation. If the sample is highly crystalline and only the phonon at 600cm^{-1} is used to determine the scaling factor than the CLS method should give the best results. The XRD results were also carefully analysed and despite the high importance given to the XRD results in [58], it was concluded that this was not an accurate method of measuring the crystallinity fraction.

Chapter 6

Germanium Stripes

6.1 Introduction

Germanium is another material that has potential for use in a solar cell due to its excellent electrical properties. With a band gap of 0.66 eV [69] energy from the infra red region of the solar or thermal spectrum can be absorbed and converted into electrical energy. The issues of availability and cost can be overcome by using thin-films instead of thick wafers of Germanium. However crystalline Germanium is expensive to purchase and therefore not suitable for mass production. Nevertheless, solid-state structures can be produced using low cost thin-film deposition techniques combined with a rapid melt growth (RMG) process, in which the deposited Germanium is heated very quickly to just above the melting point temperature, described in detail below. Raman Spectroscopy was used to determine the crystalline quality of the Germanium after the RMG process for different process parameters. Initial experiments using Raman spectroscopy on the integration of GeOI with Silicon and Sapphire substrates have demonstrated that good quality Germanium crystalline structure can be obtained. In this chapter the conditions for RMG were examined using Scanning Electron Microscopy (SEM), Transmission Electron Microscopy (TEM), Atomic Force Microscopy (AFM) and micro-Raman Spectroscopy.

Table 6.1 – Fabrication process of investigated Germanium samples.

Sample	RTA temperature (°C)	Germanium thickness (nm)	notes
PVD Sample 1	941	170	Directly on Si
PVD Sample 2	941	170	
PVD Sample 3	941	210	
PVD Sample 4	961	210	
PVD Sample 5	964	170	
PVD Sample 6	981	170	
PVD Sample 7	985	210	

6.2 Sample Preparation

The RMG fabricated Ge stripes were obtained in collaboration with Queen's University Belfast. Two techniques have been used for deposition of the Germanium, Physical Vapor Deposition (PVD) and Chemical Vapor Deposition (CVD). PVD, is used to deposit thin films by the condensation of a vaporised form of the desired material onto the Silicon wafer. CVD, is used to deposit thin films by the exposure of the wafer to one or more volatile precursors which react on the substrate producing the thin film. The process parameters are also varied, aiming for an optimal Germanium crystalline structure and to verify the lateral growth of Germanium on insulator. The parameters include Germanium thickness, crucible materials (Silicon Dioxide), anneal temperature and substrate.

The rapid melt growth (RMG) process uses a micro-crucible to hold the molten Germanium [70, 71]. The crucible is formed on the surface of an oxidized Silicon wafer with the Germanium contacting the Silicon in a seed window. In the fabrication process for PVD samples, the Germanium is deposited directly on top of the oxide. The Germanium chemical vapor deposition process, however, is selective to Silicon surfaces and thus requires a thin Silicon layer to be deposited on the oxide prior to the Germanium deposition. The deposited Germanium is then patterned into narrow stripe features with 3 to 4μm width and 60 to 400μm lengths. These stripes are then covered with a capping layer of low temperature oxide to form the micro-crucible as shown in Fig. 6.1. Rapid thermal annealing (RTA) is applied to heat the Germanium above its melting point (938 °C) for a few seconds. After annealing, the Germanium cools and crystallizes starting from the Silicon seed and contin-

uing laterally along the crucible. The seed region is expected to be defective because of the lattice mismatch between Silicon and Germanium. The dislocations will extend out from the seed region but terminate at the micro-crucible walls, and thus good crystalline quality can be obtained beyond this region.

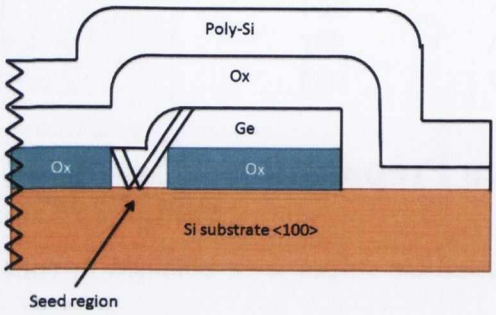

Figure 6.1 – Schematic cross section of capping layer of RMG structure.

If the capping layer is comprised of only Silicon dioxide, significant delamination of the stripes is observed and the integrity of the crucible is compromised as shown in Fig. 6.2. In the case of a capping layer comprising only low temperature oxide (PECVD oxide), significant cracks and delamination of the stripes were observed and crucible integrity is compromised as shown in Fig. 6.2. When heat treatment is applied above the Germanium melting point (938 °C), it tends to congeal into ball shapes (balling phenomenon) [72] causing the crucible to become strained. The issue is more severe with the wide stripe since the micro-crucible cap is wider and hence less rigid.

The micro-crucible was reinforced by adding a 1 μm thick poly-crystalline Silicon (polysilicon) layer on top of the PECVD oxide capping layer. The polysilicon was deposited by low pressure chemical vapor deposition (LPCVD) at 620 °C. Addition of this layer was found to minimize Germanium balling and prevent delamination, resulting in smooth defect free Germanium stripes as shown in Fig. 6.3. The defect free structures have a length from 60 to 400μm and are composed of 170nm thick PVD Germanium stripes. Addition of this 1 μm polysilicon layer on top of the PECVD oxide capping layer [73] provide a more robust micro-crucible and prevents delamination as has been demonstrated by Raman spectroscopy.

SEM images of the Germanium stripes with a 60μm length and a 3 to 4μm width are

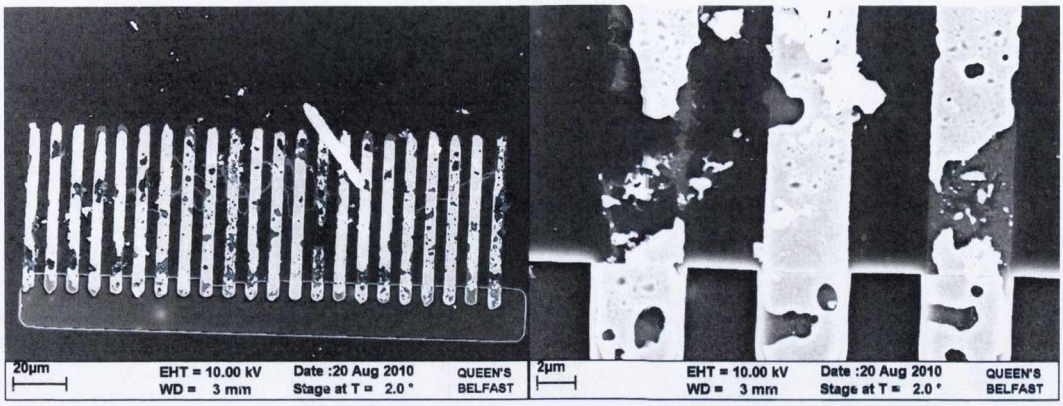

Figure 6.2 – Degraded Germanium stripes annealed at 942 °C. Degradation is due to the lack of a poly Silicon capping layer.

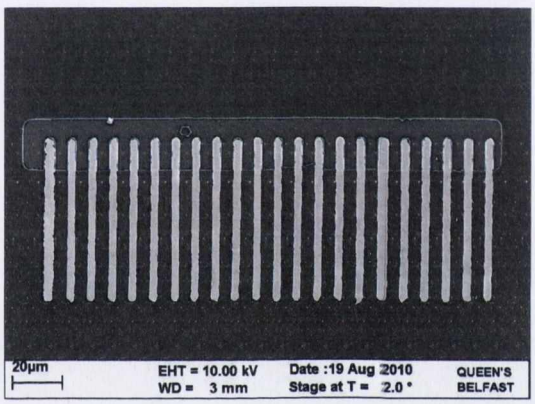

(a)

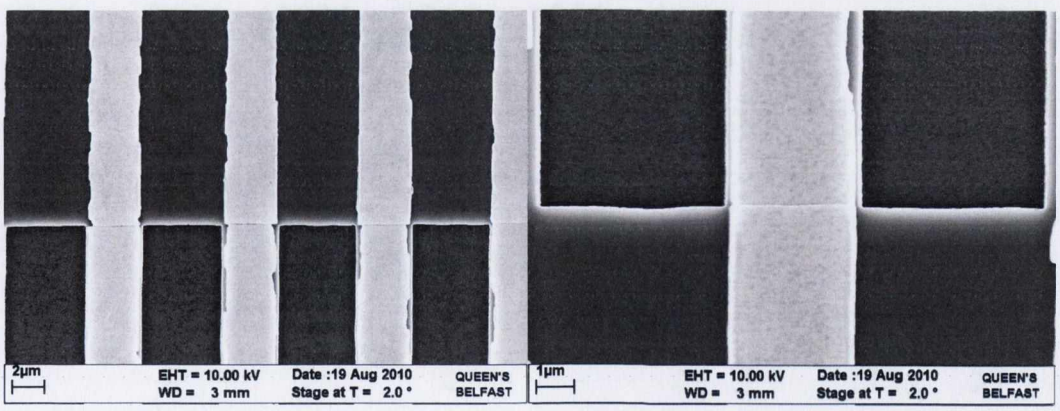

(b) (c)

Figure 6.3 – SEM images of 170nm thick Germanium stripes annealed at 942 °C for 1s. No degradation of stripes is visible due to the poly Silicon capping layer.

shown in Fig. 6.3. The crystalline structure of the PVD Germanium stripes was analyzed by Raman spectroscopy for comparison with the spectra of a bulk (100) n-Ge wafer. The Raman spectrum of bulk crystalline Germanium demonstrates an intense longitudinal-optical phonon (LO) Ge-Ge mode with a peak position at 300.2 cm^{-1} [74] similar to Silicon and a linewidth measured on our Renishaw system of $\sim$3 cm^{-1}. The presence of tensile or compressive strain in the structure results in shift of this LO peak from the unstressed Germanium peak position to the low- or high-frequency side, respectively [46]. Prior to RMG the Raman spectrum in Fig. 6.4 demonstrates a relatively wide LO peak with a linewidth of $\sim$8 cm^{-1} from the Germanium structures before annealing and comparable to the Germanium wafer reference which has a linewidth of 3.2 cm^{-1}.

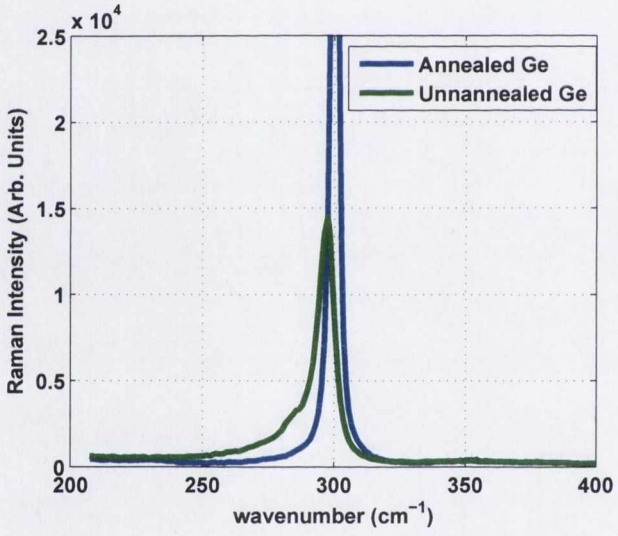

Figure 6.4 – Raman spectra before (green line) and after (blue line) anneal. The Raman spectra of the annealed sample shows that it is significantly more crystalline as a result.

The asymmetry, observed from the low frequency side of the peak, is characteristic of a partially amorphous structure. This partial crystallinity occurs in the Germanium during the deposition of the capping layer when process temperatures can reach 620 °C. After the rapid thermal anneal the Raman spectra measured and shown in Fig. 6.4 shows a sharp and symmetric peak (with linewidth of $\sim$4 cm^{-1}) indicating that the RTA has improved the crystalline quality of Germanium. The result of this process is that straight, smooth

stripes with no visible delamination and good crystal structure are obtained. The quality of Germanium crystalline structure was examined by micro-Raman spectroscopy as shown in Fig. 6.5. The crystallinity after thermal annealing compares very favourably with that of the single crystal Germanium wafer indicating that the RMG process produces Germanium of good crystallinity.

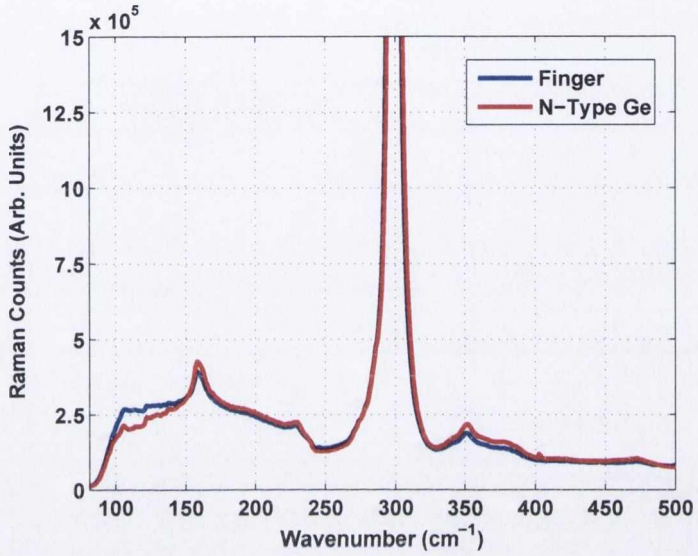

Figure 6.5 – Raman spectra of Germaium annealed at 942°C and reference n-type single crystal sample.

Atomic Force Microscopy (AFM) images of samples 3 and 4 obtained by means of NT-MDT Ntegra instrument using an upright AFM stage installed our laboratory are shown in Fig. 6.6

These images confirm that the thickness of this this fabricated Germanium stripe is slighly less than 170nm. The 3D plot shown in Fig. 6.7 shows how the Raman spectra changes as as it is brought horizontally across the sample. The Germanium peak is pronounced when the spectrometer is positioned above the stripe and the Silicon peak is pronounced when it is over the substrate.

The Transmission Electron Microscopy (TEM) measurements performed on the Ge stripes sample 2 is shown in Fig. 6.8. The TEM image demonstrate a very good quality of Ge stripe without visible sign of threading and misfit dislocations and very small number of defects.

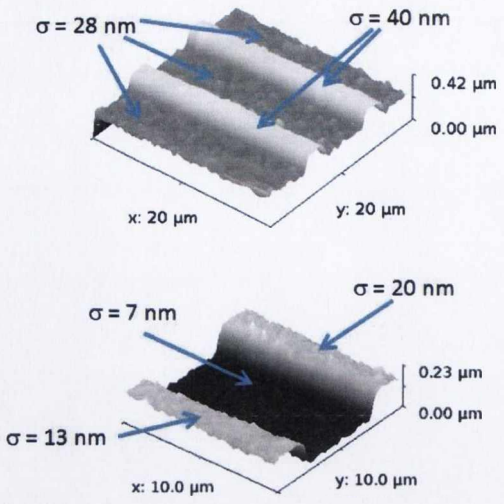

Figure 6.6 – AFM images of sample 2 (top).

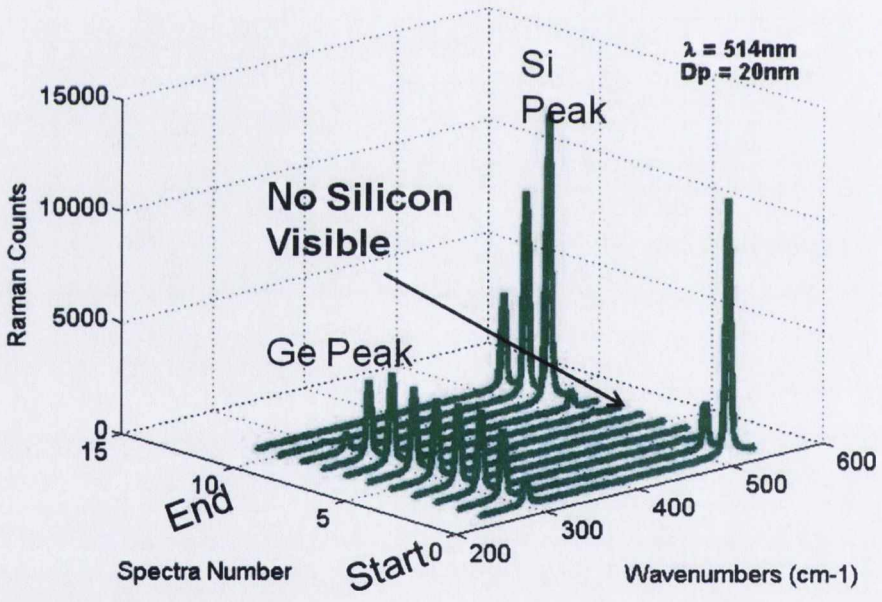

Figure 6.7 – 3D plot showing the change in the Raman spectra.

6.3 Analysis of PVD Samples

Micro-Raman line-mapping measurements were carried out along the length of PVD Germanium stripe for samples annealed at higher temperature (980 °C) with thicknesses of 170 nm and 210 nm. The 210nm samples were visibly more uniform than the 170nm samples as

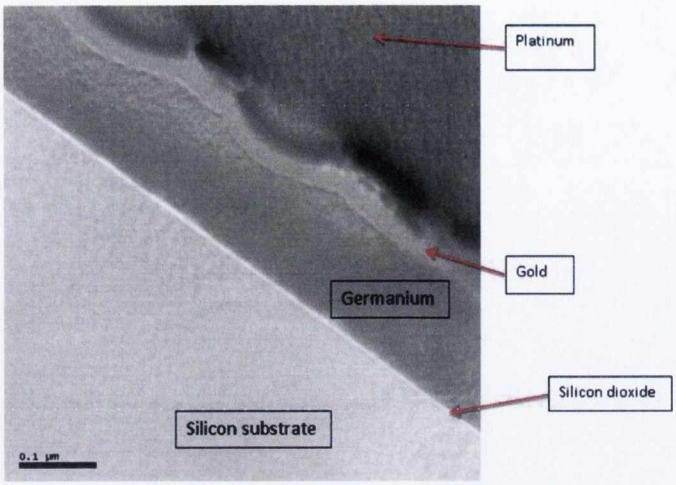

Figure 6.8 – SEM image of sample 2, very few defects are visible.

shown in Fig. 6.9. This is due to the more stable structure of the 210nm stripes.

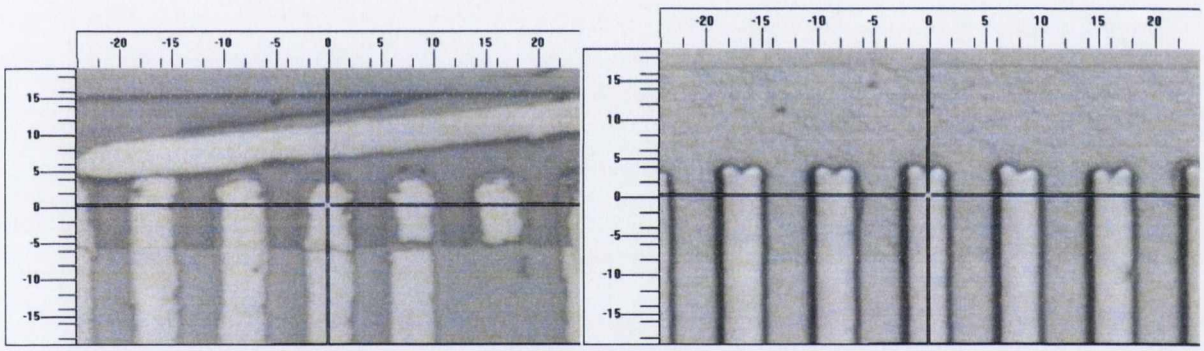

(a) 170nm **(b)** 210nm

Figure 6.9 – Optical 50x magnification of (a) 170nm and (b) 210nm thick Germanium stripes. The 170nm stripes are notably more degraded that the 210nm stripes.

The Raman peak position which reflects the stress in the Germanium taken along the length of the 170nm stripes tended to be significantly more erratic than those taken along the 210nm stripe, due to the degradation seen under the optical microscope.

Several different samples were examined using the 633nm excitation wavelength, which has a depth of penetration of 70nm in Germanium. Due to the small size of the stripes $\sim$ 3-4µm the 100x objective was used as it provides a smaller spot size. The Raman analysis consisted of vertical line mapping using a 2 µm step size. The results were analysed making

extensive use of the MATLAB scripts in the appendix.

Single crystal N-Germanium wafer

Raman spectra of an n-Germanium wafer were measured to provide a baseline with which our results could be compared.

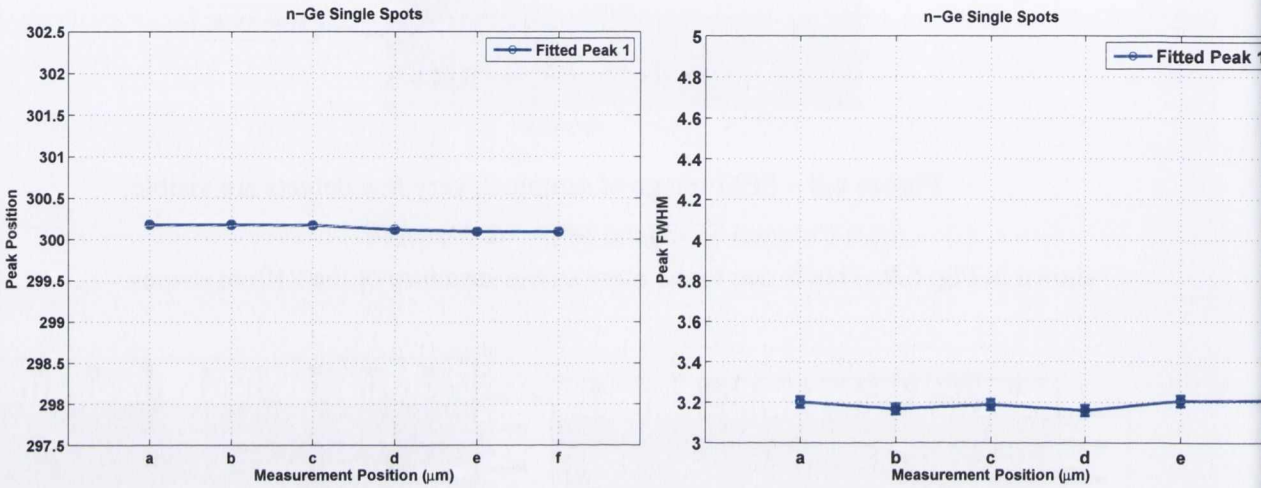

(a) Position **(b)** FWHM

Figure 6.10 – Single crystal N-Germanium Raman measurements for comparisons.

Sample 1

Pure Germanium has a peak position of approximately 300.2 cm^{-1} (Fig. 6.10). The peak positions visible in Fig. 6.11(c) show a decrease in this frequency and in certain positions points jump mainly to the low frequency side. This lowering of the Raman frequency is primarily attributed to tensile stress [46]. The locations of high tensile stress correspond to a degradation in crystallinity, indicated by an increase in the Full Width Half Maximum (FWHM) shown in Fig. 6.11(d). This tensile stress is attributed to the different thermal expansion coefficient of Ge compared to the underlying oxide cooling down to room temperature [75].

Fig. 6.11 shows that a rough periodicity is present. Germanium congeals into small drops due to surface tension and it is possible that this stress distribution demonstrates the initial phase of this phenomenon due to the breakdown of crystallinity. The increase of FWHM at

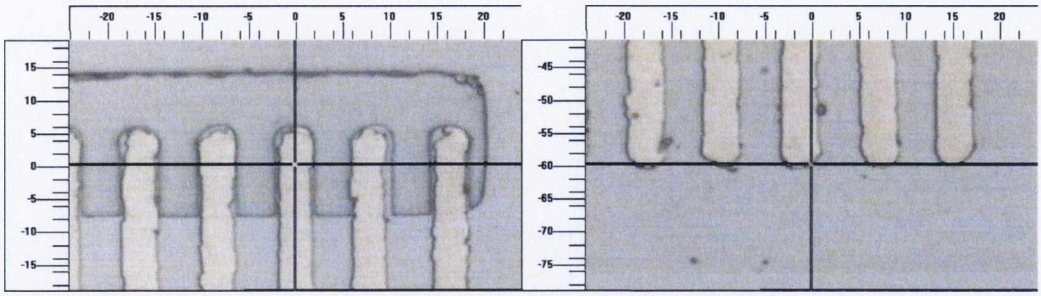

(a) Initial point of line mapping (b) Final point of line mapping

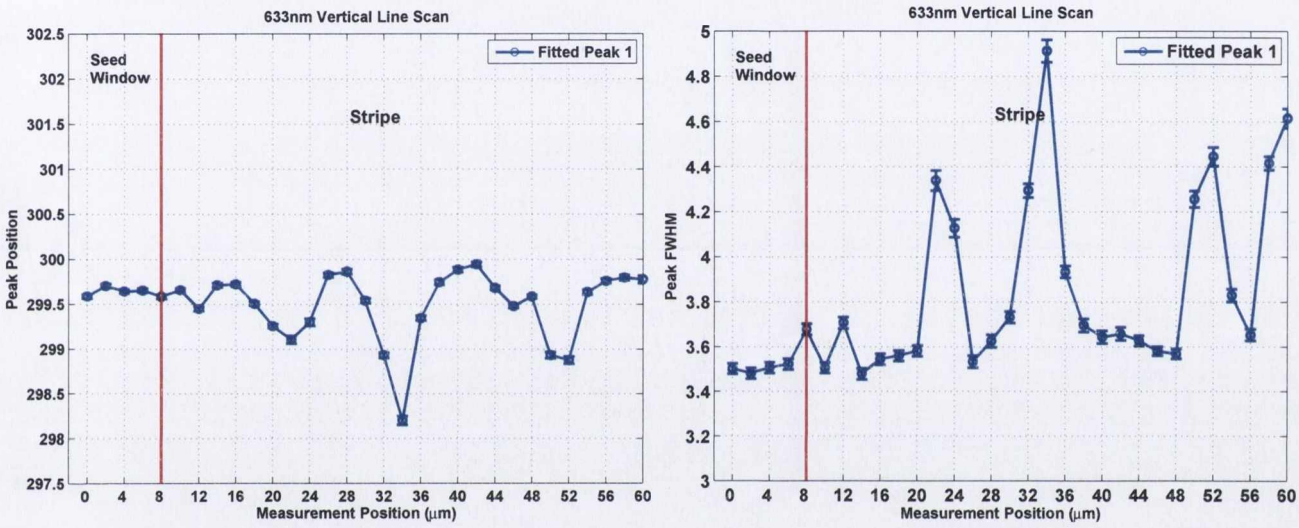

(c) Position (d) FWHM

Figure 6.11 – Vertical Raman line mapping of sample 1
Temperature of RTA 941°C, Ge Height 170nm and the oxide is removed.

the end of the strip is probably due to the fact that the measurement spot was shifted from the middle of the stripe to the edge. This results in a Raman spectrum with a much smaller intensity as the spot now includes both Silicon and Germanium.

Sample 2

Sample 2 has no seed window and the Germanium is deposited directly on Silicon unlike sample 1 (Fig. 6.11). It is important to note that this sample has been grown directly on Silicon without an intermediate oxide layer unlike the results shown in Fig. 6.11.

This replicates the seed window configuration as the Germanium is in direct contact with

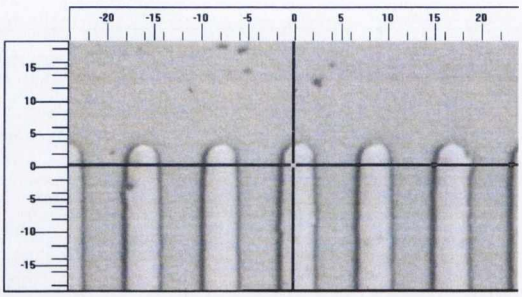

(a) Initial point

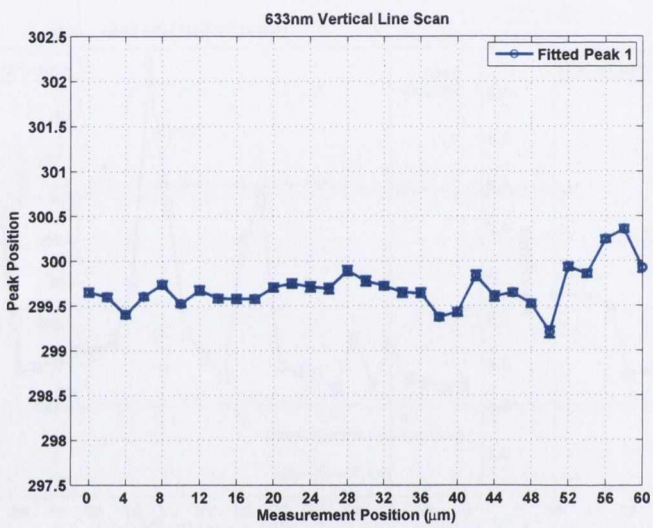

(b) Position

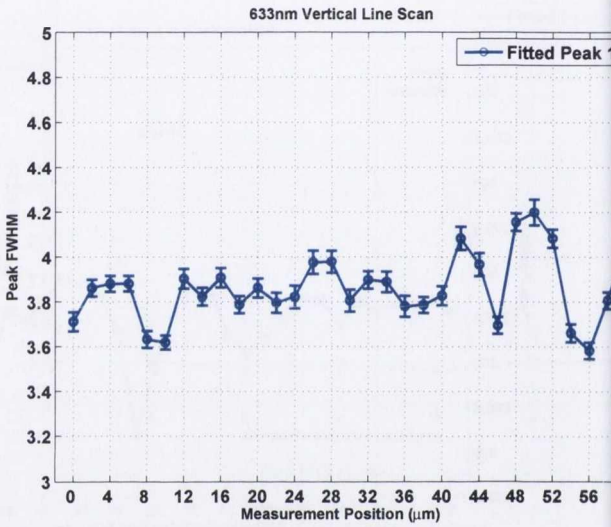

(c) FWHM

Figure 6.12 – Vertical Raman line mapping of sample 2
Temperature of RTA 941°C, Ge height of 170nm, no Seed Window with Ge deposited directly on Si, the oxide is removed. Only the initial point is shown unlike Fig. 6.11

the Si. The FWHM is approximately ~0.2-0.3 larger than Fig. 6.11(d), excluding the erratic sections. Although the FWHM does not have the sudden quite widely dispersed erratic changes of Fig. 6.11(d) it has a much more uneven profile if those areas are excluded. This is due to the lattice mismatch and the resulting high defect density that is expected in the seed window.

Sample 3

Sample 3 has a thicker Germanium layer of 210nm compared to the annealed sample (Fig. 6.11, 170nm).

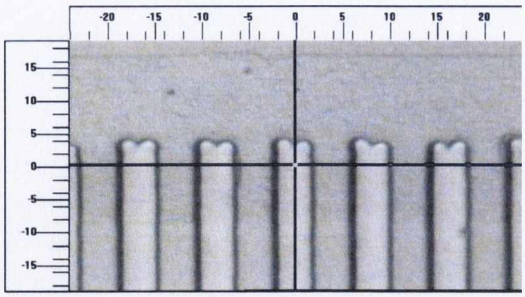

(a) Initial point

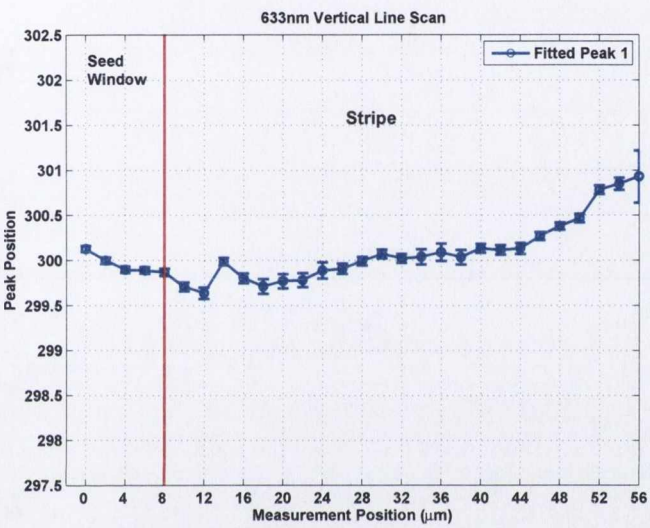

(b) Position

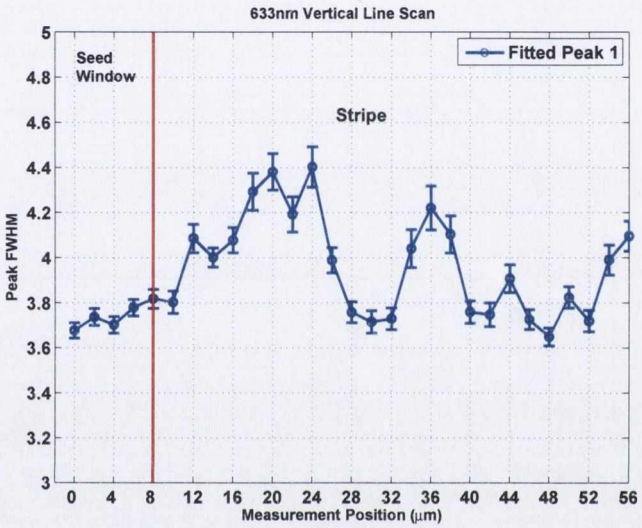

(c) FWHM

Figure 6.13 – Vertical Raman line mapping of sample 3
Termperature of RTA 941°C, Ge height of 210nm and oxide removed.

Fig. 6.13(b) appears to indicate a significantly more uniform stress distribution than Fig. 6.11(c) the periodic stress seen there has been significantly reduced possibly due to the thicker Germanium layer. However, the FWHM plots indicate that the crystallinity is far from uniform, this time however it does not appear to be the result of stress instead it could be the result of insufficient time or temperature for proper crystallisation of the larger mass of Germanium.

Sample 4

Sample 4 shown in Fig. 6.14 has a higher RTA temp compared to sample 3 (Fig. 6.13, 941°C).

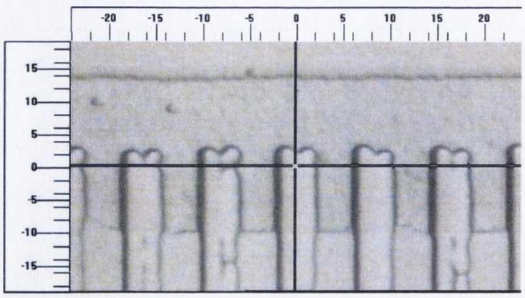

(a) Initial point

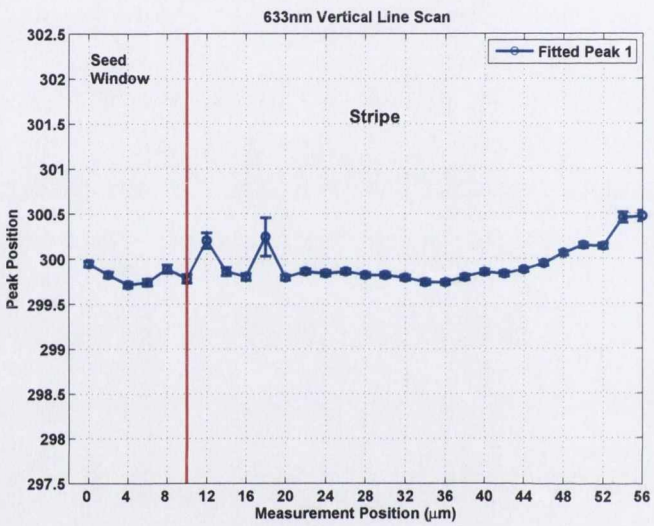

(b) Position

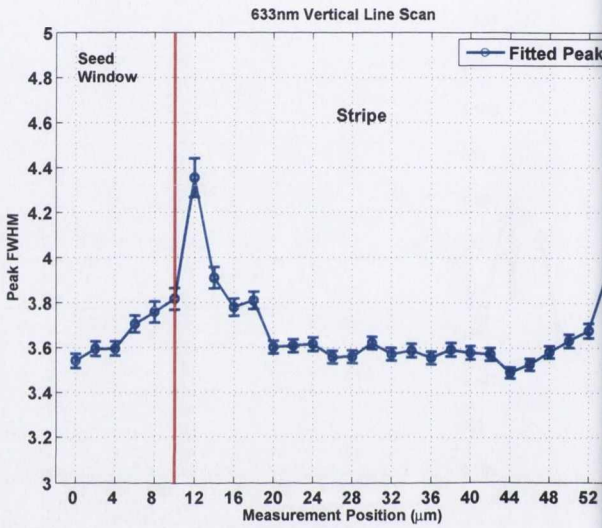

(c) FWHM

Figure 6.14 – Vertical Raman line mapping of sample 4
Temperature of RTA 961°C, Ge height of 210nm and oxide removed.

Fig. 6.14(b) shows an average position slightly higher (approximately 299.8 cm^{-1}) than the thinner samples that have had an average of 299.6cm^{-1}. 299.8 cm^{-1} is closer to the peak position of pure Germanium (Fig. 6.10) indicating reduced tensile stress.

The FWHM plot, Fig. 6.14(c) is significantly smoother than sample 3, Fig. 6.13(c), demonstrating that the increased temperature has resulted in an improved crystalline structure, validating the theory that the poor crystallinity was due to thermal growth conditions.

The two jumps in the FWHM plot appear to be repeated across several different samples and could be a result of interaction between the seed window and the external strip potentially due to dislocation termination or possibly due to the removal of the oxide layer which could result in small cracks. This is seen in the SEM image shown in Fig. 6.15.

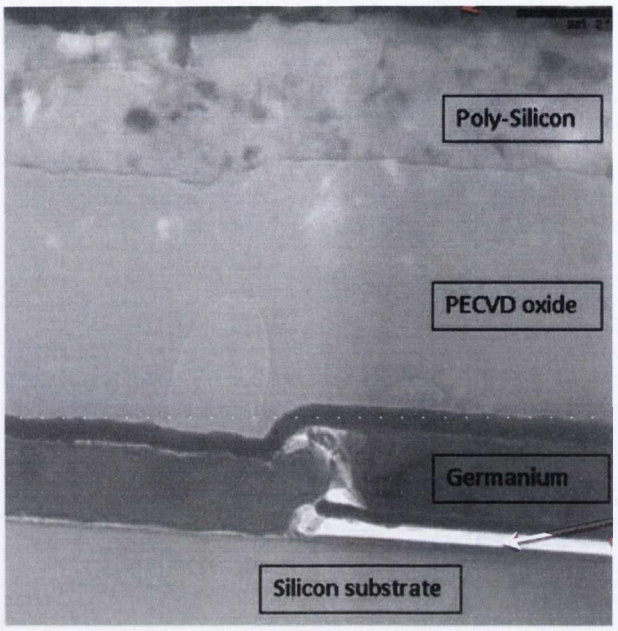

Figure 6.15 – SEM image of sample 3. Cracking is visible between the seed window and the remainder of the stripe.

Sample 5

Sample 5 has a higher RTA temperature compared to the sample 1 (Fig. 6.11, 941°C) and a thinner Ge layer compared to sample 4 (Fig. 6.14, 210nm).

The stress distribution found from the peak position shows significantly fewer erratic jumps than sample 1 shown in Fig. 6.11. The FWHM plot indicates that any areas of reduced crystallinity are the result of stress and not improper crystallisation. Discounting the change in FWHM due to stress (due to the thinner Germanium layer), it appears to be very uniform in areas where the peak position (and therefore stress) is uniform, corresponding with the results for sample 4 and strongly indicating that the thinner (170nm) Germanium layer is primarily responsible for the erratic stress distribution.

The average peak position at approximately 299.5cm^{-1} appears to be less than that for sample 4 (Fig. 6.14) indicating a higher tensile stress. The thicker Germanium layer (210nm) of sample 4 would appear have more of an effect in reducing the average tensile stress along the stripe than the higher temperature (941°C). This is also shown in the Fig. 6.17 (981°C, 210nm) which has an average tensile stress that is similar to the annealed sample (Fig. 6.11,

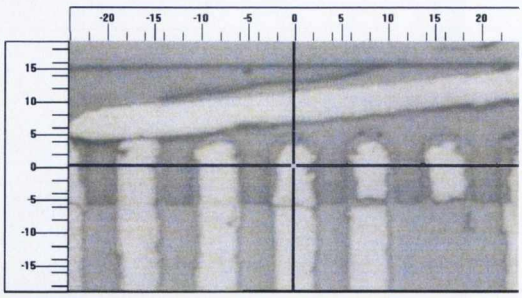

(a) Initial point

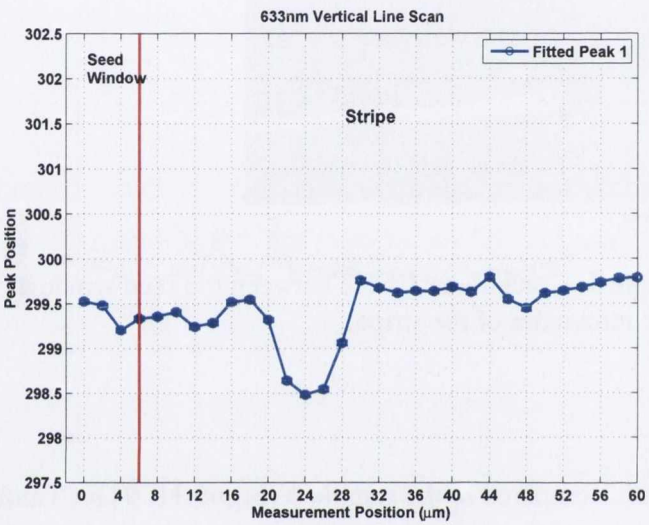

(b) Position

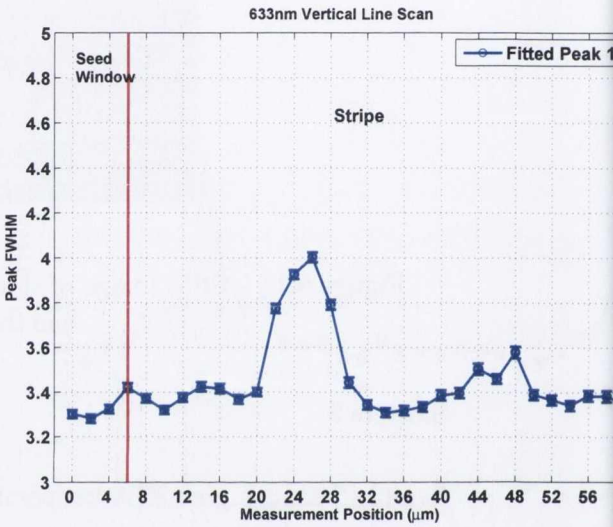

(c) FWHM

Figure 6.16 – Vertical Raman line mapping of sample 5
Temperature of RTA 964°C, Ge height of 170nm and oxide removed.

941°C, 170nm) and sample 5 (Fig. 6.16, 961°C, 170nm). The theoretical Raman depth of penetration (d_p) for Germanium is 70nm for the 633nm laser so this could be an influence if the stress or crystallinity is expected to change across the thickness of the Germanium layer however assuming the Germanium is single crystal the crystallinity fraction should be constant.

In these comparisons it is important to also note the FWHM. In Fig. 6.14(c) the FWHM is slightly higher at approximately 3.6cm^{-1}, pure Germanium has a FWHM of 3.2cm^{-1} (Fig. 6.10) and the two samples with the best FWHM excluding erratic regions, sample 5 (Fig. 6.16) and sample 6 (Fig. 6.17) both have average FWHM of approximately 3.4cm^{-1}. Despite the high FWHM (Fig. 6.14(c)) the average tensile stress is smaller than the other

samples discussed. This could possibly indicate that the decrease in stress is related to the presence of threading dislocation throughout the structure that are relieving the stress as shown in the peak position graphs but simultaneously resulting in degraded crystalline quality.

Sample 6

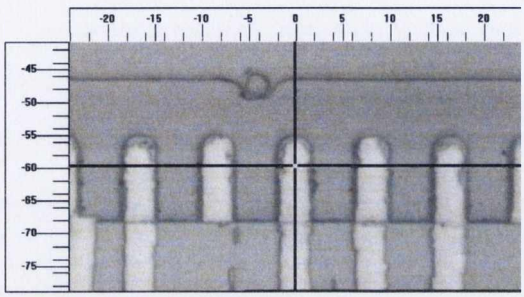

(a) Initial point

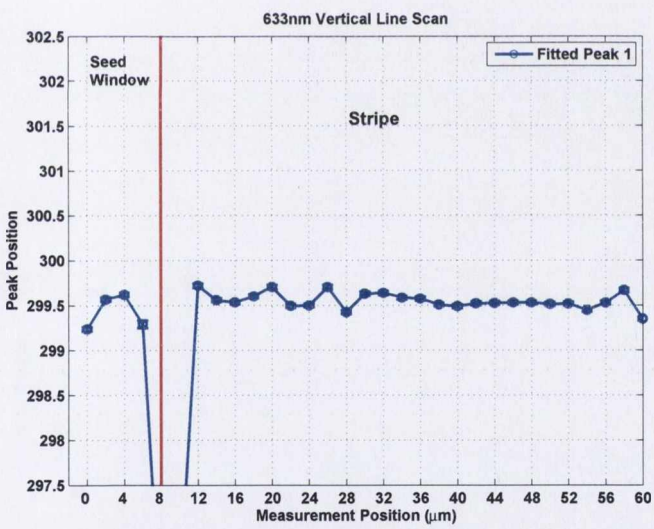

(b) Position

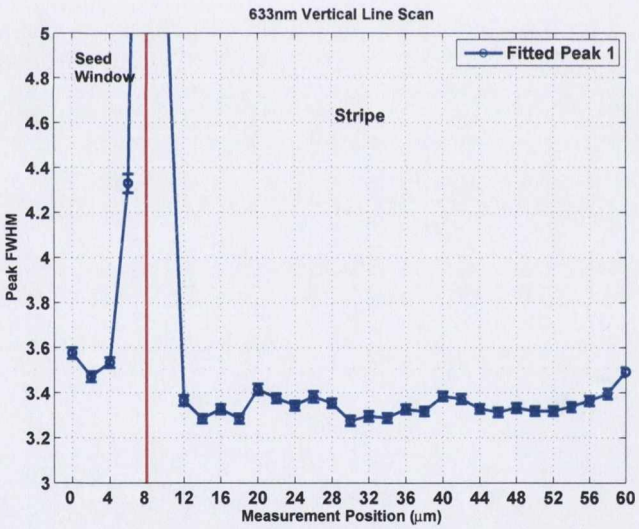

(c) FWHM

Figure 6.17 – Vertical Raman line mapping of sample 6
Temperature of RTA 981°C, Ge height of 170nm and oxide removed.

Sample 6, shown in Fig. 6.17 has a higher RTA temp compared to sample 5 (Fig. 6.16, 961°C).

The very uniform stress distribution is a significant improvement over that of sample 5 indicating that the stress and the associated decline in crystallinity (attributed to island

formation) seems to have been eliminated at this temperature in a similar manner to what was achieved using the thicker Germanium layer. Although Fig. 6.17 which was measured over a longer distance could possibly show signs of this reoccurring.

The average peak position (299.5cm^{-1}) indicates that it is slightly more stressed than sample 4 (210nm, 961°C) and sample 3 (210nm, 941°C) as discussed above. The FWHM of approximately 3.4cm^{-1} indicates it is of good crystallinity. So this sample removes the erratic stress distribution seen in previous samples while simultaneously maintaining uniformity and good crystallinity across the stripe. The FWHM is larger in the seed window which corresponds to the results in [71].

Sample 6 - 400μm length

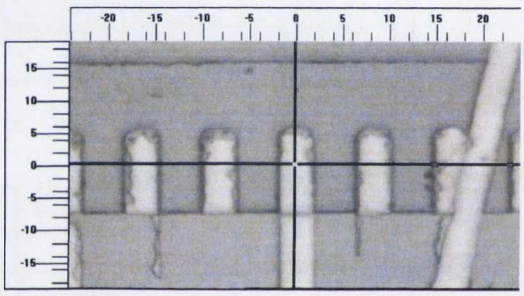

(a) Initial point

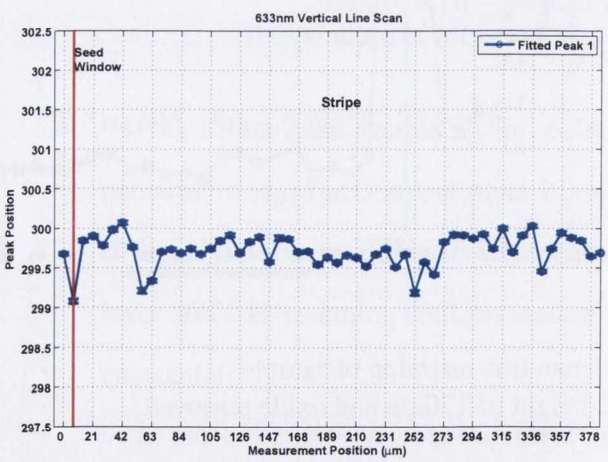

(b) Position

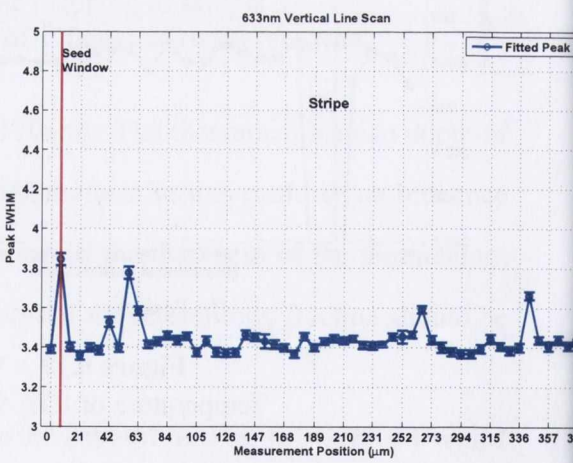

(c) FWHM

Figure 6.18 – Vertical Raman line mapping of long 400 μm sample 6 Temperature of RTA 981°C, Ge height of 170nm and oxide removed.

In this longer line mapping, the periodic stress and associated decrease in crystallinity

reoccurs expect the gap between the erratic jumps, is longer than for sample 5 or the annealed sample, indicating that the higher temperature might increase the size of the Germanium islands (assuming that is the cause of these erratic jumps).

These results show that the longer stripes maintain good crystallinity despite their length. This indicates that the RMG technique is effective for Ge stripes with substantial length.

Sample 7

Sample 7 received high temperature anneal of 985 °C and has a height of 210nm.

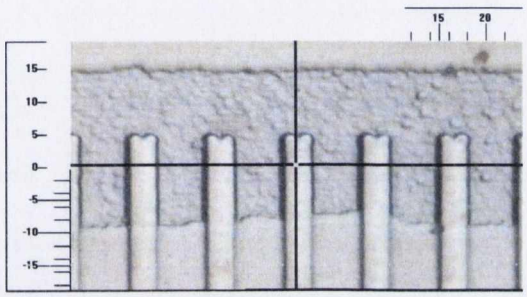

(a) Initial point

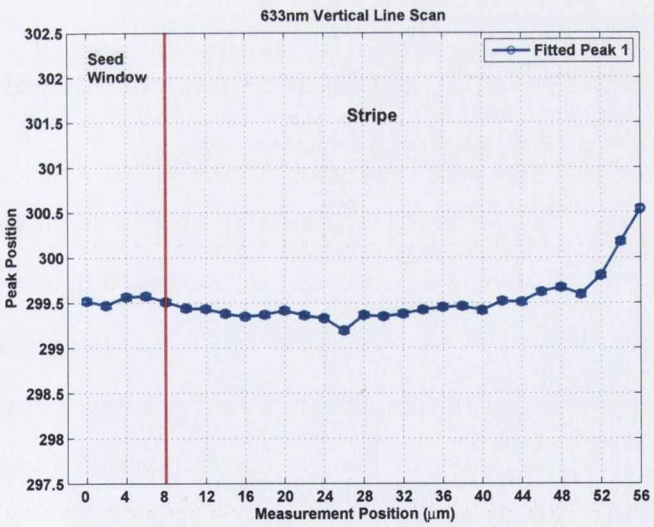

(b) Position

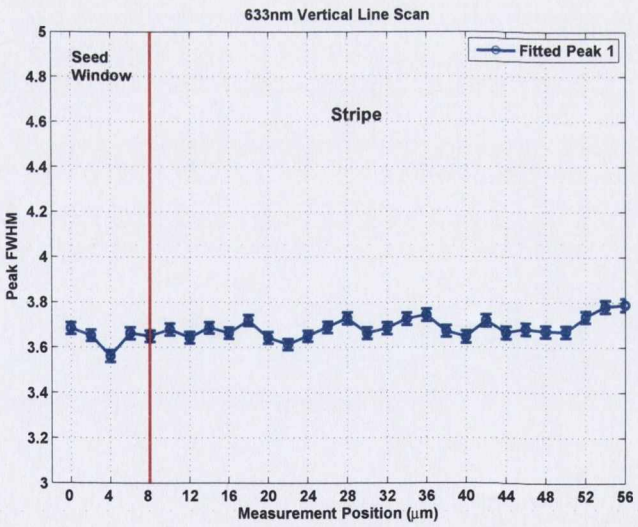

(c) FWHM

Figure 6.19 – Vertical Raman line mapping of sample 7
Temperature of RTA 985°C, Ge height of 210nm and oxide removed.

Tensile stress is still apparent by the reduction in the peak position. The crystallinity appears inferior to sample 6, all the 210nm stripes measured tended to have FWHM that

were larger than the 170nm stripes indicating reduced crystallinity.

Sample 6 - Long Accumulation time

Finally Fig. 6.20 demonstrates the Raman spectra of a Ge stripe and the pure Ge wafer in the region where the SiGe band would be expected.

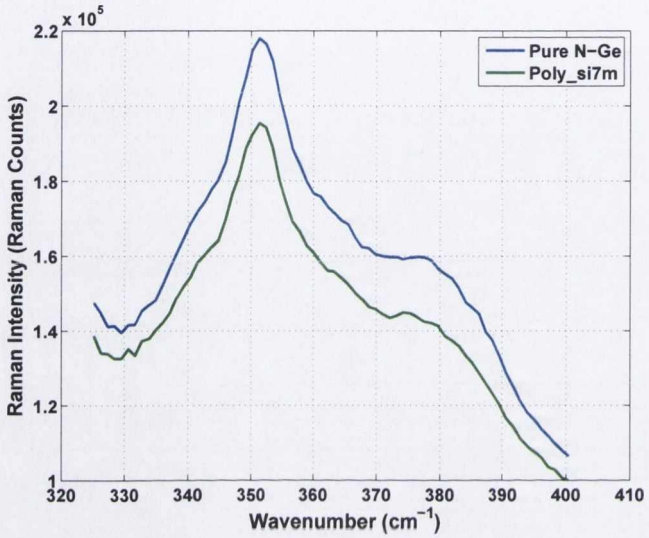

Figure 6.20 – Raman spectra of pure Germanium (reference sample) and sample 6 obtained with accumulation of 35 min in the region 320 410 cm-1, which demonstrated the absence of SiGe peak.

A SiGe peak expected at approximately 380cm^{-1} was previously described in the similar structures fabricated using the RMG process [71]. No SiGe peak was observed in any of the samples, in order to determine if the SiGe peak was present but very weak. In order to determine if a weak SiGe peak was present sample 6 was exposed to a very long exposure time of 30 minutes. Fig. 6.20 shows that despite an extended measurement time both Raman spectra are identical and no SiGe peak is visible. No SiGe peak was visible in any of the PVD deposited samples.

6.4 Analysis of CVD Samples

In the case of Chemical Vapour Deposited (CVD) Germanium, it is necessary to first deposit a thin Silicon layer on the oxide to enable the selective Germanium deposition. This is because it is impossible to deposit Germanium by CVD on the oxide but only selectively onto Silicon. Therefore, a thin Silicon layer is required to be deposited on SiO_2 prior to the CVD Germanium deposition. After the RTA process, the Raman spectrum shows a sharp Ge-Ge peak at 300 cm^{-1} with linewidth of < 4 cm^{-1} for the CVD process. This indicates a good crystalline quality of Germanium stripes comparable to the bulk Germanium (FWHM = 3.2 cm^{-1}) as shown in Fig. 6.21. The peak position for both samples is slightly shifted to the low-frequency side due to the tensile strain. A peak corresponding to SiGe bonding is observed in the Raman spectrum around 380-390 cm^{-1} in case of CVD sample annealed at $T > 940$ °C.

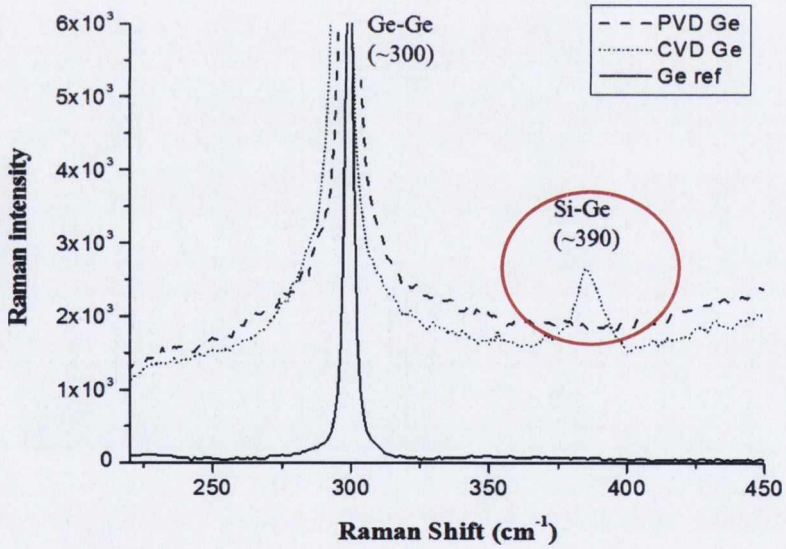

Figure 6.21 – Raman spectra for bulk Germanium reference, PVD and CVD samples after RMG at a distance of 36μm from the seed window.

The presence of SiGe is believed to result from the thin Silicon layer. Miyao et al. [71] observed a similar SiGe peak in the RMG Germanium grown by molecular beam epitaxy and attributed this to Silicon diffusion from the seed window and formation of Si-Ge bonding at

(~971 °C). In our PVD samples SiGe was not found even for high temperature (<985 °C) annealing where diffusion of Silicon from the seed window might be expected. Instead the SiGe peak seemed to result from an interaction with the Silion layer overlaying the oxide that is required for CVD deposition.

6.4.1 Anomalous Silicon Peak

A Silicon peak appeared in the Raman spectra of all measurements from the Germanium stripes. The source of this Silicon peak was unknown as the samples were etched and all layers (namely polysilicon capping layer and oxide layers) were removed. In order to determine the source of the Silicon peak a Zeiss Auriga - Focused Ion Beam (FIB), based in CRANN, was used to remove a small section of the sample allowing the cross section to be accessed for oblique SEM and EDX measurements as shown in Fig. 6.22.

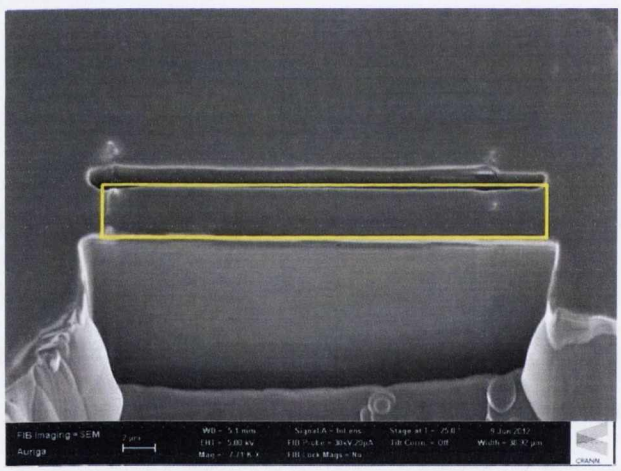

Figure 6.22 – A small section of the sample is removed used the Focused Ion Beam. Fingers are not visible due to a lead coating deposited to protect the sample.

An SEM image can then be obtained of the cross section shown in Fig. 6.23.

Using the Backscattered electrons resulting from the SEM images it is possible to identify the elements in the sample, as shown in Fig. 6.24.

The bottom section indicates that a layer, approximately 850nm thick surrounding the Germanium stripes is a composite of Silicon and Oxygen. This is the polysilicon capping

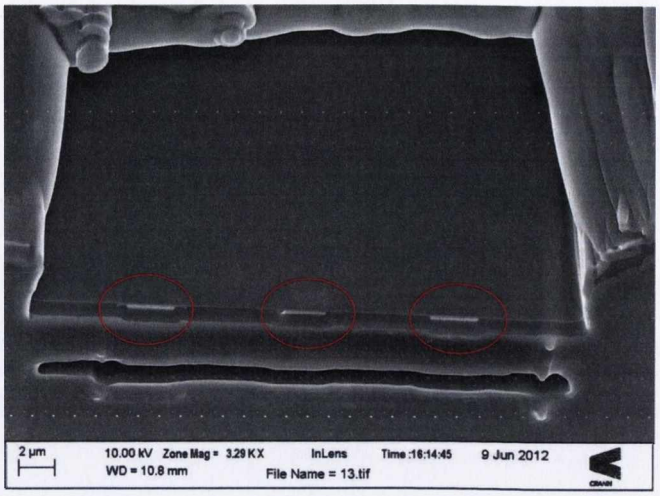

Figure 6.23 – SEM image of the cross section, the three circled rectangles are the Germanium stripes. The image is inverted so the Silicon substrate is on top.

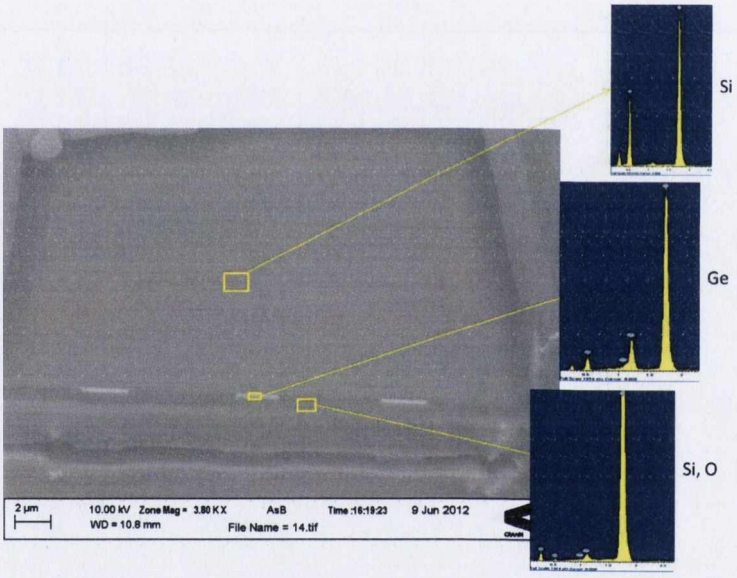

Figure 6.24 – Backscattered electrons showing the distribution of elements throughout the sample.

layer and Silicon dioxide layer.

The SEM system also contained an Energy Dispersive X-Ray (EDX) which confirmed the previous result. An EDX stimulates the emission of characteristic X-rays from a specimen, a high-energy beam of charged particles such as electrons or protons, or a beam of X-rays, is focused into the sample being studied. At rest, an atom within the sample contains ground

state electrons in discrete energy levels or electron shells bound to the nucleus. The incident beam may excite an electron in an inner shell, ejecting it from the shell while creating an electron hole where the electron was. An electron from an outer, higher-energy shell then fills the hole, and the difference in energy between the higher-energy shell and the lower energy shell may be released in the form of an X-ray. The number and energy of the X-rays emitted from a specimen can be measured by an energy-dispersive spectrometer. As the energy of the X-rays are characteristic of the difference in energy between the two shells, and of the atomic structure of the element from which they were emitted, this allows the elemental composition of the specimen to be measured. The results of the EDX measurements are shown in Fig. 6.25

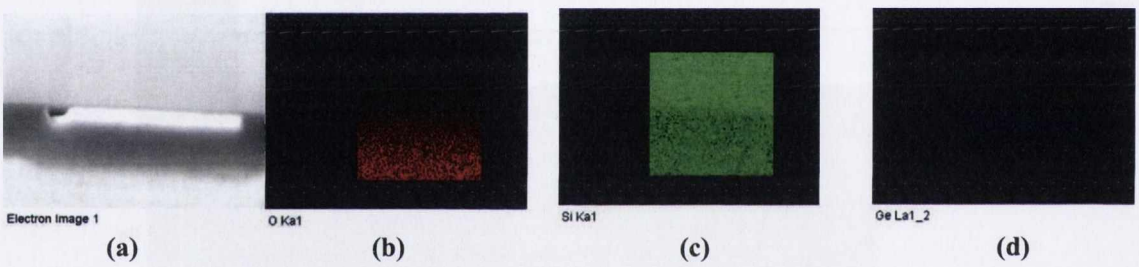

Figure 6.25 – Energy Dispersive X-Ray. The microgaph of the Germanium finger (a) with the EDX results showing the Oxygen (b), Silicon (c) and Germanium (d) distributions

6.5 Analysis of Sapphire Substrate

It has been suggested that the lateral crystallization is driven by either Silicon concentration gradient [71] or thermal gradient from the seed window [76] or a combination of both [76, 77]. In the case of the thermal gradient, the seed window provides a heat sink during temperature ramp down at the end of the RTA. This causes the Germanium close to the seed to solidify first and crystallization progresses along the stripe. In the Silicon gradient case, the higher Silicon content at the seed results in a higher melting point and again on cooling

this region solidifies first. To explore the driving mechanism the micro-crucible was fabricated on a sapphire substrate, producing a structure with no source of Silicon. A 50nm Silicon dioxide layer was deposited on the sapphire using PECVD and patterned to make a seed window. A 170nm thick PVD Germanium layer is deposited covering the seed area and Silicon dioxide and then patterned into narrow stripes. 1μm PECVD oxide and 1μm polysilicon layers were deposited on Germanium to act as the capping layer. After RTA at 985 °C, the capping layer was removed and Raman spectroscopy was used to investigate the crystalline quality. As expected no SiGe or Silicon peaks were present. The Ge-Ge peak shown in figure 6.26 has a FWHM value of ~6.4 cm^{-1} as well as asymmetry from low-frequency side of spectra, indicating that the Germanium stripe has polycrystalline structure with some amorphous content. This suggests that the presence of Silicon is necessary for optimum crystalline quality of the Ge stripe. It was also found that the sapphire substrate provides less tensile stress (as negligible shift in peak position is observed). This is due to the thermal expansion coefficient of sapphire being more closely matched to that of Germanium.

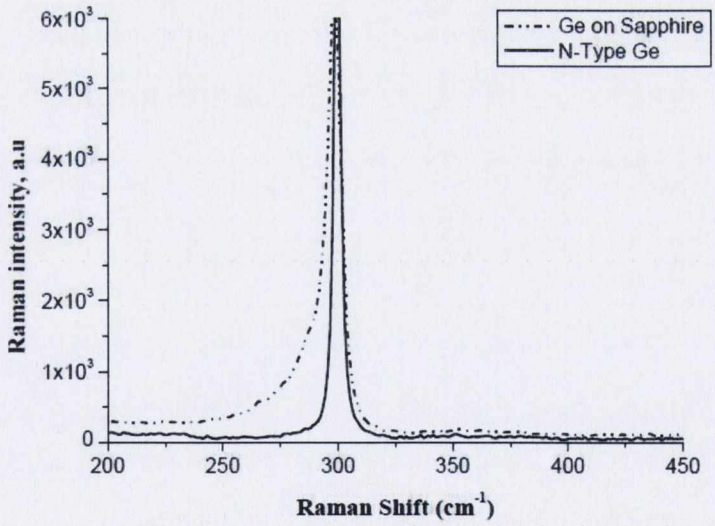

Figure 6.26 – Raman spectra of Germanium on sapphire substrate (dashed line) and the n-type Germanium wafer reference.

6.6 Conclusion

Results show that good quality Germanium stripes can be obtained from the rapid melt growth process. The TEM and SEM results confirmed that the crystalline quality of the Germanium stripes was high with a limited numbers of defects. In conjunction with the Raman analysis this shows that the rapid melt growth process can produce good quality Germanium stripes.

The PECVD oxide capping alone is not rigid enough to hold the molten Germanium resulting in cracks and delamination. Reinforcing the crucible with a polysilicon cap on top of the PECVD oxide provides robust capping layers and prevents balling and delamination.

An annealing temperature higher than 942 °C provides a better crystalline quality of PVD deposited Germanium films. This is confirmed by the uniformity of the Raman peak position and FWHM. The 170nm thick stripes were found to have a higher stress on average and were significantly more likely to suffer degradation. The 210nm thick stripes tended to have a slightly higher FWHM than the 170nm samples indicating that the decreased crystallinity is most likely due to the larger mass of Germanium that is required to undergo crystallisation. Annealing temperatures above 980 °C tended to produce stripes with uniform crystallinity for both 170nm and 210nm thick samples.

In contrast to samples with CVD Germanium, no SiGe spectrum was traced for PVD samples even when annealing at high temperatures ($\geq$ 1000 °C). This proves that the intermixing of Silicon and Germanium is due to the thin Silicon layer deposited prior to the Germanium in the CVD process and not because of the diffusion of Silicon from the seed window. CVD samples demonstrate less uniform Raman spectra with degradation of Germanium crystal quality when annealing at higher temperature ($\geq$ 1000 °C) in contrast to PVD films.

In the absence of a Silicon seed, which was the case for samples on sapphire substrate, a lower quality Germanium crystal structure (polycrystalline with some amorphisation) was observed. The Silicon seed window is therefore an important mechanism in process resulting to greater crystallinity.

Chapter 7

Piezoelectric materials

7.1 Introduction

Piezoelectric materials are suitable for a wide range of applications such as transducers, actuators, and sensors. The operating temperature range of the piezoelectric materials for these applications is determined by the Curie point [78]. The Curie point is the temperature above which the unit cell of piezoelectric compounds transforms from asymmetric tetragonal or rhombohedral arrangement to symmetric cubic arrangement; this renders them non-piezoelectric [78, 79]. The determination of the Curie point can be carried out using electrical measurements of changes in the dielectric properties of materials. Kalinin and co-workers have reported an electric field induced first order transformations in oxide thin films [80]. However, techniques that can determine temperature dependent changes in crystal structure shed more scientific insight into transformations, and also enable accurate evaluation of the Curie point of materials and hysteresis in recovery of asymmetric piezoelectric crystal states. Probing crystal structure transformations by Raman spectroscopy has been shown to be suitable for the determination of the Curie point for ceramics [81]. There has been first determination of phase transformation temperatures for thin films using in situ measurements [82]. The determination of the Curie point proved to be indicated the need for further studies to improve understanding of Raman peak assignments for complex perovskite

oxides such as the strongly Piezoelectric ABO_3-type Lead Zirconate Titanate (PZT). PZT is the most popular piezoelectric material given its large piezoelectric response and wide operating temperature range [78, 83]. The addition of Strontium as an *A*-site has been shown to enhance the piezoelectric response [84], but is expected to decrease the Curie point of the resulting material composition. The Curie point for these thin films of Sr-doped PZT (PSZT) with composition $(Pb_{0.92}Sr_{0.08})(Zr_{0.65}Ti_{0.35})O_3$ is expected to be around $250 - 280$ °C. The Curie point induced transformations are considered to be reversible with temperature [78, 79]. This chapter aimed to study the phase transformations in rhombohedral *c*-axis oriented thin films with increase in temperature, determine the thin film Curie point, and to check the reversibility of the same with controlled or uncontrolled cooling of the thin films using Raman spectroscopy.

7.2 Sample Fabrication and Characterisation

Silicon (100) samples were dipped in buffered hydrofluoric acid to remove the native oxide. These were subsequently coated with 200nm of Platinum, with a 20 nm Titanium dioxide adhesion layer; both layers deposited by electron beam evaporation. The use of the Titanium dioxide adhesion layer in place of Titanium was to significantly enhance the rhombohedral *c*-axis texture of the PSZT thin films [82, 85].

PSZT thin films were deposited by RF magnetron sputtering under conditions listed in Table 7.1. The deposition of PSZT thin films was carried out at 650 °C and at a process pressure of 10 mTorr which resulted in the optimal thin films composition, without lead/oxygen excess or deficiency. Deposition was carried out for 2 hours and the resulting PSZT thin films were 700nm thick. These 700 nm thick films were preferentially *c*-axis oriented with rhombohedral structure, as verified by X-ray diffraction (XRD) and transmission electron microscopy (TEM) [85]. Raman spectra were collected under 514nm excitation wavelength using the Ar+ laser with a power of 20mW. The Raman spectromemter was combined with a Linkam hot-stage that allowed very accurate thermal control (± 0.5°C accuracy) of the sam-

ples ranging from room temperature to 350 °C. An accumulation time of ten seconds was used and the data averaged over 10 accumulations. The spectra were taken through a quartz observation window in the Linkam stage.

Table 7.1 – PSZT thin film deposition conditions, [86].

Target	$(Pb_{0.92}Sr_{0.08})(Zr_{0.65}Ti_{0.35})O_3$
Target Diameter	100mm
RF Power	100 W
Target to substrate distance	70mm
Process Gas	10% Oxygen in Argon
Base Pressure	9.0×10^{-6} Torr
Sputtering Pressure	1.0×10^{-2} Torr
Substrate Temperature	650 °C
Temperature ramp-up rate	10 °C/min
Temperature ramp-down rate	5 °C/min
Sputtering duration	2 hr

In order to determine the Curie point, PSZT thin film samples were heated with a controlled ramp rate of 10 °C min^{-1}. Heating was carried out to a maximum of 350 °C, based on the estimate of the Curie point being ~280 °C. The sample was held at maximum temperature for 20 minutes. The sample was then cooled with controlled ramp-down (10 °C min^{-1}) until 100 °C, beyond which the cooling occurred more gradually towards room temperature. During heating and cooling each sample was maintained at the measurement temperature for two minutes in order to reach steady state conditions. Micro-Raman measurements were collected at selected set points, during the heating and cooling cycle and twice at maximum temperature, during which the temperature was held constant for 8 minutes for this purpose.

7.3 Results and Discussion

The investigated PSZT thin films (with Zirconium-Titanium ratio of 65/35) are in the rhombohedral phase at room temperature. Room temperature spectra demonstrates two main Raman bands at ~575 and ~744 cm^{-1}, as shown in Fig. 7.3. These two bands have been reported in earlier Raman investigations of PZT powders and thin films, in Ref. [87]. On heating the PSZT thin films, these bands decrease in intensity, which can be attributed to

increased scattering. These two bands are asymmetric, with a few pronounced sub-peaks visible at room temperature. To isolate the constituent peaks, these bands were fitted with a set of Gaussian/Lorentzian peaks. The band at ~575 cm^{-1} was fitted with three sub-bands located at 565, 575, and 604 cm^{-1}. The broad band centred at ~744 cm^{-1} was also fitted with three sub-bands positioned at 725, 744, and 766 cm^{-1}. In addition a small shoulder is observed at ~815 cm^{-1}. An example of the deconvolution at room temperature is shown in Fig. 7.1 and Fig. 7.2.

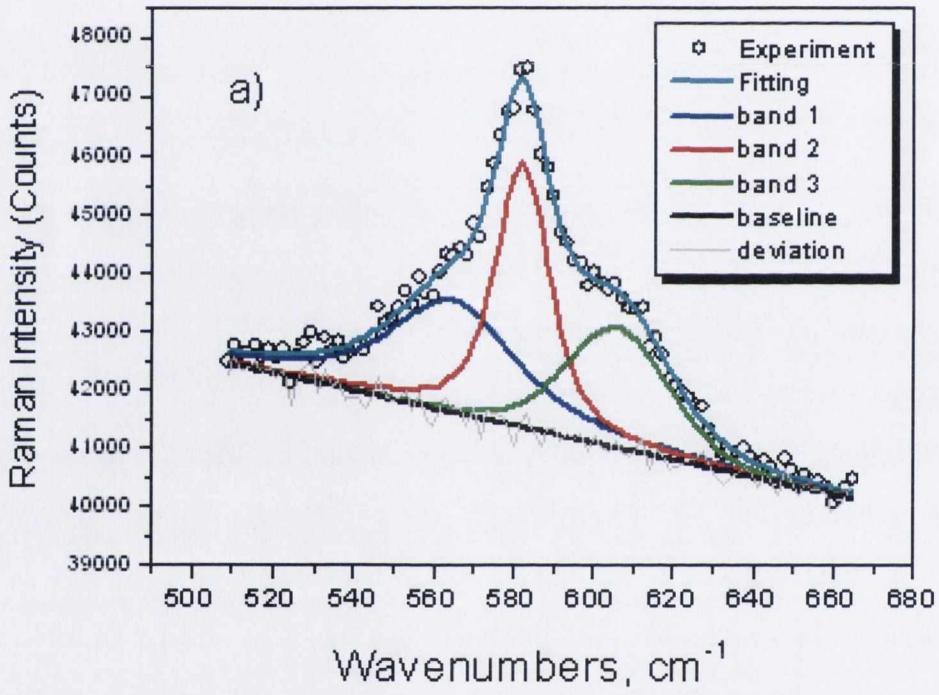

Figure 7.1 – Deconvolution of Raman peak of PSZT thin film between 500 and 680 cm^{-1} at T=25 °C into three individual components.

The position of some of these peaks is quite close to that obtained after the deconvolution of the two wide bands observed in the region from 450-620 cm^{-1} and 620-900 cm^{-1} for poled polycrystalline composites based on PZT [88].

It should be noted that our deconvolution produced three peaks for the ~744 cm^{-1} band, with only two previously reported. This can be attributed to the more pronounced sub-bands

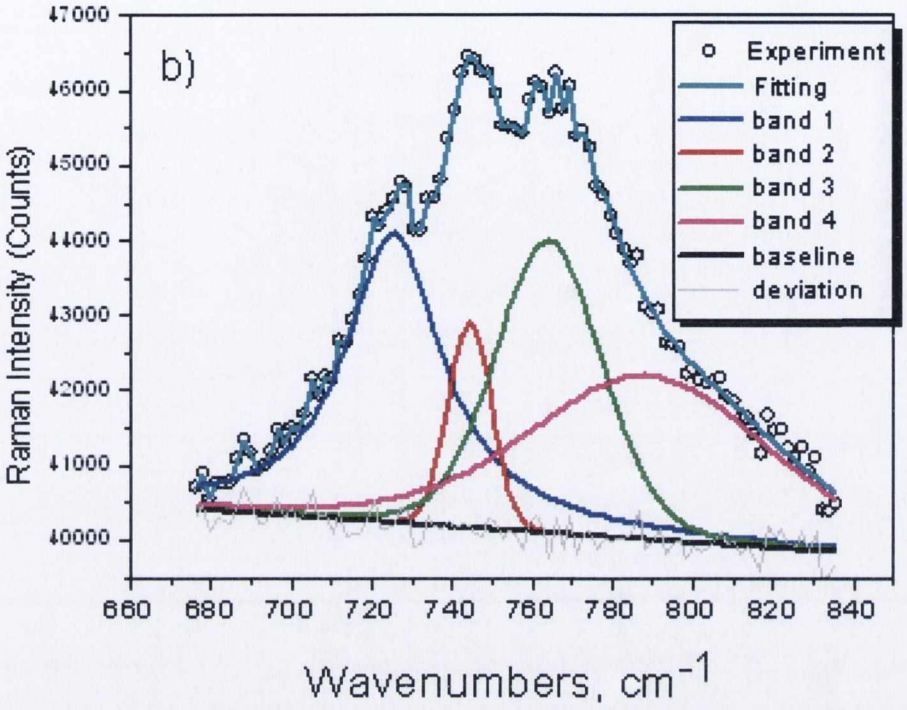

Figure 7.2 – Deconvolution of Raman peak of PSZT thin film between 680 and 840 cm^{-1} at T=25 °C into three individual components, a fourth overlapping shoulder is also included.

in our spectra as a result of the preferentially textured polycrystalline crystallography of PSZT thin films grown under optimised conditions; whereas, the sub-bands in published literature were not as pronounced [88, 89]. The stronger spectral contribution from the preferentially oriented PSZT, verified by XRD and TEM results [85], can also be confirmed from the results obtained by Foster et al. [90], where the Raman spectra of the oblique phonons of single-domain single crystal $PbTiO_3$ were demonstrated. These results show that a large number of different phonon modes can be observed at room temperature (20 °C) in the region from 420-800 cm^{-1} in platelet geometry for various directions of the phonon wave vector **k** for the $PbTiO_3$ crystal. Having established the constituent peaks in the spectra, the temperature dependence of different phonon modes obtained after fitting of the two wide bands described above were analysed. A comparison of the intensity ratios of the two peaks provides accurate evidence of phase transformations. As can be observed in Fig. 7.4, the

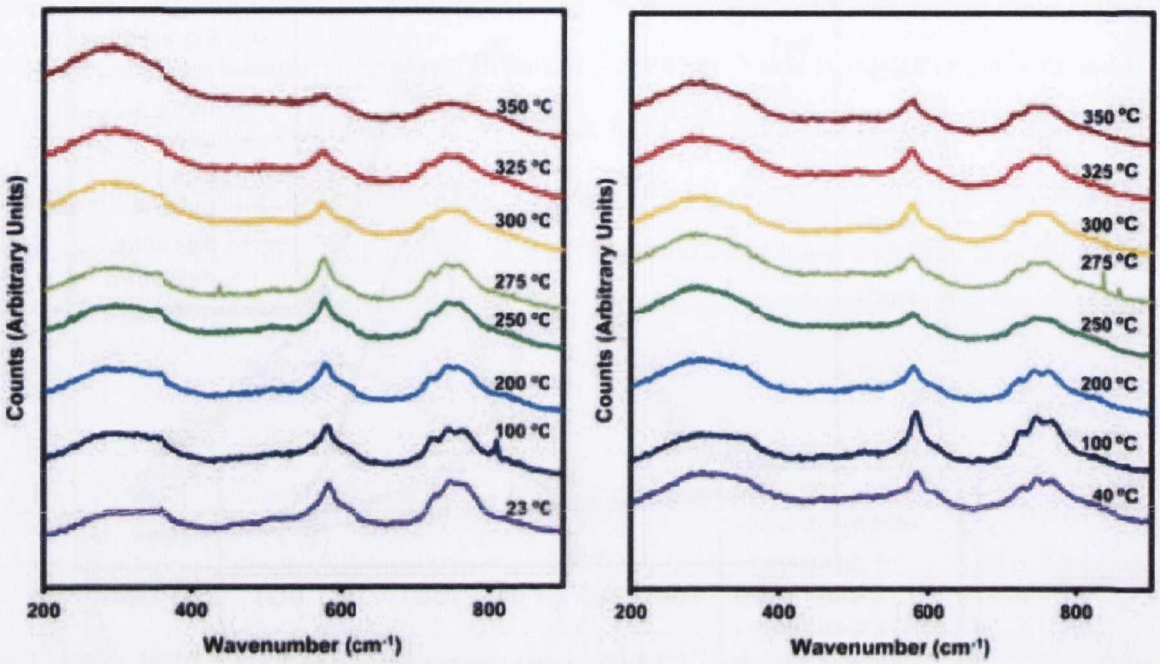

(a) Heating (b) Cooling

Figure 7.3 – Raman spectra registered *in situ* on (a) heating a PSZT thin film sample to 350 °C and (b) cooling the PSZT thin film sample from 350 °C. All spectra collected at 514nm excitation wavelength are presented on the same scale offset with respect to each other to enable comparison.

intensity ratio of the 744 and 575 cm^{-1} peaks increases at higher temperatures, following an apparent change at 275 °C.

The sharp intensity ratio variations signify phase transformation, starting at the theoretically expected value of ~280 °C. This phase transition observed can be related to the crystal structure of the thin film. The 575 cm^{-1} peak corresponds to the rhombohedral phase with a phonon mode of A1(3TO) [86, 87]. The 744 cm^{-1} peak is a combination of the rhombohedral A1(3TO) and cubic E(3LO) phonon mode [86, 87]. As a consequence of this, while both peaks should appear at room temperature (for rhombohedral structure), on heating the E(3LO) should dominate [86]. This should result in an increased intensity ratio of the 744 and 575 cm^{-1} peaks, as seen in Fig. 7.4. With controlled cooling at 10 °C /min, the cubic phase reverses back to the rhombohedral phase in the same temperature window of 275-

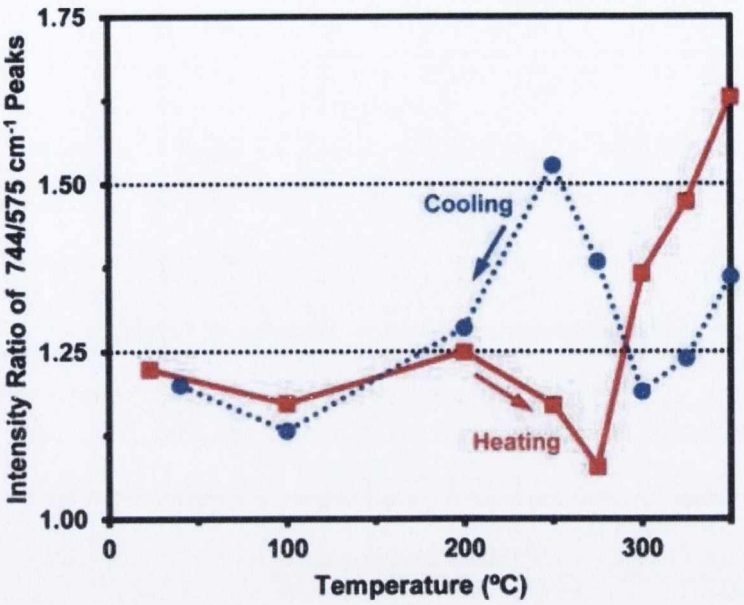

Figure 7.4 – Variation in the ratio of the intensities of the 744 and 575 cm^{-1} peaks with temperature during controlled heating and controlled cooling of the PSZT sample.

300 °C, indicating minimal hysteresis in the Curie point phase transformation. This reversal occurs with the peak intensity ratio returning to ~1.2.

In addition to the intensity ratios, the position changes with temperature for the two main peaks were also studied, as this highlights changes in bond lengths corresponding to crystal structure. These results for the ~575 and ~744 cm^{-1} peaks are presented in Fig. 7.5.

After accounting for shifts related to thermal expansion, clear features of phase transformation can be observed. For the ~575 cm^{-1} peak in Fig. 7.5(a), the peak position gradually decreases from 582 cm^{-1} (at 23 °C) on heating. A sharp change in the slope of the position variation occurs beyond 250 °C, corresponding to the intensity ratio changes in Fig. 7.4. However, the peak position behaviour is not as sharp as the peak intensity shown in Fig. 7.4 due to the fact that normally the peak intensity is more sensitive to the local change in the structure. The ~744 cm^{-1} peak showed similar behaviour during heating as seen in Fig. 7.5(b). On cooling, reversal in peak positions of both peaks was observed (Fig. 7.5), with a hysteresis behaviour present.

The Curie point phase reversal is a critical contributor to high temperature deposition of

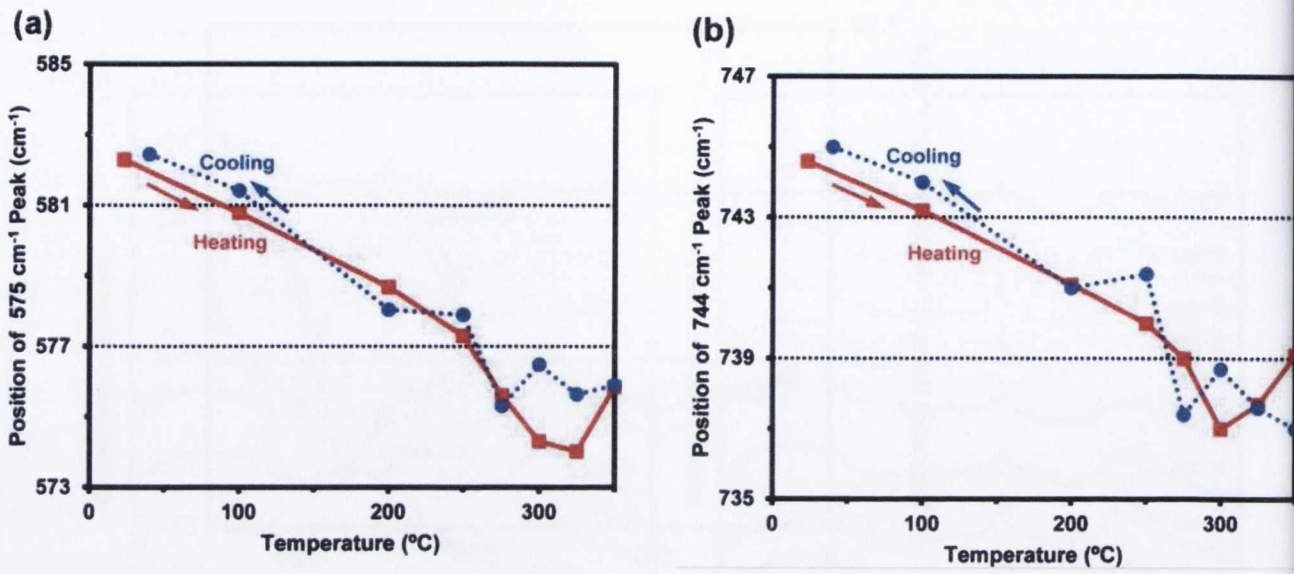

Figure 7.5 – Variation in the position of the (a) 575 and (b) 744 cm^{-1} peaks during controlled heating and controlled cooling of the PSZT sample.

piezoelectric thin films. Post-deposition cooling rate is known to greatly influence the final crystal structure of the piezoelectric materials, with slower cooling producing best results (at $\sim$5 °C min^{-1}) [83, 86]. Some hypothesise, in a principally intuitive manner, that this is due to temperature-driven crystallisation given the larger duration available for crystallisation [83]. This theory can be tested by rapid cooling of a known rhombohedral film. We carried out this investigation, using a fully characterised film, as discussed in the earlier sections of this work. The temperature of the PSZT thin films was allowed to ramp up slowly to enable phase transformations, following which the effect of uncontrolled cooling on these films was studied. For the initial experiments to determine the Curie point, PSZT thin film samples were heated up to 350 °C at a controlled rate of 10 °C/min and cooled at the same rate. Micro-Raman spectra were collected at regular temperature intervals, under the conditions described above. The complete collection of the spectra recorded during the heating and cooling processes are shown in Fig. 7.3.

The expected Curie point transformation was observed beyond 275 °C. From the maximum temperature of 350 °C, the sample was cooled naturally. The behaviour of the 575 and 744 cm^{-1} PSZT micro-Raman peaks was studied in detail, with changes in intensity and

position of the 575 cm^{-1} peak shown in Fig. 7.6.

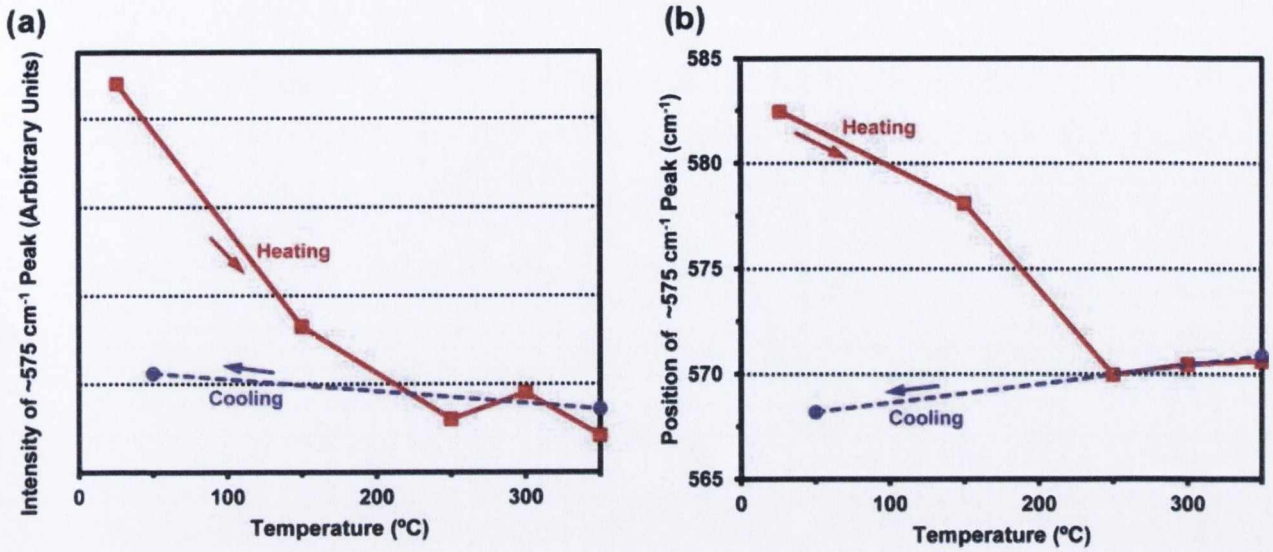

Figure 7.6 – Intensity and position variations of the 575 cm^{-1} peak during controlled heating and uncontrolled cooling are shown in (a) and (b), respectively.

The behaviour of composite peak areas is similar to that of the earlier experiment during the controlled ramp-up of temperature. However, on rapid cooling of the sample, the peak intensities and positions remain locked in the cubic phase, indicating a permanent phase change has occurred (Fig. 7.6(b)). Evidence of this pinning to the cubic phase is provided by the observation of invariance in peak heights for the cooling measurements at 350 °C and 50 °C, and by identical full range micro-Raman spectra as shown in Fig. 7.7.

The absence of any relaxation to the room temperature rhombohedral phase was verified by a repeated measurement of these samples after a period of four days and observing the same high temperature cubic phases at room temperature, indicating that this phase change is permanent. This result shows that actual cooling rate induced phase lock-in dominates any crystallisation process for these thin films.

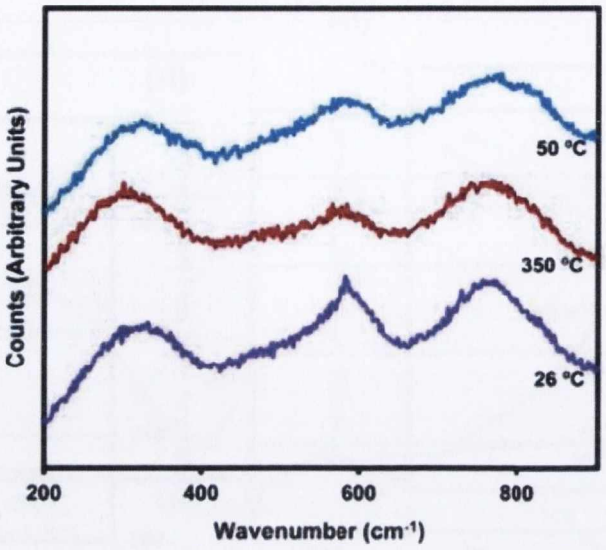

Figure 7.7 – Raman spectra collected at room temperature, after controlled heating to 350 °C and after uncontrolled cooling from 350 °C to 50 °C.

7.4 Conclusion

We have carried out in situ heating with micro-Raman spectroscopy to study the Curie point induced phase transformation in piezoelectric PSZT thin films. We have identified that Curie point transformation for these room temperature rhombohedral films occurs at 275 °C and is a reversible process with minimum hysteresis. The significance of the rate of cooling post-deposition on reversal of Curie point transformations was studied. The results show that this can strongly disrupt Curie point transformations, by pinning the material to the high temperature cubic phase, if the cooling process is rapid and uncontrolled.

Chapter 8

Silicides

8.1 Introduction

Thin films of polycrystalline Silicon, or polysilicon (also known as poly-Si or poly), are widely used as MOS transistor gate electrodes and for interconnection in MOS circuits. The electrical conductivity of a polysilicon gate may be increased by depositing a metal (such as Tungsten) or a metal silicide (such as Tungsten silicide) over the polysilicon. This creates a silicide, an alloy of a metal and Silicon. Refractory metal silicides exhibit properties that make them prime candidates for replacing doped polysilicon where low resistivity is required. Given the right stoichiometry, they are stable up to high temperatures, show good adhesion and also a good dry etchability [46]. Tungsten Silicide is used for interconnection applications because of the high conductivity, thermal stability of its teragonal phase [91, 92] and improved device performance in terms of RC time delay and power consumption [93].

Silicides can be prepared in two different ways. Pure metal can either be deposited on Silicon and transformed into a silicide via thermal annealing or alternatively, metal and Silicon can be co-deposited, which immediately leads to a silicide layer. The latter process is generally preferred since it leads to lower mechanical stress and a smoother silicide-Silicon interface [94]. While Silicon-rich WSi_x-films ($x > 2.3$) exhibit smooth film-to-substrate interface [95], they are thermally unstable and segregate the excess Silicon as Silicon crystallites

or increase the thickness of the underlying polysilicon [96]. Tungsten-rich films (x <2.0), on the other hand, are also thermally unstable and lead to the consumption of the underlying polysilicon layer during anneal steps later in the process [97].

Silicon on Insulator, SOI, technology is emerging for application in advanced digital CMOS circuits, advanced analogue bipolar transistor circuits, and in novel power device structures. Silicon-on-silicide-on-insulator (SSOI) [72] is a novel variant which can provide a low resistance buried collector contact for bipolar transistors. Tungsten silicide (WSi) is an ideal buried metallic layer as it is a refractory material that offers low sheet resistance (typically 20Ω/□ for a 200-nm layer) and excellent thermal stability. The basic structure of a bipolar transistor manufactured with this technology is shown in Fig. 8.1 [98].

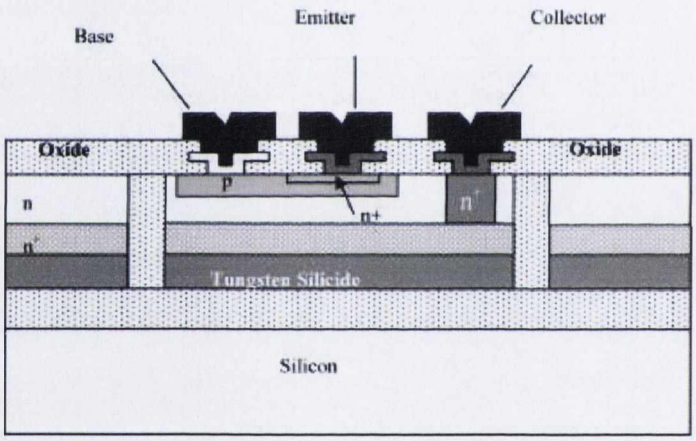

Figure 8.1 – Silicon-on-silicide-on-insulator (SSOI) transistor consisting of a bipolar transistor fabricated on SOI incorporating a buried Tungsten silicide conduction layer.

The silicide requires a shallow diffused layer to make it ohmic to the collector due to the Schottky effect. The silicide layer reduces the collector parasitic resistance by a factor of 10–100 compared to standard buried *n* and *p* implant technology and the overall thickness of Silicon can be greatly reduced [98]. A number of studies concerning the diffusion of dopant species such as Boron and Phosphorus in WSi have been published [98, 99]. This has largely been to investigate the influence of lateral diffusion of these species on threshold voltage stability in MOS transistors. The diffusivity of these dopants in WSi was reported

to be approximately 100 000 times greater than that in polycrystalline Silicon as shown in Fig. 8.2 [99]. A potential application of this is advocated for SSOI where the dopant species would be implanted into the buried silicide at a remote site as a back-end process. A low thermal budget process would diffuse the dopants through the silicide and up into the overlying active Silicon layer. This approach greatly simplifies the production of the bipolar transistors and minimizes disturbance of the emitter/base doping profiles caused by thermal annealing.

Production of complementary bipolar devices with tightly matched properties, low-loss microwave diodes, and smart power ICs with vertical DMOS can also be achieved.

Raman Spectroscopy is used in an attempt to determine the extent of dopant diffusion along Tungsten Silicide samples. Tungsten Silicide has two Raman peaks at 456 and 335cm^{-1}[100, 101]. However no work in the literature has been found to determine the doping concentration of WSi using Raman spectroscopy. The investigation of dopant diffusion in WSi_x layers was conducted in collaboration with The Northern Ireland Semiconductor Research Centre, The Queen's University Belfast.

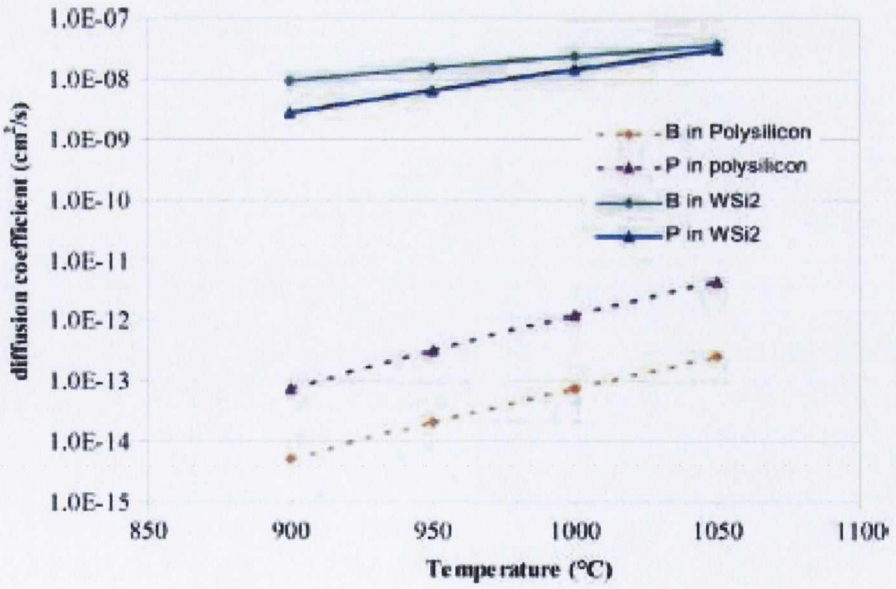

Figure 8.2 – Diffusion coefficient of Phosphorus and Boron in WSi and polycrystalline Silicon.

8.2 Manufacturing Process

Amorphous, Silicon rich WSi_x was deposited by chemical vapour deposition, using WF_6 - SiH_4 chemistry (WF_6 - 3sccm, SiH_4 - 200sccm, Ar - 550sccm, 370°C and 300m Torr, producing a deposition rate of $9Ås^{-1}$). In addition, as the deposited layer is Si rich, no Si is required from the substrate to form WSi_2, hence deposition can be performed on oxidised Silicon substrates for comparison.

Substrate contact windows (30x30m) were patterned in a thermally grown 0.45-m oxide layer. A 0.15-m Tungsten silicide layer was then deposited by LPCVD and patterned. The substrate was then coated with a 0.6-m LPCVD tetraethylorthosilicate (TEOS) oxide deposited at 720 C. The WSi_2 phase was formed by annealing at 1050 °C for 2 hours. This anneal also simulated the bond strengthening anneal normally employed when the silicide is incorporated in an SOI structure. Implant windows were patterned and either Boron or Phosphorus was implanted with energy 55 and 75 keV, respectively. A dose of $5x10^{15}$ cm^{-2} was employed for both dopants. Dopant was subsequently diffused along the conduits by annealing for 30 min at 900 C or at 1000 C. Prior to the diffusion anneal, the silicide conduit structures were capped with a low temperature (720 °C) LPCVD TEOS layer. The purpose of this encapsulating layer was to prevent dopant evaporation from the large implant window during the diffusion anneal [102]. Following contact window formation, aluminium electrodes were formed to allow electrical contact to the diodes.

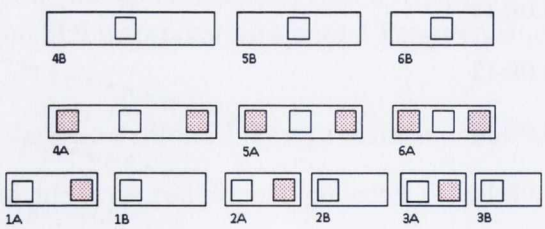

Figure 8.3 – A series of test structures results. 1A was examined in detail and the vast majority of Raman measurements were carried out on this structure. .

The as-deposited sheet resistance of the WSi_x is approximately $56\Omega/\square$. On annealing the sheet resistance decreases significantly due to structural change in the layer. As deposited

the layer is amorphous, the layer becomes a polycrystalline layer at ~400°C, as the anneal temperature increases the layer transforms to a tetragonal phase of crystalline WSi_x and the sheet resistance decreases significantly.

Fig. 8.4 shows the XRD analysis of silicide layers annealed in the 600-1000 °C, temperature range. From the XRD analysis it is clear that no further phase change occurs as the temperature increases from 600-1000 °C. Decrease in resistivity as the temperature increases is attributed to grain growth in the layer and the removal of excess Silicon from the layer. XRD analysis confirms grain growth as the peaks clearly become more defined at higher temperatures.

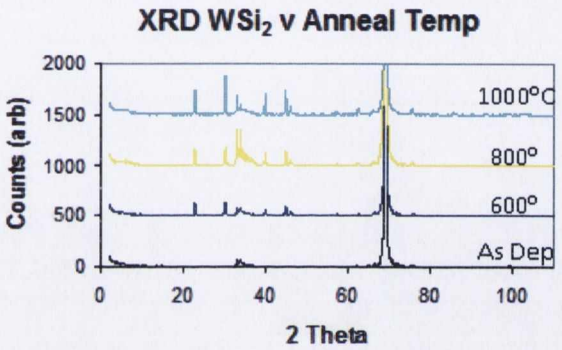

Figure 8.4 – XRD analysis of silicide layers annealed in the 600 - 1000 °C temperature range.

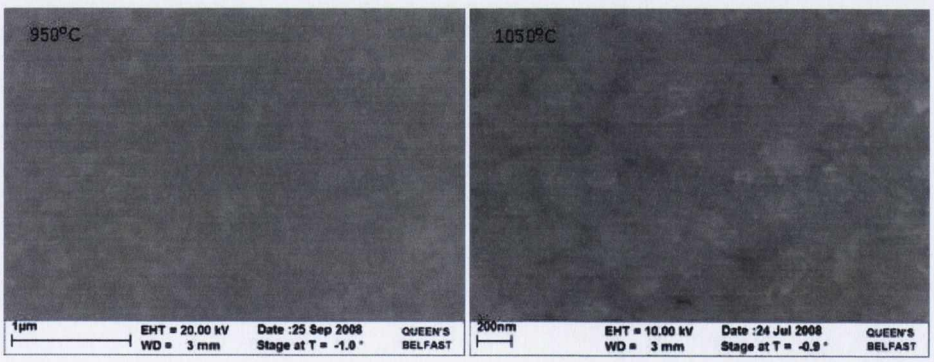

Figure 8.5 – SEM analysis of the surface of the silicide layer confirms that as the anneal temperature increases grain growth increases.

In order to allow Raman analysis the top layer of oxide over the structures were removed

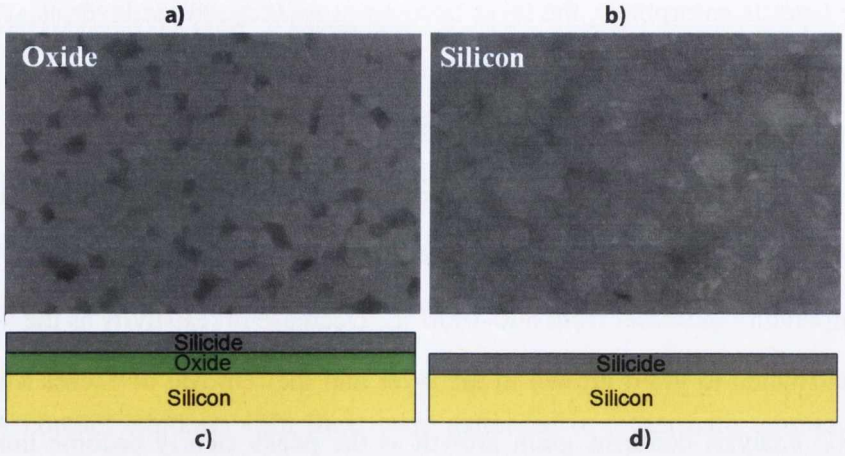

Figure 8.6 – SEM images of post anneal silicide over oxide (a) and Silicon (b) on an undoped sample. The cross section schematic is shown in (c) and (d).

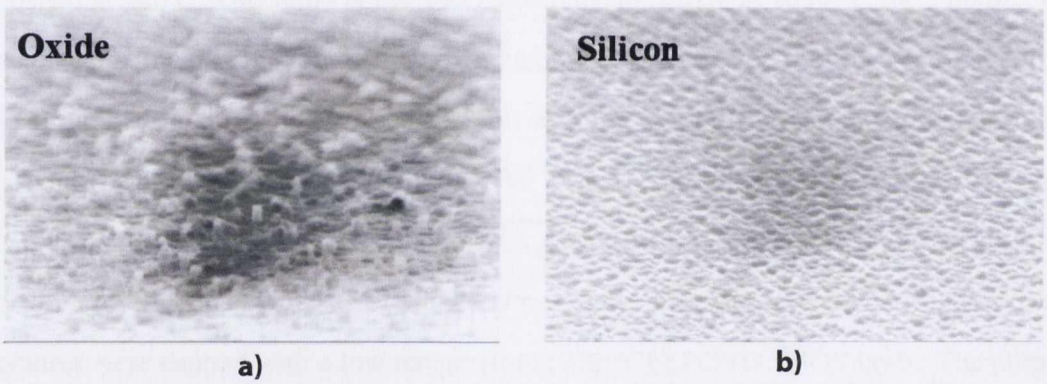

Figure 8.7 – SEM images of oxide (a) and Silicon (b) surface after selective removal of undoped WSi. Silicon tends to diffuse into WSi and oxide forms grains shown in Fig. 8.6.

using a chemical etch as shown in Figs 8.8 and 8.9.

A $5x10^{15}$ cm^{-2} Phosphorous implant was performed using the window in the oxide as a mask. Device 1A received the implant dose, device 1B was a control structure and receives no implant. The substrate was then heated to 900 °C for 30mins, resulting in P diffusion along the WSi_2 layer. The dopant diffusion produces a diode structure in the Silicon/silicide interface. Test structures 1A and 1B look identical, as the oxide has been removed as shown in Fig. 8.9.

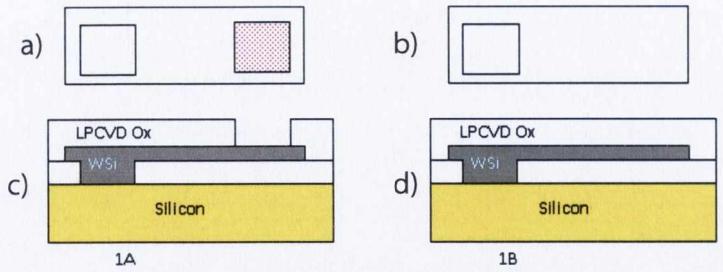

Figure 8.8 – Top and cross sectional view of test structure including top layer of deposited oxide. Sample (a) has a window allowing dopant diffusion, sample (b) is undoped.

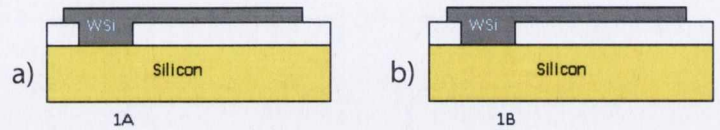

Figure 8.9 – Cross sectional view of test structure (a) with dopant and (b) without. The top layer of deposited oxide has been removed.

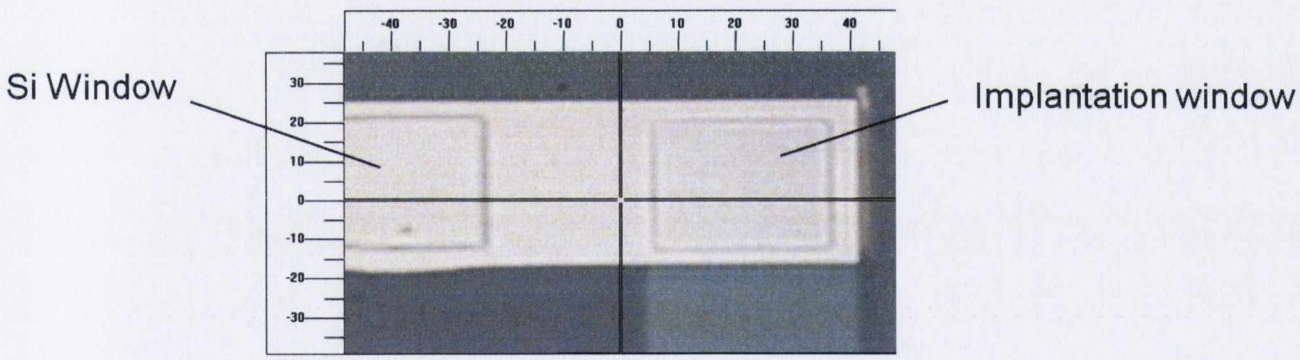

Figure 8.10 – Optical microscope image of silicide structure under investigation.

8.3 Raman Measurements of Circular Silicide Structures

Initially circular silicide structures were examined. The Raman spectra of WSi_2 without implantation was compared to WSi_2 structures implanted with Phosphorous. Figs 8.11 and 8.12, show the resultant Raman spectrum. The difference in grain size and shape affect the

Raman spectra and the diffusivity of the silicide. Large Si grains appear in the WSi over oxide as shown in Fig. 8.6.

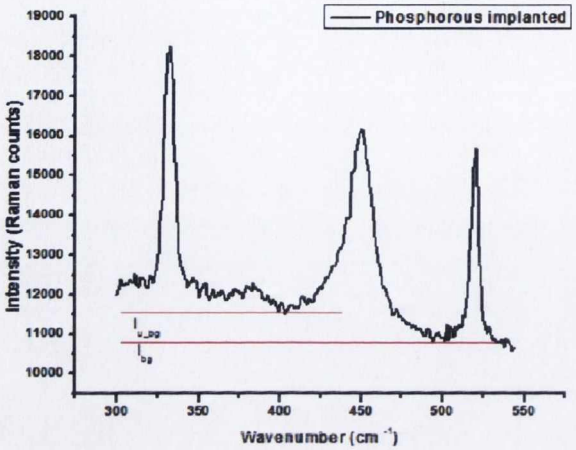

Figure 8.11 – Raman spectrum of a circular structure with Phosphorous implantation collected using 633nm laser. Peaks at 330 cm^{-1} and at 450 cm^{-1} indicate the presence of tetragonal WSi_2. The peak at 520 cm^{-1} indicates the presence of crystalline Si.

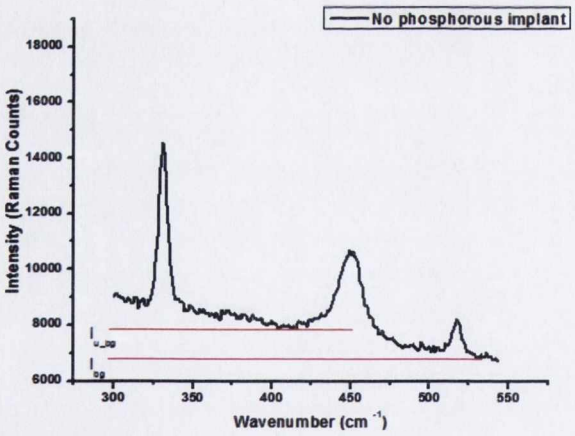

Figure 8.12 – Raman spectrum of circular structure without Phosphorous implant.

Crystalline WSi has a tetragonal structure with two active Raman modes at 456 cm^{-1} and 335.5 cm^{-1} [100] as shown in Figs. 8.11 and 8.12.

Based on these results there appears to be a slight deviation between the relative intensities of the WSi peaks in the doped and undoped samples. It is possible that the samples become more transparent due to the doping as the Silicon peak intensity increases. This is most likely

Table 8.1 – Comparison parameters between the Phosphorous implanted structure and the structure without doping.

	Doped (wP)	Undoped (noP)	Change (wP - noP)	% Change
450cm^{-1} Intensity	4403	4047	356	-8.1
450cm^{-1} Width	19.28	17.92	1.36	-7.1
450cm^{-1} Position	449.46	449.37	0.092	negligable
330cm^{-1} Intensity	5927	5017	910	-15.4
330cm^{-1} Width	6.99	6.87	0.12	-1.7
330cm^{-1} Position	331.76	330.86	0.9	-0.3

due to ion implantation damage and/or possible surface roughness.

8.4 Raman Measurements of Silicide Strips

Raman measurements using the 633nm excitation wavelength were conducted lengthwise along the prepared silicide strips. The results are shown in Fig. 8.13.

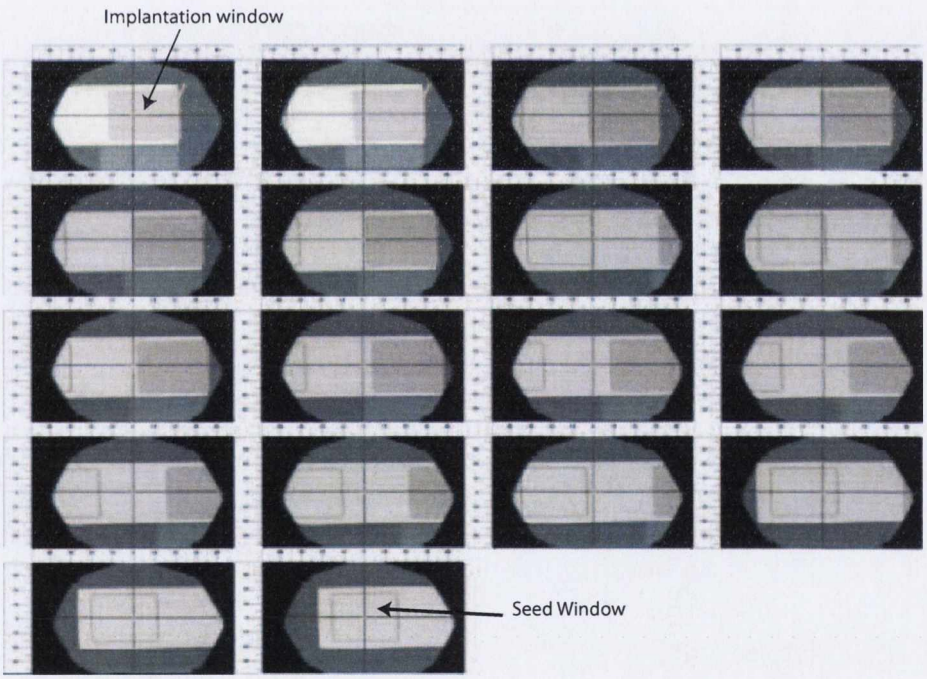

Figure 8.13 – Location of Raman measurements along the silicide structure.

The results of these measurements are shown in Fig. 8.14 for the 450 cm^{-1} peak. Significant changes can be seen in the Raman peak intensity and position, it is possible that the high

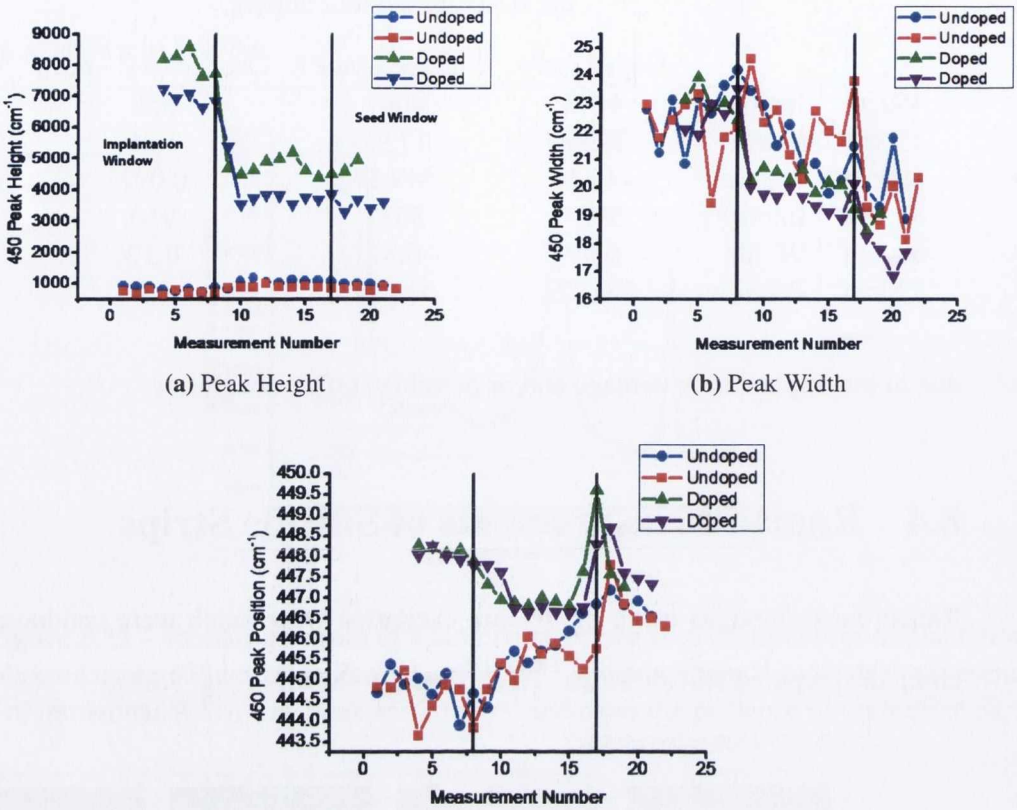

(a) Peak Height

(b) Peak Width

(c) Peak Position

Figure 8.14 – Fitting results from the 450 cm^{-1} peak. The vertical lines indicate the seed and implantation windows. Two different measurements are shown.

stress in the doped structure indicated by the higher peak position [46] may be an indicator of induced stress due to implantation in the crystalline silicide. The mechanism leading to the large divergence between the doped and undoped results and sharp transition of the 450 cm^{-1} peak height are uncertain, but most probably due to ion implantation damage.

8.5 Conclusion

Although differences in the grain structure of the Phosphorous diffused silicide grown over the oxide and Si, are not as pronounced as the undoped silicide, they will have unpredictable effects on the Raman spectra. It was difficult to determine if the changes in the Raman spectra were due to the free carrier concentration however it is possible that the large stress in the

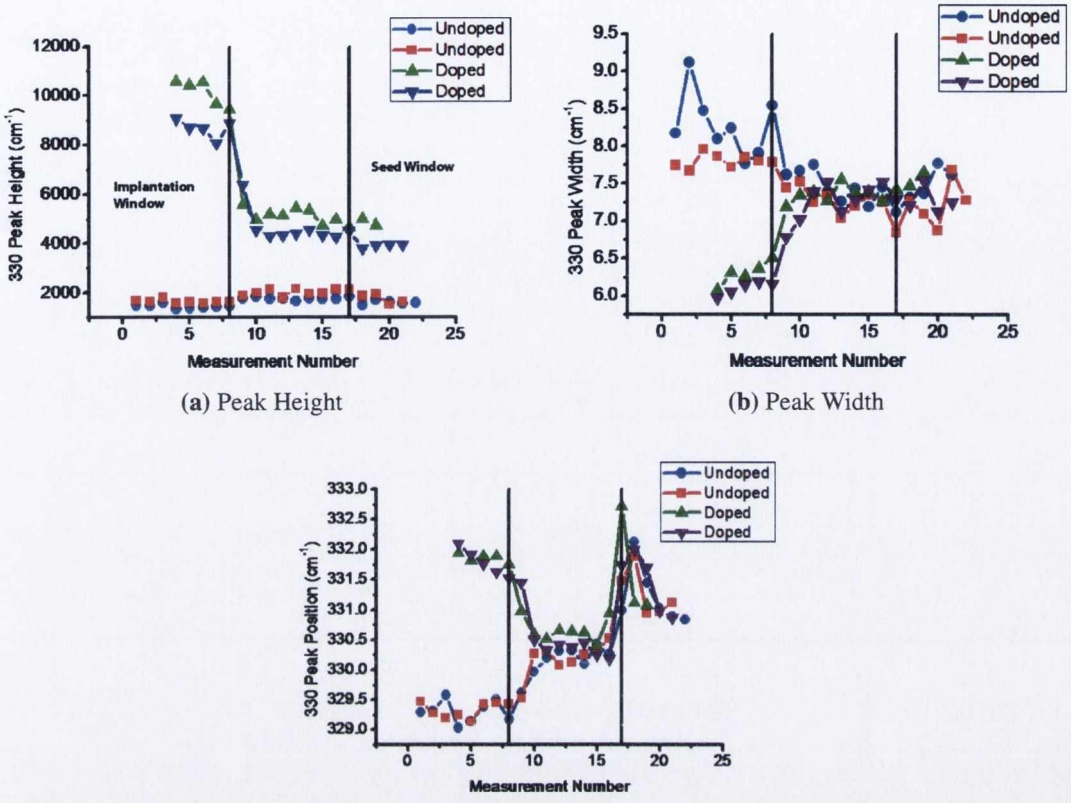

(a) Peak Height

(b) Peak Width

(c) Peak Position

Figure 8.15 – Fitting results from the 330 cm^{-1} peak.

doped structure indicated by the shift of the peak position to the higher frequency may be an indication of carrier induced stress in the crystalline silicide. Sharp discontinuities at the boundary lines are mainly due to stresses caused by the vertical transition in the topography of the structure. More detailed research into this subject are necessary in order to understand if Raman spectroscopy can be a useful tool in monitoring the diffusion process in WSi.

Chapter 9

Conclusion and Future Work

The usefulness of Raman spectroscopy, its non destructive nature, in situ measurements and minimal sample preparation were all demonstrated across a broad spectrum of materials each requiring a different method of analysis.

Through Silicon Vias

The application of Raman spectroscopy allowed detailed examination of the stress surrounding the through Silicon vias, supplied by XSiL. The results showed that the heat affected zone compares very favourably with results obtained in [48, 50] where a significant induced stress of up to 1.4 GPa and amorphization in single crystal Silicon (ranging up to $\sim$20%) was found. The stress values above 200MPa were always isolated occurrences possibly resulting from sample damage. Compressive stress in particular was very prevalent in the upper half of the vias sidewalls. No strong correlation between stress levels surrounding the via and via depth were found. The extent of the heat affected zone was measured to be approximately within a distance of 2-4 μm from the edge of the vias. Amorphous Silicon was not detected at the edge of the vias. This is contrary to recent results from [50] and [48] where a different drilling process for via fabrication was used. Based on these results the technique developed by XSiL had significant advantages over existing through Silicon vias formed by laser oblation. Raman spectroscopy has been shown to be a suitable technique to determine the quality

of through silicon vias produced with potential applications in an industrial environment.

Microcrystalline Silicon

The deposition technique developed by Phive Plasma Technologies to deposit microcrystalline Silicon over large areas was also examined. It is quite difficult to determine the crystallinity fraction of this material using existing techniques such as XRD and SEM. The application of several techniques including Raman spectroscopy and X-Ray Diffraction were investigated and successful attempts were made using chemometric analysis of the Raman data and polarisation filters to improve existing techniques used to determine the crystalline fraction.

The crystallinity fraction, determined from the Raman spectra of micro-crystalline Silicon, changed significantly depending on the penetration depth of the excitation wavelength used. This was expected as the crystalline regions grow in conical sections [61], the girth of which increases with distance from the substrate. Different wavelengths can therefore be used to determine the crystallinity at various depths. However this growth method also means that the micro-crystallinity and the resulting Raman spectra is not uniform but rather an average of the crystallinity within the Raman collection region.

Both the polarisation and chemometric techniques significantly attenuated the influence of the second order phonons and allowed for more accurate calculation of the crystallinity fraction within highly crystalline samples. The chemometric technique requires significantly shorter exposure time and could potentially be used to rapidly map regions of the sample under investigation. The XRD results were also carefully analysed and despite the importance given to the XRD results in [58], it was concluded that this was not a reliable fitting procedure. Chemometric analysis of this type although popular when studying biological samples has not been used nearly as extensively for semiconductor materials. Microcrystalline Silicon is an important material with many potential uses and correct characterisation of this material is very important.

Germanium Stripes

A novel fabrication technique in which deposited Germanium was rapidly annealed to produce single crystal Germanium from a Silicon seed was investigated to determine the quality of the Germanium. Germanium-on-insulator substrates are seen as a potential replacement for Silicon on miniaturized chips and can also be used as a substrate for high-efficiency photovoltaic cells. Results from a number of characterisation techniques showed that the rapid annealing of Germanium produced good quality crystalline Germanium in certain cases but that the structural integrity of the Germanium was weak.

Good quality Germanium stripes can be obtained from the rapid melt growth process. This is confirmed by the uniformity of the spectral parameters (the peak position and FWHM). The 170nm thick stripes were found to have a higher stress on average and were significantly more likely to suffer degradation. The 210nm thick stripes tended to have a slightly higher crystallinity than the 170nm samples indicating that the decreased crystallinity is most likely due to the larger mass of Germanium that undergoes crystallisation. Annealing temperatures above 980 °C tended to produce stripes with more uniform crystallinity for samples with 170nm and 210nm thicknesses.

The TEM and SEM results confirmed that the crystalline quality of the Germanium stripes was high with small numbers of defects (defect density $< 10^{16}$). Overall the results showed that the rapid melt growth Germanium was of good quality.

No SiGe peak was found for PVD samples even when annealing at high temperature ($\geq$ 1000 °C) however CVD deposited samples did show an SiGe peak. This proves that the intermixing of Silicon and Germanium is due to the thin Silicon layer deposited prior to the Germanium in the CVD process and not because of the diffusion of Silicon from the seed window.

In the absence of a Silicon seed, which was the case for samples on sapphire substrate, a lower quality Germanium crystal structure (polycrystalline with some amorphisation) was observed. Therefore the Silicon seed window is an important mechanism in the rapid melt process. The relatively inexpensive rapid melt process has been shown to produce crystalline

Germanium with crystallinity similar to the refernce Germanium wafer under certain conditions. Germanium produced in this manner could have many potential applications in future devices.

Piezoelectrics

Strontium doped lead Zirconate Titanate is a piezoelectric material sometimes called a smart material which is a material that has one or more properties that can be changed by external stimuli e.g. stress, temperature, moisture, pH electric or magnetic fields. The ferromagnetic properties of Strontium doped Zirconate Titanate were analysed for changes in its crystalline structure due to temperature changes.

Piezoelectric materials are used in a wide range of applications such as transducers, actuators and sensors. The range of temperatures within which the piezoelectric material can operate is determined by its Curie point and how the Curie point changes under varying temperature. In situ heating coupled with Raman spectroscopy was used to study the Curie point induced phase transformation in piezoelectric PSZT thin films. The Curie point transformation of these room temperature rhombohedral films occurs at 275 °C and is a reversible process with minimum hysteresis. The significance of the rate of cooling post-deposition on reversal of Curie point transformations was studied. The results show that this can strongly disrupt Curie point transformations, by pinning the material to the high temperature cubic phase, if the cooling process is rapid and uncontrolled.

Tungsten Silicide

In addition attempts were also made to determine dopant diffusion in Tungsten Silicide (WSi), using Raman characterisation. WSi is an ideal buried metallic layer as it is a refractory material that offers low sheet resistance and excellent thermal stability that has potential applications in transistor technology.

Although differences in the grain structure of the Phosphorous diffused silicide grown over the oxide and Silicon, are not as pronounced as the undoped silicide, they will have

unpredictable effects on the Raman spectra. It is possible that the large stress in the doped structure indicated by the shift of the peak position to the higher frequency may be an indication of carrier induced stress in the crystalline silicide. Sharp discontinuities at the boundary lines are mainly due to stresses caused by the vertical transition in the topography of the structure. More detailed investigation is required in order to further develop the analysis of the diffusion process in WSi.

The important materials characterised and analysed by Raman spectroscopy has and will contribute to advances in the semiconductor and solar cell industries.

9.1 Future Work

Composite semiconductor materials and semiconductor or piezoelectric materials comprised of different phases are used extensively in industry. The Raman analysis techniques described here could have many potential applications in this field especially if the techniques are further refined.

In the literature it has been discussed that free carrier concentration can be determined using second order plasmons potentially offering a way to further analyse the dopant diffusion in Tungsten silicide.

Raman spectroscopy has been used in several novel and interesting ways especially in relation to semiconductor materials. There is limited material available in book form on the Raman scattering of crystalline materials in comparison to that for molecular and biological systems ideally a book covering this important area would be written.

The preliminary investigations performed on WSi diffusion demonstrate the potential of using Raman mapping to monitor silicide diffusion. More work can be done in this area using Raman mapping along with EDX and SIMS measurements in the Silicon window in order to achieve a quantitative Raman analysis.

Bibliography

[1] D. Lon, *Raman Spectroscopy*. McGraw Hill, 1977.

[2] G. Turrell and J. Corset, *Raman Microscopy Developments and applications*. Academic Press, 1996.

[3] G. H. Loechelt, N. G. Cave, and J. Menendez, "Measuring the tensor nature of stress in Silicon using polarized off-axis Raman spectroscopy," *Applied Physics Letters*, vol. 66, p. 3630, 1995.

[4] N. Ashcroft and N. Mermin, *Solid State Physics*. Brooks Cole, 1979.

[5] Wikipedia, "Brillouin zone," 2012.

[6] P. Giannozzi, S. Baroni, and N. Bonini, "Quantum espresso: a modular and open-source software project for quantum simulations of materials," *Journal of Physics: Condensed Matter*, vol. 21, no. 39, p. 395502 (19pp), 2009.

[7] T. Inui, *Group Theory and Its Applications in Physics*. Springer, 1996.

[8] H. M. J. Smith, "The theory of the vibrations and the raman spectrum of the diamond lattice," *Philosophical Transactions of the Royal Society of London. Series A, Mathematical and Physical Sciences*, vol. 241, no. 829, pp. 105–145, 1948.

[9] R. Loudon, "Theory of the first-order raman effect in crystals," *Proceedings of the Royal Society of London. Series A, Mathematical and Physical Sciences*, vol. 275, no. 1361, pp. 218–232, 1963.

[10] C. Hamaguchi, *Basic Semiconductor Physics*. Springer, 2010.

[11] R. Brout, "Width and shift of spectral lines due to dissipative interaction," *Physical Review*, vol. 107, no. 3, pp. 664–668, 1957.

[12] A. Pinczuk and E. Burstein, "Fundamentals of inelastic light scattering in semiconductors and insulators," in *Light Scattering in Solids I*, Topics in Applied Physics, Springer Berlin / Heidelberg, 1983.

[13] L. van Hove, "Quantum-mechanical perturbations giving rise to a statistical transport equation," *Physica*, vol. 21, no. 1-5, pp. 517–540, 1954.

[14] R. Loudon, "The raman effect in crystals," *Advances in Physics*, vol. 50, no. 7 SPEC., pp. 813–864, 2001.

[15] P. Temple and C. Hathaway, "Multiphonon Raman Spectrum of Silicon," *Physical Review B*, vol. 7, no. 8, pp. 3685–3697, 1973.

[16] K. Uchinokura, T. Sekine, and E. Matsuura, "Critical-point analysis of the two-phonon Raman spectrum of Silicon," *Journal of Physics and Chemistry of Solids*, vol. 35, no. 2, pp. 171–180, 1974.

[17] R. Shuker and R. W. Gammon, "Raman-scattering selection-rule breaking and the density of states in amorphous materials," *Physical Review Letters*, vol. 25, no. 4, pp. 222–225, 1970.

[18] M. Brodsky, "Raman scattering in amorphous semiconductors," in *Light Scattering in Solids I*, Topics in Applied Physics, Springer Berlin / Heidelberg, 1983.

[19] J. E. Smith, M. H. Brodsky, B. L. Crowder, M. I. Nathan, and A. Pinczuk, "Raman spectra of amorphous si and related tetrahedrally bonded semiconductors," *Phys. Rev. Lett.*, vol. 26, pp. 642–646, Mar 1971.

[20] D. Weaire and R. Alben, "Phonon spectra of tetrahedrally bonded solids," *Phys. Rev. Lett.*, vol. 29, pp. 1505–1508, Nov 1972.

[21] G. Dolling and R. A. Cowley, "The thermodynamic and optical properties of germanium, Silicon, diamond and gallium arsenide," *Proceedings of the Physical Society*, vol. 88, no. 2, p. 463, 1966.

[22] Z. Iqbal, A. P. Webb, and S. Veprek, "Polycrystalline Silicon films deposited in a glow discharge at temperatures below 250C," *Applied Physics Letters*, vol. 36, no. 2, pp. 163–165, 1980.

[23] H. Richter, Z. P. Wang, and L. Ley, "The one phonon Raman spectrum in microcrystalline Silicon," *Solid State Communications*, vol. 39, no. 5, pp. 625–629, 1981.

[24] I. H. Campbell and P. M. Fauchet, "The effects of microcrystal size and shape on the one phonon Raman spectra of crystalline semiconductors," *Solid State Communications*, vol. 58, no. 10, pp. 739–741, 1986.

[25] J. . Takahashi and T. Makino, "Raman scattering measurement of silicon-on-insulator substrates formed by high-dose oxygen-ion implantation," *Journal of Applied Physics*, vol. 63, no. 1, pp. 87–91, 1988.

[26] W. Martienssen and H. Warlimont, *Springer Handbook of Condensed Matter and Materials Data*. Springer, 2005.

[27] T. Vucurevich, "3-D semiconductor's: More from Moore," in *Proceedings - Design Automation Conference*, p. 664, 2008.

[28] *Silvaco TCAD Omni License Brochure*.

[29] T. S. Gross, S. D. Hening, and D. W. Watt, "Crack formation during laser cutting of Silicon," *Journal of Applied Physics*, vol. 69, no. 2, pp. 983–989, 1991.

[30] Y. . Chen, W. . Lo, and T. . Kuo, "Thermal effect characterization of laser-ablated Silicon-through interconnect," in *ESTC 2006 - 1st Electronics Systemintegration Technology Conference*, vol. 1, pp. 594–599, 2007.

[31] K. K. Linder, F. C. Zhang, J. . Rieh, P. Bhattacharya, and D. Houghton, "Reduction of dislocation density in mismatched SiGe/Si using a low-temperature Si buffer layer," *Applied Physics Letters*, vol. 70, no. 24, pp. 3224–3226, 1997.

[32] S. Spiesshoefer, Z. Rahman, G. Vangara, S. Polamreddy, S. Burkett, and L. Schaper, "Process integration for through-Silicon vias," *Journal of Vacuum Science and Technology A: Vacuum, Surfaces and Films*, vol. 23, no. 4, pp. 824–829, 2005.

[33] N. Kawahara, M. Tagami, B. Withers, Y. Kakuhura, H. Imura, K. Ohto, T. Taiji, K. Arita, T. Kurokawa, M. Nagase, T. Maruyama, N. Oda, Y. Hayashi, J. Jacobs, M. Sakurai, M. Sekine, and K. Ueno, "A novel CoWP cap integration for porous low-k/Cu interconnects with NH_3 plasma treatment and low-k top (LKT) dielectric structure," in *2006 International Interconnect Technology Conference, IITC*, pp. 152–154, 2006.

[34] R. Nagarajan, K. Prasad, L. Ebin, and B. Narayanan, "Development of dual-etch via tapering process for through-Silicon interconnection," *Sensors and Actuators, A: Physical*, vol. 139, no. 1-2 SPEC. ISS., pp. 323–329, 2007.

[35] M. W. Newman, S. Muthukumar, M. Schuelein, T. Dambrauskas, P. A. Dunaway, J. M. Jordan, S. Kulkarni, C. D. Linde, T. A. Opheim, R. A. Stingel, W. Worwag, L. A. Topic, and J. M. Swan, "Fabrication and electrical characterization of 3D vertical interconnects," in *Proceedings - Electronic Components and Technology Conference*, vol. 2006, pp. 394–398, 2006.

[36] A. M. Rodin, J. Callaghan, and N. Brennan, "High throughput low CoO industrial laser drilling tool," *EuroAsia Semiconductor*, vol. 30, no. 6, pp. 11–15, 2008.

[37] D. M. Karnakis, "High power single-shot laser ablation of Silicon with nanosecond 355 nm," *Applied Surface Science*, vol. 252, no. 22, pp. 7823–7825, 2006.

[38] R. Dorn, S. Quabis, and G. Leuchs, "Sharper Focus for a Radially Polarized Light Beam," *Physical Review Letters*, vol. 91, no. 23, pp. 2339011–2339014, 2003.

[39] C. Krner, R. Mayerhofer, M. Hartmann, and H. W. Bergmann, "Physical and material aspects in using visible laser pulses of nanosecond duration for ablation," *Applied Physics A: Materials Science and Processing*, vol. 63, no. 2, pp. 123–131, 1996.

[40] A. Luft, U. Franz, A. Emsermann, and J. Kaspar, "A study of thermal and mechanical effects on materials induced by pulsed laser drilling," *Applied Physics A: Materials Science and Processing*, vol. 63, no. 2, pp. 93–101, 1997.

[41] E. Anastassakis, A. Pinczuk, E. Burstein, F. H. Pollak, and M. Cardona, "Effect of static uniaxial stress on the Raman spectrum of Silicon," *Solid State Communications*, vol. 8, no. 2, pp. 133–138, 1970.

[42] S. Ganesan, A. A. Maradudin, and J. Oitmaa, "A lattice theory of morphic effects in crystals of the diamond structure," *Annals of Physics*, vol. 56, no. 2, pp. 556–594, 1970.

[43] R. P. Koseski, W. A. Osborn, S. J. Stranick, F. W. Delrio, M. D. Vaudin, T. Dao, V. H. Adams, and R. F. Cook, "Micro-scale measurement and modeling of stress in Silicon surrounding a Tungsten-filled through-Silicon via," *Journal of Applied Physics*, vol. 110, no. 7, pp. 073517/1–10, 2011.

[44] S. Nadahara, S. Kambayashi, M. Watanabe, and T. Nakakubo, "Micro area stress around trench structure.," in *Conference on Solid State Devices and Materials*, pp. 327–330, 1987.

[45] I. De Wolf, "Micro-Raman spectroscopy to study local mechanical stress in Silicon integrated circuits," *Semiconductor Science and Technology*, vol. 11, no. 2, pp. 139–154, 1996.

[46] S. Wolf, *Silicon Processing for the VLSI Era.* Lattice Press, 1990.

[47] Y. Izawa, S. Tanaka, H. Kikuchi, Y. Tsurumi, and N. Miyanaga, "Debris-free in-air laser dicing for multi-layer mems by perforated internal transformation and ther-

mally induced crack propagation," in *MEMS 2008. IEEE International Conference on MEMS*, pp. 822–827.

[48] M. S. Amer, L. Dosser, S. LeClair, and J. F. Maguire, "Induced stresses and structural changes in Silicon wafers as a result of laser micro-machining," *Applied Surface Science*, vol. 187, no. 3-4, pp. 291–296, 2002.

[49] M. S. Amer, M. A. El-Ashry, L. R. Dosser, K. E. Hix, J. F. Maguire, and B. Irwin, "Femtosecond versus nanosecond laser machining: Comparison of induced stresses and structural changes in Silicon wafers," *Applied Surface Science*, vol. 242, no. 1-2, pp. 162–167, 2005.

[50] Y. Kimura and T. Katoda, "Effects of strain on crystallization of amorphous Silicon characterized by laser Raman spectroscopy," *Applied Surface Science*, vol. 117-118, pp. 790–793, 1997.

[51] W. E. Spear and P. G. Le Comber, "Investigation of the localised state distribution in amorphous Si films," *Journal of Non-Crystalline Solids*, vol. 8-10, no. C, pp. 727–738, 1972.

[52] W. Spear and P. L. Comber, "Substitutional doping of amorphous silicon," *Solid State Communications*, vol. 88, no. 11-12, pp. 1015 – 1018, 1993.

[53] W. E. Spear and P. G. L. Comber, "Electronic properties of substitutionally doped amorphous si and ge," *Philosophical Magazine*, vol. 33, no. 6, pp. 935–949, 1976.

[54] A. J. Lewis, G. A. N. Connell, W. Paul, J. R. Pawlik, and R. J. Temkin, "Hydrogen incorporation in amorphous germanium," *AIP Conference Proceedings*, vol. 20, no. 1, pp. 27–32, 1974.

[55] D. L. Staebler and C. R. Wronski, "Optically induced conductivity changes in discharge-produced hydrogenated amorphous silicon," *Journal of Applied Physics*, vol. 51, no. 6, pp. 3262–3268, 1980.

[56] G. Viera, S. Huet, M. Mikikian, and L. Boufendi, "Electron diffraction and high-resolution transmission microscopy studies of nanostructured Si thin films deposited by radiofrequency dusty plasmas," *Thin Solid Films*, vol. 403-404, pp. 467–470, 2002.

[57] M. Zeman, G. van Elzakker, F. D. Tichelaar, and P. Sutta, "Structural properties of amorphous Silicon prepared from hydrogen-diluted silane," *Philosophical Magazine*, vol. 89, no. 28, pp. 2435 – 2448, 2009.

[58] C. Smit, R. A. C. M. M. Van Swaaij, H. Donker, A. M. H. N. Petit, W. M. M. Kessels, and M. C. M. Van de Sanden, "Determining the material structure of microcrystalline Silicon from Raman spectra," *Journal of Applied Physics*, vol. 94, no. 5, pp. 3582–3588, 2003.

[59] I. H. Campbell and P. M. Fauchet, "The effects of microcrystal size and shape on the one phonon Raman spectra of crystalline semiconductors," *Solid State Communications*, vol. 58, no. 10, pp. 739 – 741, 1986.

[60] T. Kaneko, K.-i. Onisawa, M. Wakagi, Y. Kita, and T. Minemura, "Crystalline fraction of microcrystalline Silicon films prepared by plasma-enhanced chemical vapor deposition using pulsed silane flow," *Japanese Journal of Applied Physics, Part 1: Regular Papers and Short Notes and Review Papers*, vol. 32, no. 11 A, pp. 4907–4911, 1993.

[61] L. Houben, M. Luysberg, P. Hapke, R. Carius, F. Finger, and H. Wagner, "Structural properties of microcrystalline Silicon in the transition from highly crystalline to amorphous growth," *Philosophical Magazine A: Physics of Condensed Matter, Structure, Defects and Mechanical Properties*, vol. 77, no. 6, pp. 1447–1460, 1998.

[62] M. Ledinsk, A. Vetushka, J. Stuchlk, T. Mates, A. Fejfar, J. Kocka, and J. Łtepnek, "Crystallinity of the mixed phase Silicon thin films by Raman spectroscopy," *Journal of Non-Crystalline Solids*, vol. 354, no. 19-25, pp. 2253–2257, 2008.

[63] M. Heintze, R. Zedlitz, and G. H. Bauer, "Analysis of high-rate a-Si:H deposition in a VHF plasma," *Journal of Physics D: Applied Physics*, vol. 26, no. 10, pp. 1781–1786, 1993.

[64] T. Michna and A. R. Ellingboe, "Characterisation of an RF power splitter for multi-tile PECVD systems application," *Current Applied Physics*, vol. 11, no. 5 SUPPL., pp. S9–S11, 2011.

[65] M. Ledinsk, A. Vetushka, J. Stuchlk, A. Fejfar, and J. Kocka, "Raman mapping of microcrystalline Silicon thin films with high spatial resolution," *Physica Status Solidi (C) Current Topics in Solid State Physics*, vol. 7, no. 3-4, pp. 704–707, 2010.

[66] http://www.eigenvector.com.

[67] D. L. Williamson, "Medium-range order in a-Si:H below and above the onset of microcrystallinity," *Materials Research Society Symposium - Proceedings*, vol. 557, pp. 251–261, 1999.

[68] A. Guinier, *X-Ray Diffraction in Crystals, Imperfect Crystals and Amorphous Bodies*. W.H. Freeman and Company, 1963.

[69] B. Bitnar, "Silicon, Germanium and Silicon/Germanium photocells for thermophotovoltaics applications," *Semiconductor Science and Technology*, vol. 18, no. 5, pp. S221–S227, 2003.

[70] Y. Liu, M. D. Deal, and J. D. Plummer, "Rapid melt growth of Germanium crystals with self-aligned microcrucibles on Si substrates," *Journal of the Electrochemical Society*, vol. 152, no. 8, pp. G688–G693, 2005.

[71] M. Miyao, K. Toko, T. Tanaka, and T. Sadoh, "High-quality single-crystal Ge stripes on quartz substrate by rapid-melting-growth," *Applied Physics Letters*, vol. 95, no. 2, pp. 022115/1–3, 2009.

[72] M. Bain, M. Jin, S. H. Loh, P. Baine, B. M. Armstrong, H. S. Gamble, and D. W. McNeill, "Electrical characterization of SOI substrates incorporating WSi_x Ground planes," *IEEE Electron Device Letters*, vol. 26, no. 2, pp. 72–74, 2005.

[73] N. Zainal, S. Mitchell, D. McNeill, M. Bain, B. Armstrong, P. Baine, D. Adley, and T. Perova, "High quality thin-film germanium on insulator by rapid melt growth," in *UK Semiconductor Conference*, 2005.

[74] B. A. Weinstein and M. Cardona, "Second-order Raman spectrum of Germanium," *Physical Review B*, vol. 7, no. 6, pp. 2545–2551, 1973.

[75] Y. Yamamoto, P. Zaumseil, T. Arguirov, M. Kittler, and B. Tillack, "Low threading dislocation density Ge deposited on Si (1 0 0) using RPCVD," *Solid-State Electronics*, vol. 60, no. 1, pp. 2–6.

[76] K. Toko, T. Sakane, T. Tanaka, T. Sadoh, and M. Miyao, "Defect-free single-crystal Ge island arrays on insulator by rapid-melting-growth combined with seed-positioning technique," *Applied Physics Letters*, vol. 95, no. 11, pp. 112107/1–3, 2009.

[77] T. Sadoh and M. Miyao, "High-mobility Ge on insulator by SiGe mixing-triggered rapid-melting-growth," in *ECS Transactions*, vol. 33, pp. 409–418, 2010.

[78] W. Jaffe, W. Cook, and H. Jaffe, *Piezoelectric Ceramics*. Academic Press, New York, 1971.

[79] H. Zheng, I. M. Reaney, G. D. C. Csete De Gyrgyfalva, R. Ubic, J. Yarwood, M. P. Seabra, and V. M. Ferreira, "Raman spectroscopy of $CaTiO_3$-based perovskite solid solutions," *Journal of Materials Research*, vol. 19, no. 2, pp. 488–495, 2004.

[80] S. V. Kalinin, S. Jesse, B. J. Rodriguez, Y. H. Chu, R. Ramesh, E. A. Eliseev, and A. N. Morozovska, "Probing the role of single defects on the thermodynamics of

electric-field induced phase transitions," *Physical Review Letters*, vol. 100, no. 15, pp. 155703/1–4, 2008.

[81] G. Burns and B. A. Scott, "Raman spectra of polycrystalline solids; application to the $PbTi_{1-x}Zr_xO_3$ system," *Physical Review Letters*, vol. 25, no. 17, pp. 1191–1194, 1970.

[82] S. Sriram, M. Bhaskaran, T. S. Perova, V. A. Melnikov, and A. S. Holland, "In situ investigation of thermally influenced phase transformations in $(pb_0.92sr_0.08)(zr_0.65ti_0.35)O_3$ thin films using micro-Raman spectroscopy and X-Ray diffraction," *IEEE transactions on ultrasonics, ferroelectrics, and frequency control*, vol. 56, no. 2, pp. 241–245, 2009.

[83] K. Wasa, M. Kitabatake, and H. Adachi, *Thin Film Materials Technology - Sputtering of Compound Materials*. William Andrew Publishing, 2004.

[84] S. Sriram, M. Bhaskaran, A. S. Holland, K. T. Short, and B. A. Latella, "Measurement of high piezoelectric response of Strontium-doped lead Zirconate Titanate thin films using a nanoindenter," *Journal of Applied Physics*, vol. 101, no. 10, pp. 104910/1–5, 2007.

[85] M. Bhaskaran, S. Sriram, D. R. G. Mitchell, K. T. Short, and A. S. Holland, "Effect of multi-layered bottom electrodes on the orientation of Strontium-doped lead Zirconate Titanate thin films," *Thin Solid Films*, vol. 516, no. 22, pp. 8101–8105, 2008.

[86] S. Sriram, M. Bhaskaran, and A. S. Holland, "The effect of post-deposition cooling rate on the orientation of piezoelectric $(Pb_{0.92}Sr_0.08)(Zr_{0.65}Ti_{0.35})O_3$ thin films deposited by RF magnetron sputtering," *Semiconductor Science and Technology*, vol. 21, no. 9, pp. 1236–1243, 2006.

[87] C. E. F. Costa, F. M. Pontes, A. G. Souza, E. R. Leite, P. S. Pizani, and E. Longo, "Influence of Strontium concentration on the structural, morphological, and electrical

properties of lead Zirconate Titanate thin films," *Applied Physics A: Materials Science and Processing*, vol. 79, no. 3, pp. 593–597, 2004.

[88] M. Deluca, T. Sakashita, and G. Pezzotti, "Polarized Raman scattering of domain structures in polycrystalline lead zirconate titanate," *Applied Physics Letters*, vol. 90, no. 5, pp. 051919/1–3, 2007.

[89] D. C. Agrawal, S. B. Majumder, Y. N. Mohapatra, S. Sathaiah, H. D. Bist, R. S. Katiyar, E. Ching-Prado, and A. Reynes, "Micro-Raman spectroscopy of sol-gel-derived $Pb(Zr_xTi_{1-x})O_3$ thin films," *Journal of Raman Spectroscopy*, vol. 24, no. 7, pp. 459–462, 1993.

[90] C. M. Foster, Z. Li, M. Grimsditch, S. . Chan, and D. J. Lam, "Anharmonicity of the lowest-frequency A_1(TO) phonon in $PbTiO_3$," *Physical Review B*, vol. 48, no. 14, pp. 10160–10167, 1993.

[91] F. Nava, B. Z. Weiss, K. Y. Ahn, D. A. Smith, and K. N. Tu, "Thermal stability and electrical conduction behavior of coevaporated WSi thin films," *Journal of Applied Physics*, vol. 64, no. 1, pp. 354–364, 1988.

[92] F. Nava, E. Mazzega, M. Michelini, O. Laborde, O. Thomas, J. P. Senateur, and R. Madar, "Analysis of the electrical resistivity of Ti, Mo, Ta, and W monocrystalline disilicides," *Journal of Applied Physics*, vol. 65, no. 4, pp. 1584–1590, 1989.

[93] J. H. Liang and D. S. Chao, "Formation of Tungsten silicide films by ion beam synthesis," *Surface and Coatings Technology*, vol. 140, no. 2, pp. 116–121, 2001.

[94] N. Thomas, P. Suryanarayana, E. Blanquet, C. Vahlas, R. Madar, and C. Bernard, "LPCVD WSi_2 films using Tungsten chlorides and silane," *Journal of the Electrochemical Society*, vol. 140, no. 2, pp. 475–481, 1993.

[95] K. C. Saraswat, D. L. Brors, J. A. Fair, K. A. Monnig, and R. Beyers, "Properties Of Low-Pressure CVD Tungsten Silicide For MOS VLSI Interconnections.," *IEEE Transactions on Electron Devices*, vol. ED-30, no. 11, pp. 1497–1505, 1983.

[96] S. G. Telford, M. Eizenberg, M. Chang, A. K. Sinha, and T. R. Gow, "Chemically vapor deposited Tungsten Silicon films using dichlorosilane in a single-wafer reactor," *Journal of the Electrochemical Society*, vol. 140, no. 12, pp. 3689–3701, 1993.

[97] J. . Chen, Y. . Fang, and S. . Hsu, "Growth of Tungsten silicide films by low pressure CVD method," *Vacuum*, vol. 37, no. 3-4, pp. 357–361, 1987.

[98] S. Liao, M. Bain, P. Baine, J. H. Montgomery, D. W. McNeill, B. M. Armstrong, and H. S. Gamble, "Dopant transport in Tungsten silicide buried layers for application in SSOI," in *ECS Transactions*, vol. 28, pp. 331–341, 2010.

[99] C. L. Chu, K. C. Saraswat, and S. S. Wong, "Measurement of lateral dopant diffusion in thin silicide layers," *IEEE Transactions on Electron Devices*, vol. 39, no. 10, pp. 2333–2340, 1992.

[100] O. Chaix-Pluchery, L. Abello, G. Lucazeau, B. Chenevier, and R. Madar, "A Raman study of single crystal and thin film tetragonal WSi_2," *Journal of Physics and Chemistry of Solids*, vol. 57, no. 5, pp. 527–537, 1996.

[101] O. Chaix-Pluchery, F. Genet, G. Lucazeau, and R. Madar, "Raman study of tetragonal Tungsten disilicide," *Applied Surface Science*, vol. 91, no. 1-4, pp. 68–71, 1995.

[102] C. W. Maa, J.and Magee and J. J. O'Neill, "Phosphorus Out Diffusion From Double-Layered Tantalum Silicide/Polycrystalline Silicon Structure.," *Journal of Vacuum Science and Technology B: Microelectronics and Nanometer Structures*, vol. 1, no. 1, pp. 1–5, 1983.

Appendices

Appendix A

List of Publications

Journal Publications

1. Wasyluk, J., **Adley, D.**, Perova, T.S., Rodin, A.M., Callaghan, J., Brennan, N. (2009) Micro Raman investigation of stress distribution in laser drilled via structures Applied Surface Science, 255(10): 5546-5548.

2. Monaghan, E. , Michna, T., Gaman, C., O'Farrel, D., Ryan, K., **Adley, D.**, Perova, T.S., Drews, B., Jaskot, M., Ellingboe, A.R. (2011). Characterisation of thin film silicon films deposited by plasma enhanced chemical vapour deposition at 162 MHz, using a large area, scalable, multi-tile-electrode plasma source ThinSolid Film 519(20): 6884-6886

3. Bhaskaran, M., Sriram, S., **Adley, D.**, Perova, T.S., Mitchell, (2011) A Reversal and pinning of Curie point transformations in thin film piezoelectrics. CrystEngComm, 13: 1280-1282

4. Zainal, N., Mitchell, S. J. N., McNeill, D. W., Bain, M. F., Armstrong, B. M., Baine, P. T., **Adley, D.**, Perova, T. S. (2012) Characterization of Rapid Melt Growth (RMG) Process for High Quality Thin Film Germanium on Insulator. ECS Trans. 45(4) 169-180

Oral Presentation

Adley D. (2009) Raman analysis of thermal damage in laser micro machined silicon substrates. Intel European Technology Research Conference, Leixlip, Co. Kildare. September 9-11th 2009

Conference presentations

1. Wasyluk, J., **Adley, D.**, Perova, T.S., Wadsworth, H., Gamble, H.S. (2008) Raman line and area mapping experiments for composition, stress and defects identification in SiGe structures. 32nd Annual Microscopic Society Ireland Symposium, The Queens University Belfast, Month 2008.

2. Wasyluk, J., **Adley, D.**, Perova, T.S., Wadsworth, H., Gamble, H.S., Luytovich, K. and Kasper, E..(2008) Raman line and area mapping experiments for composition, stress and defects identification in SiGe structures. AFM Forum & Workshop, University College Dublin, November 2008

3. **Adley, D.**U., Perova, T.S., Bain, M.F., Armstrong, B.F. (2009) Analysis of Phosphorous diffused Tungsten Silicide using Ramen Spectroscopy. 33rd Annual Microscopical Society of Ireland (MSI) Symposium, University College Dublin, August 26-29, 2009, p40

4. **Adley, D.**, Wasyluk, J., Perova, T.S., Giordani, S., Wadsworth, H., Gamble, H.S., Armstrong, M., Lyutovich, K., Oehme, M. (2010) Investigation of surface roughness caused by crosshatched patterns in SiGe epilayers. International Workshop In situ characterization of near-surface processes Workshop, May 30 - June 3, 2010 Montan University, Eisenerz, Austria

5. Monaghan, E., Michna, T., O'Hara, N., Gaman, D., O'Farrel, D., Ryan, K., **Adley, D.**, Perova, T.S., Drews, B., Jaskot,M., Ellingboe, A.R. (2010) Characterisation of

PECVD Films Deposited at 162MHz Using a Large Area, Scalable, Segmented Electrode Topology, European Physical Society (EPS) Conference on Plasma Physics, Dublin City University, June 21st - 25th 2010

6. **Adley, D.**, Perova, T.S., Monaghan, E., Ellingboe, A.R. (2009) Micro-Raman Investigation of Amorphous and Microcrystalline Silicon films deposited by Plasma Enhanced CVD. International Meeting on Developments in Materials, Processes and Applications of Emerging Technologies (MPA), Braga, Portugal, 28th-30th July 2010.

7. **Adley, D.**, Perova, T.S., Monaghan, E., Ellingboe, A.R., (2010) Micro-Raman Investigation of Amorphous and Microcrystalline Silicon films deposited by Plasma Enhanced CVD, The Microscopical Society of Ireland and the Northern Ireland Biomedical Engineering Society, Joint Annual Symposium, 34th MSI Symposium 25th - 27th August 2010, University of Ulster, Jordanstown.

8. Zainal, N., Mitchell, S.J.N., McNeill, D.W., Bain, M.F., Armstrong, B.M., Baine, P., **Adley, D.**, and Perova, T.S. (2011) High quality thin-film Germanium on insulator by Rapid Melt Growth, 2011 UK Semiconductor Conference, University Of Sheffield, July 2011

9. Zainal, N., Mitchell, S.J.N., McNeill, D.W., Bain, M.F., Armstrong, B.M., Baine, P., **Adley, D.**, and Perova, T.S. (2012) Characterization of Rapid Melt Growth (RMG) Process for High Quality Thin Film Germanium on Insulator, 221st Meeting of The Electrochemical Society (ECS), Seattle, Washington 6-10th May 2012

Appendix B

MATLAB Code

Although commercial applications are available to fit spectra with non-linear curves they often have limited functionality and do not allow fine grained control over the process. MATLAB provides a robust development environment that allows incredibly sophisticated and flexible manipulation of data along with excellent graphing tools. Therefore several scripts were developed that provide extensively customisable non-linear fitting including support for asymmetrical fitting functions, multiple functions per peak, fine gained control of fitting parameters such as the FWHM, peak position and intensity. MATLAB also allowed large numbers of spectra to be fitted automatically and graphed this was invaluable when dealing with multiple spectra from mapping experiments. In order to separate peaks from background noise and baselines, a MATLAB script was written removed the baseline from the spectra either through hard coded limits or automatically based on the slope of the curve. Once this was completed a large number of subsidiary scripts were then used to perform important functions such as subtraction, calculation of Xc fraction, 2D and 3D graphing of individual spectra from mapping and calculating stress. The three most important scripts are included.

Listing B.1 – Plot spectra statistics such as peak position, FWHM. Calls a fitting function and a baseline subtraction functions listed below. Can fit many separate peaks and composite peaks comprising up to three components

```
function [mydata] =  fitall(inputmat,typeoffit,spectra)


%%%%%%%%%%%%SETTINGS%%%%%%%%%%%%%%%%%%%%%%%%
graph_spacing = 1; %Number of files to operate on before showing a graph
scaled_fitting = false; %use the scaled data when peak fitting
%%%%%%%%%%%%%%%%%%%%%%%%%%%%%%%%%%%%%%%%%%%%
warning on all
warning off MATLAB:gui:latexsup:BadTeXString; %MATLAB bug
warning backtrace off; %not good for debugging
[rows, cols] = size(inputmat);

if nargin == 1
    typeoffit = 'gauss';
    cprintf('comments','defaulting to gaussian fit\n');
end

% Import the file


if nargin == 1 || nargin == 2

    cprintf('comments','defaulting to dat files\n');
    datFiles = dir('*.dat');
    numfiles = length(datFiles);
    filenames =  cell(numfiles,1);
    for fi = 1:numfiles
        filenames{fi} = datFiles(fi).name;
    end
    filenames = sort_nat(filenames);
```

```
    mydata = cell(rows+3, max([numfiles rows]));
    mydata{1,1}.brieftitles = cell(numfiles,1);
    mydata{1,1}.filenames = cell(numfiles,1);
    mydata{1,1}.titles = cell(numfiles,1);
end

if nargin == 3

    if ischar(spectra)
        addpath(genpath('C:\Users\adleyd\Documents\MATLAB\GSTools\'));
        spectra = GSSpcRead(spectra);
        [zz,numfiles] = size(spectra.spectra);
         mydata = cell(rows+3, max([numfiles rows]));
         mydata{1,1}.brieftitles = cell(numfiles,1);
    else
        spectra = spectra;
        [zz,numfiles] = size(spectra);
        mydata = cell(rows+3, max([numfiles rows]));
        mydata{1,1}.brieftitles = cell(numfiles,1);
    end



end

for w = 1:rows
    fxnsperpeak  = inputmat(w,4);
    mydata{rows+3,w}.centres = zeros(numfiles,fxnsperpeak);
    mydata{rows+3,w}.heights = zeros(numfiles,fxnsperpeak);
    mydata{rows+3,w}.fwhms = zeros(numfiles,fxnsperpeak);
    mydata{rows+3,w}.areas = zeros(numfiles,fxnsperpeak);
    mydata{rows+3,w}.shapes = zeros(numfiles,fxnsperpeak);
    mydata{rows+3,w}.roughheights = zeros(numfiles,1);
```

```
    mydata{rows+3,w}.roughcentres = zeros(numfiles,1);
end

for k = 1:numfiles

    if nargin == 1 || nargin == 2

        mydata{1,k} = importdata(filenames{k},',',3);
        mydata{1,1}.filenames{k,1} = filenames{k};
        mydata{1,1}.titles{k,1} = char(mydata{1,k}.textdata(1,1));
        mydata{1,1}.brieftitles{k,1} = char(mydata{1,k}.textdata(2,1));
        mydata{rows+2,k} = char(mydata{1,k}.textdata(2,1));

        %baseline_subtraction =
        %get_rmbaseline(mydata{1,k}.data,25,mydata{1,k}.textdata,inputmat
            );

        cprintf('Comments',['Curently processing: ' char(mydata{1,k}.
            textdata(2,1)) '\n']);

    end

    if nargin == 3
            mydata{1,1}.brieftitles{k,1} = char(['spec_' num2str(k) ]);%'
                _' spectra.Comment]);
            if ischar(spectra)
                mydata{1,1}.titles{k,1} = mydata{1,1}.brieftitles{k,1};
                data = [spectra.spectra(1,k).xaxis(1,1:end)' spectra.
                    spectra(1,k).data(1,1:end)'];
                mydata{1,k}.data = data;
            else
                mydata{1,1}.titles{k,1} = char(['spec_' num2str(k) ]);
                data = [spectra(:,1) spectra(:,2)];
                mydata{1,k}.data = data;
```

```
        end


end

original = mydata{1,k}.data;
data = mydata{1,k}.data;

for z = 1:rows
    rangedata = data(data(:,1) > inputmat(z,1) & data(:,1) < inputmat
        (z,2),:);
    data(data(:,1) > inputmat(z,1) & data(:,1) < inputmat(z,2),2) =
        rmbaseline(data, inputmat(z,3), inputmat(z,1), inputmat(z,2));
    rangedata(:,2) = rangedata(:,2) - data(data(:,1) > inputmat(z,1)
        & data(:,1) < inputmat(z,2),2); %subtraction messy.
    [mydata{rows+3,z}.roughheights(k,1), maxpos] = max(rangedata(:,2)
        );
    mydata{rows+3,z}.roughcentres(k,1) = rangedata(maxpos,1);

end

baseline_subtraction = original(:,2) - data(:,2);

if  scaled_fitting == true;
    mydata{1,k}.baseline = baseline_subtraction;
    mydata = scalespec(mydata,k);
    baseline_subtraction = mydata{1,k}.scaledbaseline;
end


%Scale the data based on peaks or excluding peaks

%Controversial:
```

```
%Can be used to push all values above 0 and possibly improve fit. Is
    it
%better to smooth baselien and add quite a bit to the data or use
    original
%values? Fixed: Recursive line fitting in rmbaseline should do a
    better job
%if(min(baseline_subtraction) < 0)
%    baseline_subtraction = baseline_subtraction + abs(min(
    baseline_subtraction));
%end


for i = 2:rows+1

    fxnsperpeak = inputmat(i-1,4);

    %%Send each peak to the fitting function
    [mydata{i,k}.fit,mydata{i,k}.gof, fxhandles,output] =
        createFit_Pv(mydata{1,k}.data(:,1), baseline_subtraction,
        fxnsperpeak ,inputmat(i-1,1),inputmat(i-1,2),typeoffit);

    %Confidence intervals (95%)
    mydata{i,k}.confint = confint(mydata{i,k}.fit);
    mydata{i,k}.confint = [mydata{i,k}.confint; abs(mydata{i,k}.
        confint(2,:) - mydata{i,k}.confint(1,:))];
    mydata{i,k}.output = output;
    mydata{i,k}.fxhandles = fxhandles;

    %%%%%%%%%%%%%%%%%%% GRAPHS %%%%%%%%%%%%%%%%%%%%%%%%%%
    if mod(k,graph_spacing) == 0 || k == 1 %Space graphs according to
        settings not every spectra is plotted (speeds things up)

        %Original spectra and baseline
```

```
if i == 2 %% Only show original spectra and baseline once per
    spectra (Not every peak)
    figure('name',['baseline: ' mydata{1,1}.titles{k,1}],'
        Units','Pixels','Position',[1100 357 688 486],'
        WindowStyle', 'docked');
    plot(original(:,1),original(:,2),'r-',data(:,1),data(:,2)
        ,'b-', data(:,1), baseline_subtraction ,'g-' );
    title(mydata{1,1}.titles{k,1},'interpreter','none');
    legend('Original Spectra','Baseline', 'Subtraction');
end

%Graph with fitted fxns
figure('name',['fit ' num2str(i-1) ': ' mydata{1,1}.
    brieftitles{k,1}],'Visible','off');

% Set up figure to receive datasets and fits
f_ = clf;
set(f_,'Units','Pixels','Position',[276 357 688 486]);
legh_ = []; legt_ = {};   % handles and text for legend
xlim_ = [Inf -Inf];       % limits of x axis
ax_ = axes;
set(ax_,'FontSize',14,'FontWeight','Bold')
set(ax_,'Units','normalized','OuterPosition',[0 0 1 1]);
set(ax_,'Box','on');
grid(ax_,'on');
axes(ax_); hold on;


% ---- Plot data originally in dataset "Raman Spectra"
X1 = mydata{1,k}.data(:,1);
X1 = X1(:); % column vector
Y1 = baseline_subtraction;
Y1 = Y1(:);
```

```
h_ = line(X1,Y1,'Parent',ax_,'Color',[0.333333 0.666667
    0],...
    'LineStyle','none', 'LineWidth',1,...
    'Marker','.', 'MarkerSize',12);
xlim_(1) = min(xlim_(1),min(X1));
xlim_(2) = max(xlim_(2),max(X1));
legh_(end+1) = h_;
legt_{end+1} = 'Raman_Spectra';

% Nudge axis limits beyond data limits
if all(isfinite(xlim_))
    xlim_ = xlim_ + [-1 1] * 0.01 * diff(xlim_);
    set(ax_,'XLim',xlim_)
else
    set(ax_, 'XLim',[202.76653349999998, 819.62647650000008])
        ;
end


%plot functions individually
for fxns = 1:length(fxhandles)
    fplot(fxhandles{fxns}, [X1(1) X1(end)]);
end


% Plot this fit
h_ = plot(mydata{i,k}.fit,'fit',0.95);
legend off;  % turn off legend from plot method call
set(h_(1),'Color',[1 0 0],'LineStyle','-', 'LineWidth',2,'
   Marker','none', 'MarkerSize',6);
legh_(end+1) = h_(1);

switch typeoffit
    case 'gauss'
```

```
            legt_{end+1} = 'Fitted Gaussian(s)';
        case 'lornz'
            legt_{end+1} = 'Fitted Lorentzian(s)';
        case 'pv'
            legt_{end+1} = 'Fitted PseudoVoight(s)';
        case 'asym'
            legt_{end+1} = 'Fitted Asymmetrical(s)';
        otherwise
            legt_{end+1} = 'Fitted Function(s)';
    end


    % Done plotting data and fits.  Now finish up loose ends.
    hold off;
    leginfo_ = {'Orientation', 'vertical', 'Location', 'NorthEast
        '};
    h_ = legend(ax_,legh_,legt_,leginfo_{:}); % create legend
    set(f_,'WindowStyle', 'docked','Visible','on');
    xlabel(ax_,'Wavenumber (cm^{-1})','FontSize',14,'FontWeight',
        'Bold');                % x label
    ylabel(ax_,'Intensity (Raman Counts)','FontSize',14,'
        FontWeight','Bold');                % y label
    title(mydata{1,1}.titles{k,1},'FontSize',14,'FontWeight','
        Bold');


end
%%%%END OF GRAPHS%%%%

%%%%OUTPUT RELEVANT STATISTICS %%%%

mydata{i,k}.coeffs = [coeffnames(mydata{i,k}.fit) num2cell(
    coeffvalues(mydata{i,k}.fit))'];

coeffs = coeffvalues(mydata{i,k}.fit);
```

```
errors = confint(mydata{i,k}.fit);

if strcmp(typeoffit,'pv')
    noshape = coeffs(1:length(coeffs)-fxnsperpeak);
    coeffs = [reshape(noshape,3,fxnsperpeak); coeffs(length(
        coeffs)-fxnsperpeak+1:end)];
    coeffs = coeffs';
    coeffs= sortrows(coeffs,-2);
    %If errrorbars are added they chould really include shape
    %errors as well as these are significant and can mask other
        errors in centres for instance. This would also
    %require upgrading the plot_vars +... not now
    mydata{rows+3,i-1}.shapes(k,:) = coeffs(:,4);
    mydata{rows+3,i-1}.areas(k,:) = coeffs(:,1) .* abs(coeffs
        (:,3)) .* ((coeffs(:,4) * pi) + (1 - coeffs(:,4)) * sqrt(
        pi/log(2)));

    %errors don't include shape and plot_vars shouldn't plot
        shape.
    error_without_shape = errors(:,1:end-fxnsperpeak);
    temp1 = reshape(mean(error_without_shape),3,fxnsperpeak)';
    temp2 = reshape((abs(error_without_shape(2,:)-
        error_without_shape(1,:))/2),3,fxnsperpeak)';
    errors = [temp1 temp2];
    errors = sortrows(errors,-2);

elseif strcmp(typeoffit,'asym')
    %NB in order for this to work coefficients must be specified
        in
    %fitting function
    %like height,centre,hwhm1a,hwhm1b, height2,centre2,hwhm2a,
        hwhm2b
    %NOt like is done with the shape where they are all at the
        end.
```

```
        %merged_hwhms = coeffs(length(coeffs)-(2*fxnsperpeak):length(
            coeffs)-(2*fxnsperpeak)+fxnsperpeak) + coeffs(length(
            coeffs)-fxnsperpeak:end);
        %coeffs_merged_hwhms = [coeffs(1:length(coeffs)-(2*
            fxnsperpeak)-1); merged_hwms/2];


        coeffs = reshape(coeffs,4,fxnsperpeak)';
        coeffs = sortrows(coeffs,-2);

        errors = [reshape(mean(errors),4,fxnsperpeak)' reshape(abs(
            errors(2,:)-errors(1,:))/2,4,fxnsperpeak)'];
        errors = sortrows(errors,-2);

        mydata{rows+3,i-1}.hwhm1(k,:) = coeffs(:,3);
        mydata{rows+3,i-1}.hwhm2(k,:) = coeffs(:,4);
        mydata{rows+3,i-1}.realfwhm(k,:) = coeffs(:,3) + coeffs(:,3);
        mydata{rows+3,i-1}.areas(k,:) = coeffs(:,1) .* abs(0.5 * (
            coeffs(:,3) + coeffs(:,3))) .* pi; % approx area


        warning('The fwhm in the structure is the first fwhm not a
            sum of both!!');
        %plot_vars will only plot the first hwhm and associate the
        %errors of only that one. I guess it could plot the second
            one
        %as well...

    elseif strcmp(typeoffit,'gauss') || strcmp(typeoffit,'lornz')
        coeffs = reshape(coeffs,3,fxnsperpeak)';
        coeffs= sortrows(coeffs,-2);
```

```
            errors = [reshape(mean(errors),3,fxnsperpeak)' reshape(abs(
                errors(2,:)-errors(1,:))/2,3,fxnsperpeak)'];
            errors = sortrows(errors,-2);
            %NB errors
            %First three used solely to put into the correct order

            if strcmp(typeoffit,'gauss')
                mydata{rows+3,i-1}.areas(k,:) = coeffs(:,1) .* abs(coeffs
                    (:,3)) .* sqrt(pi / .69314);
                %Gaussian area = height * abs(hwhm) * sqrt(pi / Ln2)
            else
                mydata{rows+3,i-1}.areas(k,:) = coeffs(:,1) .* abs(coeffs
                    (:,3)) .* pi;
                %Lorentzian area =  height * abs(hwhm) * pi
            end

        end

        mydata{rows+3,i-1}.errorheights(k,:) = errors(:,4);
        mydata{rows+3,i-1}.errorcentres(k,:) = errors(:,5);
        mydata{rows+3,i-1}.errorfwhms(k,:) = errors(:,6);
        mydata{rows+3,i-1}.heights(k,:) = coeffs(:,1) ;
        mydata{rows+3,i-1}.centres(k,:) = coeffs(:,2);
        mydata{rows+3,i-1}.fwhms(k,:) = 2 * coeffs(:,3); %value in coeff
            is hwhm

        %PseudoVoight area

    end

end

end
```

Listing B.2 – Attempt to remove the baseline from a Raman spectra

```
function [ origintensities ] = rmbaseline(data, snr, minpoint, maxpoint)
%rmbaseline data, size of window (10ish), snr
%   data, size of window, snr.

%%%%%%%SETTINGS%%%%%%%%%%%%%%%%%%%%%%%%%%%%%%%%
    minlength = 25; %Min length of peak (approx 1 cm-1 per point)
    num_of_subsections = 41; %num_of_subsections of 2, 7, 14, 41, 82, 287
        give round numbers
    rangewarn = .05; %Issue warning when peak is this % close to either
       end
    maxunderline = 2; %Max points to allow under any line
    minrecline = 1000; %min length of line before recursive fitting as it
        doesn't work on short lines
    windowpts = 15; %size of window to use
    useweighted = false; %NB If useweighted is true then stds are
       weighted useful for detecting weak peaks but not good for sharp Si
        peaks!!!

%%%%%%%%%%%%%%%%%%%%%%%%%%%%%%%%%%%%%%%%%%%%%%%%%%%%


    %smooth data first otherwise we get false positives
    %intensities = sgolayfilt(data(:,2),2,41);
    if(nargin < 4)
       intensities = data(:,2);
    else
       intensities = data(data(:,1) > minpoint & data(:,1) < maxpoint,2);
    end

    origintensities = intensities;
    %Smoothed to find peaks
    intensities = smooth(intensities,7,'moving');
```

```
datalength = length(intensities);
subsection_size = floor(datalength/num_of_subsections);

windowedstds = intensities;
for i = 1:num_of_subsections
   start = 1+(i-1)*subsection_size;
   endnum =  i*subsection_size;
   windowedstds( start : endnum ) = std( intensities(start : endnum )
      );
end

if ~useweighted
    windowedstds(:) = 1;
end
%First get weighted variance then use sqrt to get standard deviation
weightedstd = sqrt(var(intensities ,windowedstds));
baseline = intensities;
start = 1;
endnum = windowpts + 1;

if endnum > length(intensities)
    error 'Window_length_too_long';
end

for i = 1:datalength

  [maxvalue ,maxpos] = max(intensities(start : endnum ));
  [minvalue ,minpos] = min(intensities(start : endnum ));

  if minpos > maxpos || i > datalength - windowpts %on downward slopr
      (backward looking window) maintain peak as long as pos
      endnum = i;
      if(i > windowpts)
```

```
            start = i-windowpts;
        else
            start = 1;
        end
    else %forward looking window
        endnum =  i + windowpts;
        start = i;
    end

    ydiff = max(intensities(start : endnum )) - min(intensities(start :
        endnum ));

    if ydiff > snr*weightedstd
        baseline(i) = 0;
    elseif snr == -1
        baseline(i) = 0;
    %elseif ydiff < snr*weightedstd
    end
end

%remove all small clumps of baseline and peaks < minlength
start = 1;
tosearch = baseline > 0;
for i = 1:datalength-1
    if tosearch(i+1) ~= tosearch(i) %transition
        if i - start < minlength %bad transition
            tosearch(start : i) = not(i);
        end
        start = i + 1;
    end
end
baseline = baseline .* tosearch;

%Find baseline between two points
```

```
zerosbl = find(baseline == 0);
start = 1;

for i = 1:length(zerosbl) %looking at matrix indices now not the
    values
     if  i == length(zerosbl) || (zerosbl(i) + 1 ~= zerosbl(i+1))
         datastart = zerosbl(start);
         dataend = zerosbl(i);

         %Use original baseline values now that peaks have been found
         %from smoothed version.
         peakvalues = origintensities(datastart:dataend);
         [peakvalue, peakpos] = max(peakvalues);

         if (dataend - datastart) < (3*minlength)
             floor(data(data(:,2) == origintensities(datastart),1))
             floor(data(data(:,2) == origintensities(dataend),1))
             warning('Very short peak < 3*minlength (%d cm-1 to %d cm
                 -1) possibly a stub',floor(data(data(:,2) ==
                 origintensities(datastart),1)),floor(data(data(:,2) ==
                  origintensities(dataend),1)));
         elseif (peakpos > (length(peakvalues) * (1 - rangewarn)) ||
            peakpos < (length(peakvalues) * rangewarn)) &&
            origintensities(peakpos) ~= 0
             warning('!!! Peak at %d is at extremity of range (%d cm-1
                 to %d cm-1), re adjust range as false positive
                 possible !!!',floor(data(data(:,2) == origintensities(
                 peakpos),1)),floor(data(data(:,2) == origintensities(
                 datastart),1)),floor(data(data(:,2) == origintensities
                 (dataend),1)));
         end

         %Make sure minimum points are used to create the line.
         [minstartvalue, minstart] = min(peakvalues(1:peakpos));
```

```
[minendvalue, minend] = min(peakvalues(peakpos:end));
minend = minend + peakpos - 1;

%recursive while to find lowest point after subtraction
    rarely
%needs to go more than once.
allabove = 0;
while allabove == 0

    %Find line parameters
    ydiff = peakvalues(minend) - peakvalues(minstart);
    xdiff = minend - minstart;
    slope = ydiff/xdiff;
    xvals = [1:minend-minstart+1]';

    %Determine if any points are below the line
    subtraction  = peakvalues(minstart:minend) -( (slope *
        xvals) + peakvalues(minstart,1));

    [subminvalue, subminpos] = min(subtraction);
    subminpos = subminpos + minstart - 1;

    if sum(subtraction < 0) > maxunderline && subminpos >
        peakpos && (dataend - datastart) > minrecline &&
        minend ~= subminpos%downward slope
        warning('Extra linear line step(s) required is range
            properly set up?');
        minend = subminpos;
    elseif sum(subtraction < 0) > maxunderline && subminpos <
        peakpos && (dataend - datastart) > minrecline &&
        minstart ~= subminpos %rising slope
        warning('Extra linear line step(s) required is range
            properly set up?');
        minstart = subminpos;
```

```
                else
                    allabove = 1;
                    peakvalues(minstart:minend) = (slope * xvals) +
                        peakvalues(minstart,1);% y = mx + c
                    %peakvalues(minstart:minend) = 0; %DEBUG
                end
            end

            origintensities(datastart : dataend) = peakvalues;
            start = i + 1;

        end
    end

    %figure; plot(data(1:datalength,1),intensities,'r-',data(1:datalength
        ,1),origintensities,'b-'); %,data(1:datalength,1), rmbaselinec(data
        ,windowpts,snr),'g-');
    %title(textlabel(1));
    %plot(diff(intensities,1),'m-');
end
```

Listing B.3 – Fitting of Raman spectra files, can do Asymmetric, Pseudovoight, Lorentzian and Gaussian fits

```
function [ cf_, gof, fxhandles, output ] = createFit_Pv(X1,Y1,fxnsperpeak
    ,minexclude,maxexclude,typeoffit)
% Data from dataset "Raman Spectra":
%     X = X1:
%     Y = Y1:
%     Unweighted
%


%%SETTINGS%%%%%
%NB: MUST ENTER UPPER BOUNDS if not using default 0 Inf as start point is
    mid way between the two!!!!!
%Fitting will fail otherwise
%Generally lowerbounds = 0, upperbounds = Inf
%                    [height centre hwhm]
%peak1_lowerparams = [(max(Y1)/8) 400 1];
%peak1_upperparams = [(max(Y1)/3) 500 50];
peak1_lowerparams = [0 0 0];
peak1_upperparams = [Inf Inf Inf];
peak2_lowerparams = [0 0 0];
peak2_upperparams = [Inf Inf Inf];
peak3_lowerparams = [0 0 0];
peak3_upperparams = [Inf Inf Inf];
peak4_lowerparams = [0 0 0];
peak4_upperparams = [Inf Inf Inf];
%%%%%%%%%%%%%%%%%%%%
%%%%%%%%%%%%%%%%%%%%


X1 = X1(:);
Y1 = Y1(:);
```

```
% ---- Create fit "3 PseudoVoigts(exclusion)"

% Apply exclusion rule "erule"
if length(X1) < 316
    error('Exclusion rule ''%s'' is incompatible with ''%s''.','erule','
        X1');
end
ex_ = false(length(X1),1);
ex_([]) = 1;
ex_ = ex_ | (X1 <= minexclude | X1 >= maxexclude);
ok_ = isfinite(X1) & isfinite(Y1);
if ~all( ok_ )
    warning( 'GenerateMFile:IgnoringNansAndInfs', ...
        'Ignoring NaNs and Infs in data' );
end

xrange = X1(ex_ == 0); %can be differnt from exclusion rule as it's used
   to find best peaks, so should just contain the range of possible peaks
yrange = Y1(ex_ == 0);

if fxnsperpeak == 4

    %%% Changed order and nmae of parameters

    %%%---------- Added (to find approximate peak positions)
    gaussnstart = startpt(fittype('gauss4'));
    st_ = gaussnstart(xrange,yrange,4);

    start_params = [peak1_upperparams peak2_upperparams peak3_upperparans
        peak4_upperparams];
```

```
start_params(isinf(start_params)) = 0;
start_params = (start_params + [peak1_lowerparams peak2_lowerparams
    peak3_lowerparams peak4_lowerparams])/2;

st_ = diag([st_, ones(3*fxnsperpeak,1)] * [not(start_params);
    start_params]); %change automatic start points to new ones

if strcmp(typeoffit,'pv')
    ft_ = fittype('height*((1-shape)*exp(-0.69315*((x-centre)/hwhm)
        ^2)+shape/(1+((x-centre)/hwhm)^2))+height1*((1-shape1)*exp
        (-0.69315*((x-centre1)/hwhm1)^2)+shape1/(1+((x-centre1)/hwhm1)
        ^2))+ height2*((1-shape2)*exp(-0.69315*((x-centre2)/hwhm2)^2)+
        shape2/(1+((x-centre2)/hwhm2)^2)) + height3*((1-shape3)*exp
        (-0.69315*((x-centre3)/hwhm3)^2)+shape3/(1+((x-centre3)/hwhm3)
        ^2))',...
         'dependent',{'y'},'independent',{'x'},...
         'coefficients',{'height', 'centre', 'hwhm', 'height1', '
            centre1', 'hwhm1', 'height2', 'centre2', 'hwhm2','
            height3', 'centre3', 'hwhm3','shape', 'shape1', 'shape2','
            shape3'});
    st_ = [st_; [0.5; 0.5; 0.5; 0.5]]; % append shape on to other
        parameters  % append shape on to other parameters
    % Fit this model using new data
    if sum(~ex_(ok_))<2  %% too many points excluded
        error('Not enough data left to fit ''%s'' after applying
            exclusion rule ''%s''.','3 PseudoVoigts(exclusion)','erule
            ')
    else
        %Also added Lower and upper  bounds in the fit function below
             and the
        %MaxFunEvals option. gof option is returned as goodness of
            fit
        [cf_,gof,output] = fit(X1(ok_),Y1(ok_),ft_,'Startpoint',st_,'
            Exclude',ex_(ok_),'Lower',[peak1_lowerparams
```

```
            peak2_lowerparams peak3_lowerparams peak4_lowerparams 0 0
            0 0],'Upper',[peak1_upperparams peak2_upperparams
            peak3_upperparams peak4_upperparams 1 1 1 1],'MaxFunEvals'
            ,10000);
    end

    coeffs = coeffvalues(cf_);
    pv = @(x) coeffs(1)*((1-coeffs(13))*exp(-0.69315*((x-coeffs(2))/
        coeffs(3))^2)+coeffs(13)/(1+((x-coeffs(2))/coeffs(3))^2));
    pv1 = @(x) coeffs(4)*((1-coeffs(14))*exp(-0.69315*((x-coeffs(5))/
        coeffs(6))^2)+coeffs(14)/(1+((x-coeffs(5))/coeffs(6))^2));
    pv2 = @(x) coeffs(7)*((1-coeffs(15))*exp(-0.69315*((x-coeffs(8))/
        coeffs(9))^2)+coeffs(15)/(1+((x-coeffs(8))/coeffs(9))^2));
    pv3 = @(x) coeffs(10)*((1-coeffs(16))*exp(-0.69315*((x-coeffs(11)
        )/coeffs(12))^2)+coeffs(16)/(1+((x-coeffs(11))/coeffs(12))^2))
        ;

elseif strcmp(typeoffit,'gauss')
    ft_ = fittype('gauss4');
    if sum(~ex_(ok_))<2  %% too many points excluded
        error('Not enough data left to fit ''%s'' after applying
            exclusion rule ''%s''.','3 PseudoVoigts(exclusion)','erule
            ')
    else
        %Also added Lower and upper  bounds in the fit function below
            and the
        %MaxFunEvals option. gof option is returned as goodness of
            fit
        [cf_,gof,output] = fit(X1(ok_),Y1(ok_),ft_,'Startpoint',st_,'
            Exclude',ex_(ok_),'Lower',[peak1_lowerparams
            peak2_lowerparams peak3_lowerparams peak4_lowerparams],'
            Upper',[peak1_upperparams peak2_upperparams
            peak3_upperparams peak4_upperparams],'MaxFunEvals',10000);
    end
```

```
        coeffs = coeffvalues(cf_);
        pv = @(x) coeffs(1)*exp(-0.69315*((x-coeffs(2))/coeffs(3))^2);
        pv1 = @(x) coeffs(4)*exp(-0.69315*((x-coeffs(5))/coeffs(6))^2);
        pv2 = @(x) coeffs(7)*exp(-0.69315*((x-coeffs(8))/coeffs(9))^2);
        pv3 = @(x) coeffs(10)*exp(-0.69315*((x-coeffs(11))/coeffs(12))^2)
            ;

    elseif strcmp(typeoffit,'lornz')
        error('No Lorentzian fitting for more than 2 peaks');

    elseif strcmp(typeoffit,'asym')
        error('Asymmetrical fitting not implemented for more than 1 peak'
            );
    end

    fxhandles = {pv,pv1,pv2,pv3};

elseif fxnsperpeak == 3

    %%% Changed order and nmae of parameters


    %%%---------- Added (to find approximate peak positions)
    gaussnstart = startpt(fittype('gauss3'));
    st_ = gaussnstart(xrange,yrange,3);

    start_params = [peak1_upperparams peak2_upperparams peak3_upperparams
        ];
    start_params(isinf(start_params)) = 0;
    start_params = (start_params + [peak1_lowerparams peak2_lowerparams
        peak3_lowerparams])/2;
```

```
st_ = diag([st_, ones(3*fxnsperpeak,1)] * [not(start_params);
    start_params]); %change automatic start points to new ones


if strcmp(typeoffit,'pv')
    ft_ = fittype('height*((1-shape)*exp(-0.69315*((x-centre)/hwhm)
        ^2)+shape/(1+((x-centre)/hwhm)^2))+height1*((1-shape1)*exp
        (-0.69315*((x-centre1)/hwhm1)^2)+shape1/(1+((x-centre1)/hwhm1)
        ^2))+ height2*((1-shape2)*exp(-0.69315*((x-centre2)/hwhm2)^2)+
        shape2/(1+((x-centre2)/hwhm2)^2))',...
         'dependent',{'y'},'independent',{'x'},...
         'coefficients',{'height', 'centre', 'hwhm',  'height1', '
             centre1',  'hwhm1',  'height2', 'centre2', 'hwhm2','shape'
             , 'shape1', 'shape2'});
    st_ = [st_; [0.5; 0.5; 0.5]];  % append shape on to other
        parameters
    % Fit this model using new data
    if sum(~ex_(ok_))<2  %% too many points excluded
        error('Not enough data left to fit ''%s'' after applying
            exclusion rule ''%s''.','3 PseudoVoigts(exclusion)','erule
            ')
    else
        %Also added Lower and upper  bounds in the fit function below
            and the
        %MaxFunEvals option. gof option is returned as goodness of
            fit
        [cf_,gof,output] = fit(X1(ok_),Y1(ok_),ft_,'Startpoint',st_,'
            Exclude',ex_(ok_),'Lower',[peak1_lowerparams
            peak2_lowerparams peak3_lowerparams 0 0 0],'Upper',[
            peak1_upperparams peak2_upperparams peak3_upperparams 1 1
            1],'MaxFunEvals',10000);
    end

    coeffs = coeffvalues(cf_);
```

```
    pv = @(x) coeffs(1)*((1-coeffs(10))*exp(-0.69315*((x-coeffs(2))/
        coeffs(3))^2)+coeffs(10)/(1+((x-coeffs(2))/coeffs(3))^2));
    pv1 = @(x) coeffs(4)*((1-coeffs(11))*exp(-0.69315*((x-coeffs(5))/
        coeffs(6))^2)+coeffs(11)/(1+((x-coeffs(5))/coeffs(6))^2));
    pv2 = @(x) coeffs(7)*((1-coeffs(12))*exp(-0.69315*((x-coeffs(8))/
        coeffs(9))^2)+coeffs(12)/(1+((x-coeffs(8))/coeffs(9))^2));

elseif strcmp(typeoffit,'gauss')
    ft_ = fittype('gauss3');
    if sum(~ex_(ok_))<2 %% too many points excluded
        error('Not enough data left to fit ''%s'' after applying
            exclusion rule ''%s''.','3 PseudoVoigts(exclusion)','erule
            ')
    else
        %Also added Lower and upper  bounds in the fit function below
            and the
        %MaxFunEvals option. gof option is returned as goodness of
            fit
        [cf_,gof,output] = fit(X1(ok_),Y1(ok_),ft_,'Startpoint',st_,'
            Exclude',ex_(ok_),'Lower',[peak1_lowerparams
            peak2_lowerparams],'Upper',[peak1_upperparams
            peak2_upperparams],'MaxFunEvals',10000);
    end

    coeffs = coeffvalues(cf_);
    pv = @(x) coeffs(1)*exp(-0.69315*((x-coeffs(2))/coeffs(3))^2);
    pv1 = @(x) coeffs(4)*exp(-0.69315*((x-coeffs(5))/coeffs(6))^2);
    pv2 = @(x) coeffs(7)*exp(-0.69315*((x-coeffs(8))/coeffs(9))^2);

elseif strcmp(typeoffit,'lornz')
    error('No Lorentzian fitting for more than 2 peaks');

elseif strcmp(typeoffit,'asym')
```

```
        error('Asymmetrical fitting not implemented for more than 1 peak'
            );
    end



    fxhandles = {pv,pv1,pv2};

elseif fxnsperpeak == 2
    %%% Changed order and nmae of parameters


    %%%---------- Added (to find approximate peak positions)
    gaussnstart = startpt(fittype('gauss2'));
    st_ = gaussnstart(xrange,yrange,2);

    start_params = [peak1_upperparams peak2_upperparams];
    start_params(isinf(start_params)) = 0;
    start_params = (start_params + [peak1_lowerparams peak2_lowerparams])
        /2;

    st_ = diag([st_, ones(3*fxnsperpeak,1)] * [not(start_params);
        start_params]); %change automatic start points to new ones

    if strcmp(typeoffit,'pv')
        ft_ = fittype('height*((1-shape)*exp(-0.69315*((x-centre)/hwhm)
            ^2)+shape/(1+((x-centre)/hwhm)^2))+height1*((1-shape1)*exp
            (-0.69315*((x-centre1)/hwhm1)^2)+shape1/(1+((x-centre1)/hwhm1)
            ^2))',...
            'dependent',{'y'},'independent',{'x'},...
            'coefficients',{'height', 'centre', 'hwhm',  'height1', '
                centre1',  'hwhm1','shape', 'shape1',});
        st_ = [st_; [0.5; 0.5]];  % append shape on to other parameters
        % Fit this model using new data
```

```
    if sum(~ex_(ok_))<2  %% too many points excluded
        error('Not enough data left to fit ''%s'' after applying
            exclusion rule ''%s''.','3 PseudoVoigts(exclusion)','erule
            ')
    else
        %Also added Lower and upper  bounds in the fit function below
             and the
        %MaxFunEvals option. gof option is returned as goodness of
            fit
        [cf_,gof,output] = fit(X1(ok_),Y1(ok_),ft_,'Startpoint',st_,'
            Exclude',ex_(ok_),'Lower',[peak1_lowerparams
            peak2_lowerparams 0 0],'Upper',[peak1_upperparams
            peak2_upperparams 1 1],'MaxFunEvals',10000);
    end

    coeffs = coeffvalues(cf_);
    pv = @(x) coeffs(1)*((1-coeffs(7))*exp(-0.69315*((x-coeffs(2))/
        coeffs(3))^2)+coeffs(7)/(1+((x-coeffs(2))/coeffs(3))^2));
    pv1 = @(x) coeffs(4)*((1-coeffs(8))*exp(-0.69315*((x-coeffs(5))/
        coeffs(6))^2)+coeffs(8)/(1+((x-coeffs(5))/coeffs(6))^2));

elseif strcmp(typeoffit,'gauss')
    ft_ = fittype('gauss2');
    if sum(~ex_(ok_))<2  %% too many points excluded
        error('Not enough data left to fit ''%s'' after applying
            exclusion rule ''%s''.','3 PseudoVoigts(exclusion)','erule
            ')
    else
        %Also added Lower and upper  bounds in the fit function below
             and the
        %MaxFunEvals option. gof option is returned as goodness of
            fit
        [cf_,gof,output] = fit(X1(ok_),Y1(ok_),ft_,'Startpoint',st_,'
            Exclude',ex_(ok_),'Lower',[peak1_lowerparams
```

```
            peak2_lowerparams],'Upper',[peak1_upperparams
            peak2_upperparams],'MaxFunEvals',10000);
    end

    coeffs = coeffvalues(cf_);
    pv = @(x) coeffs(1)*exp(-0.69315*((x-coeffs(2))/coeffs(3))^2);
    pv1 = @(x) coeffs(4)*exp(-0.69315*((x-coeffs(5))/coeffs(6))^2);


elseif strcmp(typeoffit,'lornz')
    ft_ = fittype('height/(1+((x-centre)/hwhm)^2)+height1/(1+((x-
        centre1)/hwhm1)^2)',...
        'dependent',{'y'},'independent',{'x'},...
        'coefficients',{'height', 'centre', 'hwhm',  'height1', '
            centre1',  'hwhm1'});
    if sum(~ex_(ok_))<2  %% too many points excluded
        error('Not enough data left to fit ''%s'' after applying
            exclusion rule ''%s''.','3 PseudoVoigts(exclusion)','erule
            ')
    else
        %Also added Lower and upper  bounds in the fit function below
             and the
        %MaxFunEvals option. gof option is returned as goodness of
            fit
        [cf_,gof,output] = fit(X1(ok_),Y1(ok_),ft_,'Startpoint',st_,'
            Exclude',ex_(ok_),'Lower',[peak1_lowerparams
            peak2_lowerparams],'Upper',[peak1_upperparams
            peak2_upperparams],'MaxFunEvals',10000);
    end

    coeffs = coeffvalues(cf_);
    pv = @(x) coeffs(1)/((1+((x-coeffs(2))/coeffs(3))^2));
    pv1 = @(x) coeffs(4)/((1+((x-coeffs(5))/coeffs(6))^2));
```

```
    elseif strcmp(typeoffit,'asym')
        error('Asymmetrical fitting not implemented more than 1 peak');
    end

    fxhandles = {pv,pv1};

elseif fxnsperpeak == 1

    %%% Changed order and nmae of parameters

    %%%---------- Added (to find approximate peak positions)
    gaussnstart = startpt(fittype('gauss1'));
    st_ = gaussnstart(xrange,yrange,1);

    start_params = [peak1_upperparams ];
    start_params(isinf(start_params)) = 0;
    start_params = (start_params + [peak1_lowerparams ])/2;

    st_ = diag([st_, ones(3*fxnsperpeak,1)] * [not(start_params);
        start_params]); %change automatic start points to new ones


    %%%----------


    if strcmp(typeoffit,'pv')
        ft_ = fittype('height*((1-shape)*exp(-0.69315*((x-centre)/hwhm)
            ^2)+shape/(1+((x-centre)/hwhm)^2))',...
            'dependent',{'y'},'independent',{'x'},...
            'coefficients',{'height', 'centre', 'hwhm','shape'});
        st_ = [st_; 0.5]; % append shape on to other parameters
        % Fit this model using new data
        if sum(~ex_(ok_))<2 %% too many points excluded
```

```
        error('Not enough data left to fit ''%s'' after applying
            exclusion rule ''%s''.','3 PseudoVoigts(exclusion)','erule
            ')
    else
        %Also added Lower and upper  bounds in the fit function below
             and the
        %MaxFunEvals option. gof option is returned as goodness of
            fit
        [cf_,gof,output] = fit(X1(ok_),Y1(ok_),ft_,'Startpoint',st_,'
            Exclude',ex_(ok_),'Lower',[peak1_lowerparams 0],'Upper',[
            peak1_upperparams 1],'MaxFunEvals',10000);
    end

    coeffs = coeffvalues(cf_);
    pv = @(x) coeffs(1)*((1-coeffs(4))*exp(-0.69315*((x-coeffs(2))/
        coeffs(3))^2)+coeffs(4)/(1+((x-coeffs(2))/coeffs(3))^2));


elseif strcmp(typeoffit,'gauss')
    ft_ = fittype('gauss1');
    if sum(~ex_(ok_))<2  %% too many points excluded
        error('Not enough data left to fit ''%s'' after applying
            exclusion rule ''%s''.','3 PseudoVoigts(exclusion)','erule
            ')
    else
        %Also added Lower and upper  bounds in the fit function below
             and the
        %MaxFunEvals option. gof option is returned as goodness of
            fit
        [cf_,gof,output] = fit(X1(ok_),Y1(ok_),ft_,'Startpoint',st_,'
            Exclude',ex_(ok_),'Lower',peak1_lowerparams,'Upper',
            peak1_upperparams,'MaxFunEvals',10000);
    end
```

```
    coeffs = coeffvalues(cf_);
    pv = @(x) coeffs(1)*exp(-0.69315*((x-coeffs(2))/coeffs(3))^2);

elseif strcmp(typeoffit,'lornz')
    ft_ = fittype('height/((1+((x-centre)/hwhm)^2))',...
        'dependent',{'y'},'independent',{'x'},...
        'coefficients',{'height', 'centre', 'hwhm',});
    if sum(~ex_(ok_))<2  %% too many points excluded
        error('Not enough data left to fit ''%s'' after applying
            exclusion rule ''%s''.','3 PseudoVoigts(exclusion)','erule
            ')
    else
        %Also added Lower and upper  bounds in the fit function below
            and the
        %MaxFunEvals option. gof option is returned as goodness of
            fit
        [cf_,gof,output] = fit(X1(ok_),Y1(ok_),ft_,'Startpoint',st_,'
            Exclude',ex_(ok_),'Lower',peak1_lowerparams,'Upper',
            peak1_upperparams,'MaxFunEvals',10000);
    end

    coeffs = coeffvalues(cf_);
    pv = @(x) coeffs(1)/((1+((x-coeffs(2))/coeffs(3))^2));

elseif strcmp(typeoffit,'asym')
    ft_ = fittype('0.5*(height*(1-sign(x-centre))/((1+((x-centre)/
        hwhm)^2))) + 0.5*(height*(1-sign(centre-x))/((1+((x-centre)/
        hwhm2)^2)))',...
        'dependent',{'y'},'independent',{'x'},...
        'coefficients',{'height', 'centre', 'hwhm','hwhm2'});

    st_ = [st_(1); st_(2); 0.5*st_(3); 0.5*st_(3);]; % adjust
        starting parameters
```

```
        if sum(~ex_(ok_))<2  %% too many points excluded
            error('Not enough data left to fit ''%s'' after applying
                exclusion rule ''%s''.','3 PseudoVoigts(exclusion)','erule
                ')
        else
            %Also added Lower and upper  bounds in the fit function below
                and the
            %MaxFunEvals option. gof option is returned as goodness of
                fit
            [cf_,gof,output] = fit(X1(ok_),Y1(ok_),ft_,'Startpoint',st_,'
                Exclude',ex_(ok_),'Lower',peak1_lowerparams,'Upper',
                peak1_upperparams,'MaxFunEvals',10000);
        end

        coeffs = coeffvalues(cf_);
        pv = @(x) 0.5*(coeffs(1)*(1-sign(x-coeffs(2)))/((1+((x-coeffs(2))
            /coeffs(3))^2))) + 0.5*(coeffs(1)*(1-sign(coeffs(2)-x))/((1+((
            x-coeffs(2))/coeffs(4))^2)));

    end

    fxhandles = {pv};


end
end
```